JOURNAL OF
PETROLOGY

*Journal of Petrology*, 2015, Vol. 56, No. 7, 1365–1406
doi: 10.1093/petrology/egv040
Original Article

OXFORD

# Post-collisional Ultrapotassic Mafic Magmatism in South Tibet: Products of Partial Melting of Pyroxenite in the Mantle Wedge Induced by Roll-back and Delamination of the Subducted Indian Continental Lithosphere Slab

**Zhengfu Guo[1]*, Marjorie Wilson[2], Maoliang Zhang[1], Zhihui Cheng[1] and Lihong Zhang[1]**

[1]Key Laboratory of Cenozoic Geology and Environment, Institute of Geology and Geophysics, Chinese Academy of Sciences, PO Box 9825, Beijing 100029, China and [2]School of Earth and Environment, University of Leeds, Leeds LS2 9JT, UK

*Corresponding author. Telephone: + 86 10 82998393. Fax: + 86 10 62010846.
E-mail: zfguo@mail.iggcas.ac.cn

Received June 2, 2014; Accepted July 6, 2015

## ABSTRACT

Post-collisional (25–8 Ma) ultrapotassic mafic magmatic rocks occur to the north of the India–Asia collision zone within the Lhasa terrane of the southern Tibetan Plateau, forming a near 1000 km long semi-continuous igneous belt. They include both extrusive and intrusive facies, although lava flows dominate. To understand their petrogenesis, the mineral chemistry of olivine phenocrysts and xenocrysts and whole-rock major and trace element and Sr–Nd–Pb isotope data are presented for the most primitive mafic magmatic rocks ($MgO > 6$ wt %) from west to east. The studied samples are characterized by high MgO (6·28–15·75 wt %), $K_2O$ (4·76–8·89 wt %), $SiO_2$ (46·44–59·74 wt %), Ba (1368–14076 ppm), Th (69–336 ppm) and Ni (106–527 ppm) contents. Chondrite-normalized rare earth element (REE) patterns show enrichment in light rare earth elements (LREE), flat heavy REE (HREE) patterns and negative Eu anomalies. These REE patterns have a very distinctive inverted 'spoon shape', which appears to be a common characteristic of collision-related ultrapotassic magmas. Primitive mantle-normalized incompatible trace element patterns exhibit strong enrichments in large ion lithophile elements (LILE) relative to high field strength elements (HFSE) and strong negative Ta–Nb–Ti anomalies, which are typical of subduction-related magmas. The ultrapotassic magmatic rocks studied have extremely radiogenic initial Sr isotopic compositions (0·712379–0·737616) and low $(^{143}Nd/^{144}Nd)_i$ (0·511662–0·511984). Combined with their Pb isotope compositions $[(^{206}Pb/^{204}Pb)_i = 18{\cdot}30–18{\cdot}92$; $(^{207}Pb/^{204}Pb)_i = 15{\cdot}65–15{\cdot}87$; $(^{208}Pb/^{204}Pb)_i = 39{\cdot}02–39{\cdot}76]$ these data are consistent with the involvement of a subducted continental crustal component in their petrogenesis. The Sr–Nd–Pb isotope compositions exhibit linear trends between depleted mid-ocean ridge basalt (MORB)-source mantle (DMM) and Indian continental crust. The extreme enrichment of the upper mantle below south Tibet is considered to result from the addition of components derived from subducted Indian continental crust to the overlying mantle wedge during northward underthrusting of Indian continental lithosphere beneath the Lhasa terrane since India–Asia collision at ~55 Ma. The post-collisional K-rich mafic magmas in south Tibet were generated by partial melting of pyroxenite in a mantle source region that was created by reaction of hydrous fluids and siliceous melts from subducted granulite–eclogite-facies Indian continental crustal rocks with the surrounding peridotitic mantle. A continuous process from slab roll-back, through break-off, to detachment of the slab may have induced partial melting of the pyroxenites. Cessation of the post-collisional ultrapotassic magmatism at ~8 Ma may be linked to the onset of flat slab subduction beneath southern Tibet and the elimination of the wedge of Tibetan subcontinental lithospheric mantle and underlying asthenosphere; geophysical data indicate that at the present day eclogite-facies Indian continental crust directly underthrusts the crust of the Lhasa terrane with no intervening mantle wedge. The proportion of the Indian continental crustal component in the mantle source of the ultrapotassic mafic magmas decreases eastward, as do the ages and volumes of the magmatic rocks. There are no outcrops of post-collisional K-rich mafic magmatic rocks (MgO > 6 wt %) to the east of 87°E in the Lhasa terrane, which may indicate a change in subduction geometry at this longitude.

**Key words**: post-collisional ultrapotassic magmatism; Indian continental subduction; pyroxenite; slab roll-back; Lhasa terrane; south Tibet

## INTRODUCTION

Post-collisional potassic and ultrapotassic magmatism is widely distributed within the Alpine–Himalayan orogenic belt from Eastern Europe to the Tibetan Plateau. Understanding the petrogenesis of the most primitive K-rich magmatic rocks can provide important constraints on the evolution of the upper mantle in such continent–continent collision zones. However, their petrogenesis remains controversial, despite numerous studies (e.g. Pearce & Mei, 1988; Arnaud *et al.*, 1992; Turner *et al.*, 1996; Williams *et al.*, 2001; Ding *et al.*, 2003; Nomade *et al.*, 2004; Mo *et al.*, 2006; Gao *et al.*, 2007; Zhao *et al.*, 2009*a*; Chen *et al.*, 2010, 2011, 2012; Guo *et al.*, 2013, 2014; Wang *et al.*, 2014*a*; Liu *et al.*, 2014*a*, 2014*b*, 2014*c*).

Within the Lhasa terrane of south Tibet post-collisional, K-rich magmatic rocks are distributed in a linear belt to the north of the Indus–Tsangpo Suture (ITS) (Fig. 1). Three hypotheses have been proposed to explain this magmatism: (1) it is the product of convective removal of previously thickened lithospheric mantle (e.g. Turner *et al.*, 1993, 1996; Williams *et al.*, 2001, 2004; Chung *et al.*, 2005; Zhao *et al.*, 2009*a*); (2) it is associated with northward subduction of Indian continental lithosphere (e.g. Pearce & Mei, 1988; Arnaud *et al.*, 1992; Tapponnier, 2001; Ding *et al.*, 2003; Guo *et al.*, 2013); (3) it is the consequence of the break-off of the subducted Indian continental lithosphere slab (e.g. Miller *et al.*, 1999; DeCelles, 2002; Mahéo *et al.*, 2002; Replumaz *et al.*, 2010, 2013, 2014) or slab roll-back (e.g. Guo *et al.*, 2013). Because these previous studies mainly focused on single volcanic fields it has been difficult to develop a holistic petrogenetic model that has a realistic geodynamic context.

Ultrapotassic mafic magmatism within the Lhasa terrane occurs to the west of 87°E (Fig. 1), whereas more evolved potassic magmatism is distributed throughout the terrane. In contrast, contemporaneous, post-collisional, ore-bearing, adakite-like intrusive rocks, including the largest porphyry Cu–Mo deposit in China (Qulong) (e.g. Hou *et al.*, 2004, 2013; Yang *et al.*, 2009), are mainly distributed in the eastern part of the Lhasa terrane (Fig. 1), although rare Miocene adakite-like intrusive rocks do occur further to the west (Guo *et al.*, 2007, 2013; Zhao *et al.*, 2009*a*). It is significant that all of the post-collisional potassic and ultrapotassic magmatic rocks and adakite-like intrusive rocks are restricted in their distribution to the north of the ITS (Fig. 1), whereas contemporaneous Miocene leucogranites (Guo & Wilson, 2012) occur to the south of the ITS in the Himalayas.

None of the hypotheses mentioned above can fully explain the distribution patterns of the post-collisional potassic and ultrapotassic magmatic rocks, adakite-like intrusive rocks and leucogranites in south Tibet and the Himalayas. Additionally, most of the previously studied samples were of evolved magmatic rocks (MgO < 6 wt %), the parental magmas of which must have undergone combined crustal contamination and fractional crystallization (Guo *et al.*, 2006, 2013), making it difficult to constrain the nature of their mantle source. The lack of detailed field sampling and of petrological, geochronological and geochemical data for the whole volcanic belt from east to west in the Lhasa terrane (Fig. 1) has precluded further advances in understanding the petrogenesis of the magmas.

In this study, we report new bulk-rock major and trace element, Sr–Nd–Pb isotope and olivine phenocryst composition data for the entire, near 1000 km long, post-collisional ultrapotassic mafic magmatic belt (Fig. 1) in the Lhasa terrane of the southern Tibetan Plateau. Samples were selected to minimize the effects of shallow-level crustal contamination and magmatic differentiation. Our samples are representative of all of the post-collisional K-rich mafic volcanic fields recognized in previous studies (e.g. Miller *et al.*, 1999; Williams *et al.*, 2001; Ding *et al.*, 2003, 2006; Chen *et al.*, 2007; Gao *et al.*, 2007; Guo *et al.*, 2013) and also from additional outcrops new to our study (Fig. 1). On the basis of our new data and previously published geochemical and geophysical data, we develop a robust petrogenetic model to better explain genesis of the post-collisional ultrapotassic mafic magmas, their mantle source characteristics and geodynamic setting.

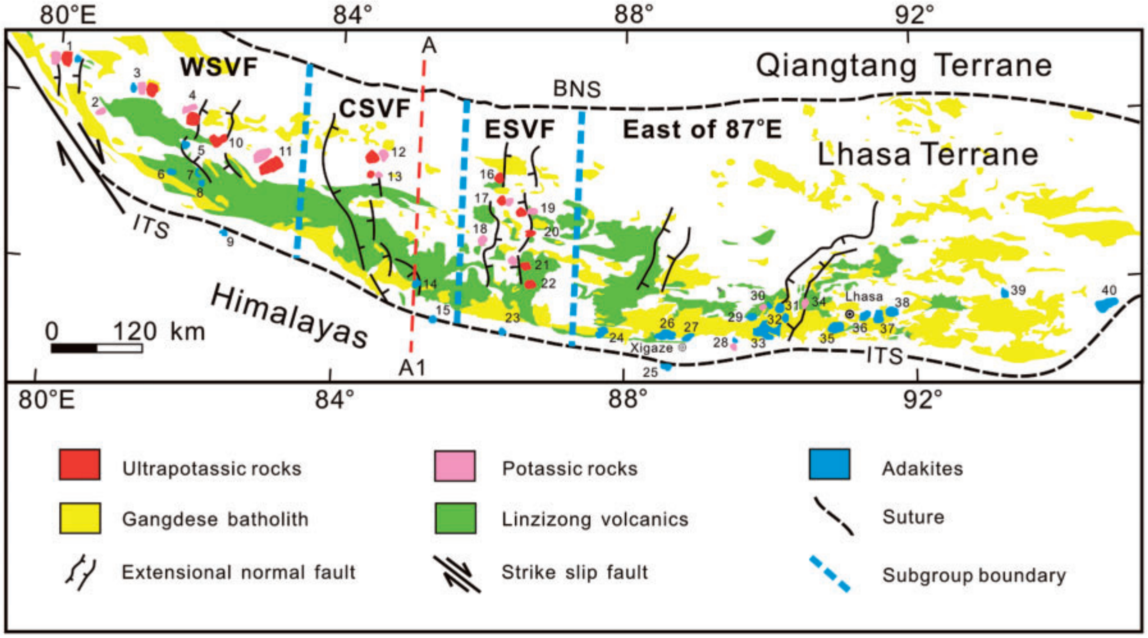

**Fig. 1.** Simplified map showing the distribution of Cenozoic magmatic rocks in southern Tibet (modified from Pan *et al.*, 2004; Ding *et al.*, 2006; Guo *et al.*, 2007, 2013; Hou *et al.*, 2013). The red dashed line labeled A–A1 represents the location of the line of the Hi-CLIMB seismic array at ~85°E from Nábělek *et al.* (2009). BNS, Bangong–Nujiang Suture; ITS, Indus–Tsangpo Suture. WSVF, western subgroup volcanic fields; CSVF, central subgroup volcanic fields; ESVF, eastern subgroup volcanic fields. Numbers indicate the volcanic fields (or intrusive bodies): 1, Shiquanhe; 2, Chajiasi; 3, Bongba; 4, Xungba; 5, Gegar; 6, Manasarowar; 7, Yare; 8, Puridazong; 9, Mayum; 10, Jarga; 11, Sailipu; 12, Zabuye; 13, Maiga; 14, Daggyai; 15, Saga; 16, Garwa; 17, Yaqian; 18, Konglongxiang; 19, Mibale; 20, Yiqian; 21, Chazi; 22, Pabbai; 23, Sangsang; 24, Zhunuo; 25, Kuday; 26, Nanmuqie; 27, Xigaze; 28, Namlin; 29, Chongjiang; 30, Majiang; 31, Nimu; 32, Tinggong; 33, Pagu; 34, Yangying; 35, Nanmu; 36, Qulong; 37, Lakang'e; 38, Jiama; 39, Tangbula; 40, Linzhi.

## GEOLOGICAL SETTING

The Tibetan Plateau is a collage of east–west-trending allochthonous microcontinent terranes (Kunlun, Songpan–Ganzi, Qiangtang and Lhasa), which were successively accreted to the southern margin of the Asian continent since Palaeozoic times (Fig. 1). The Lhasa terrane is bordered by the Bangong–Nujiang Suture (BNS) to the north and the Indus–Tsangpo Suture (ITS) to the south (Fig. 1). Collision between the Indian and Asian continents at ~55–50 Ma resulted in the formation of the ITS and the Tibetan–Himalayan orogenic belt (e.g. Patriat & Achache, 1984; Klootwijk *et al.*, 1992; Leech *et al.*, 2005; Zhu *et al.*, 2005; Royden *et al.*, 2008; Najman *et al.*, 2010; Sun *et al.*, 2012).

Extensive magmatic activity has characterized the Lhasa terrane during Cenozoic times, associated with India–Asia continent–continent collision. Three types of magmatism can be distinguished based on their temporal–spatial distribution and geochemical characteristics. The first type includes calc-alkaline volcanism (Linzizong volcanic series) and associated granitoid batholiths (Gangdese batholith) during the period 65–40 Ma (Schärer *et al.*, 1984; Coulon *et al.*, 1986; Zhou *et al.*, 2004; Mo *et al.*, 2005, 2006; Wen *et al.*, 2008; Niu *et al.*, 2013; Fig. 1), considered to be the consequence of northward subduction of Neo-Tethyan oceanic lithosphere beneath the Lhasa terrane. The second type comprises Oligocene–Miocene (26–10 Ma) adakite-like intrusive rocks, which are mainly distributed in the eastern part of the Lhasa terrane (Fig. 1) and have been proposed to be the products of melting of thickened lower crust (e.g. Chung *et al.*, 2003; Hou *et al.*, 2004; Guo *et al.*, 2007; Zheng *et al.*, 2012; Zhang *et al.*, 2014*a*). The third type consists of the ultrapotassic and potassic magmatic rocks, which are the focus of this study (Fig. 1); their ages range from 25 to 8 Ma based on $^{40}$Ar/$^{39}$Ar, K–Ar, Rb–Sr and single-crystal zircon U–Pb dating (e.g. Coulon *et al.*, 1986; Yin *et al.*, 1994; Miller *et al.*, 1999; Williams *et al.*, 2001, 2004; Ding *et al.*, 2003; Nomade *et al.*, 2004; Mo *et al.*, 2006; Zhao *et al.*, 2006, 2009*a*, *b*; Sun *et al.*, 2008; Chen *et al.*, 2010; Zhou *et al.*, 2010; Liu *et al.*, 2011*b*, 2014*b*, *c*; Guo *et al.*, 2013). They crop out as small-volume lava flows, plugs and dyke swarms within a series of north–south-trending rifts bounded by normal faults (Guo *et al.*, 2013; Fig. 1). Recent geophysical studies (e.g. Li *et al.*, 2008; Nábělek *et al.*, 2009; Zhao *et al.*, 2011; Zhang *et al.*, 2014*b*) suggest that at present the Tibetan Plateau crust beneath these volcanic fields is underlain by a flat-lying layer of inferred subducted Indian continental crust, ~15–20 km thick, with no intervening mantle wedge. This lower layer of the crust could be made of amphibolite-, granulite- or eclogite-facies metamorphic rocks (Worthington *et al.*, 2013; Zhang *et al.*, 2014*b*).

### Ultrapotassic volcanic fields

Thirteen ultrapotassic mafic volcanic fields have been identified, which form the basis of this study, extending from the Shiquanhe volcanic field in the west, through the Bongba, Xungba, Jarga, Sailipu, Zabuye, Maiga, Garwa, Yaqian, Mibale, Yiqian and Chazi volcanic fields to the Pabbai volcanic field in the east (Fig. 1). Exposures range from less than ~1 km$^2$ to ~600 km$^2$. Lava flow thicknesses vary from ~30 m in the Yiqian volcanic field to about 300 m in the Zabuye volcanic field. The volume of magmatism appears to decrease from west to east; the Maiga and Yiqian volcanic fields in the east have the smallest exposed areas of less than 1 km$^2$, whereas the Xungba, Sailipu and Zabuye volcanic fields in the west have the largest exposed areas of 400–600 km$^2$. For ease of reference we have subdivided the volcanic fields into three subgroups based upon longitude: (1) a western subgroup (WSVF; including the Shiquanhe, Bongba, Xungba, Jarga and Sailipu volcanic fields), (2) a central subgroup (CSVF; including the Zabuye and Maiga volcanic fields) and (3) an eastern subgroup (ESVF; including the Garwa, Yaqian, Mibale, Yiqian, Chazi and Pabbai volcanic fields) (Fig. 1).

### Age of the volcanism

To study the timing of the ultrapotassic mafic magmatism we have compiled all the available geochronological data from the published literature (Table 1), including Miller *et al.* (1999), Williams *et al.* (2001, 2004), Nomade *et al.* (2004) and Guo *et al.* (2013). A range of geochronometers (e.g. $^{40}$Ar/$^{39}$Ar, K–Ar, U–Pb, Rb–Sr) have been used and we have checked the data quality and compared the ages from the various methods to identify any age trends. Our analysis of the data (Fig. 2 and Table 1) indicates that the age of the magmatism ranges from 25 to 8 Ma and shows a decreasing trend from north to south (Fig. 2a) and from west to east (Fig. 2b). This is a very interesting and important observation, which may be consistent with Indian slab roll-back during the period 25–8 Ma from north to south combined with slab break-off that propagated eastwards from 25 to 10 Ma, as proposed by Replumaz *et al.* (2010, 2013, 2014) and Guo *et al.* (2013).

The magmatism in the eastern subgroup (ESVF) ranges widely in age from 25 to 8 Ma (Guo *et al.*, 2013). Here volcanism youngs from north to south within a single north–south-trending rift and has been interpreted by Guo *et al.* (2013) to reflect magma generation in response to progressive roll-back of the subducted Indian lithosphere.

## PETROGRAPHY

The post-collisional ultrapotassic mafic magmatic rocks (MgO > 6 wt %) studied have porphyritic textures with phenocrysts of clinopyroxene, phlogopite, olivine and rare sanidine; the groundmass includes phlogopite, clinopyroxene, olivine, sanidine, apatite, Fe–Ti oxides, leucite, zircon and glass. The typical size of the phenocrysts is 1–5 mm. The main petrographic characteristics are summarized in Table 2.

Mantle-derived olivine xenocrysts have been recognized in the ultrapotassic magmatic rocks of the Xungba and Sailipu volcanic fields (Fig. 1). Some samples from the Sailipu volcanic field also contain mantle xenoliths, which comprise olivine, orthopyroxene, clinopyroxene and spinel (Zhao *et al.*, 2009*a*; Liu *et al.*, 2011*a*, 2014*a*). The olivine xenocrysts are characterized by disequilibrium textures and reaction rims (Fig. 3a and f). Most of the olivine phenocrysts in the most primitive magmatic rocks of the Sailipu and Maiga volcanic fields (e.g. MgO ~15 wt % in sample MG1303; Table 3) have corroded rims (Fig. 3b). Some of the olivine xenocrysts in the ultrapotassic rocks of the Xungba and Sailipu volcanic fields have reaction rims of pyroxene (Fig. 3c). Phlogopite and clinopyroxene (Fig. 3d and e) occur as euhedral phenocrysts and microphenocrysts.

## ANALYTICAL METHODS

All of the analysed samples show no evidence of significant hydrothermal alteration or weathering. Samples 4–5 kg in weight were cut into thin slices, which were cleaned three times using deionized water, dried and then crushed between corundum plates, and finally ground into whole-rock powders in an agate mortar in preparation for whole-rock major element, trace element and Sr–Nd–Pb isotope analysis.

### Whole-rock major and trace element analyses

Whole-rock major element contents were determined on fused glass discs by X-ray fluorescence (XRF) using an XRF-1500 sequential spectrometer at the Institute of Geology and Geophysics, Chinese Academy of Sciences (IGGCAS). Sample powders (0·6 g) were fused with $Li_2B_4O_7$ (6 g) in a TR-1000S automatic bead fusion furnace at 1100°C for 10 min. Loss on ignition (LOI) was determined by ignition at 1100°C for 10 h of 2 g powders. The analytical precision was better than 2% relative, including the errors in $SiO_2$ and $Al_2O_3$ contents inherited from sample crushing using corundum plates and grinding in an agate mortar. The detailed analytical method follows that given by Guo *et al.* (2006, 2013). Whole-rock major element compositions are reported in Table 3.

Whole-rock trace element contents were determined by inductively coupled plasma mass spectrometry (ICP-MS) using a FINNIGAN MAT II element system at IGGCAS. Whole-rock powders (40 mg) were dissolved in distilled 1 ml 20N HF and 0·5 ml 7·5 N $HNO_3$ in 7 ml Savillex Teflon screw-cap capsules and then were ultrasonically stirred for 15 min. Then, the solutions were evaporated at 150°C to dryness and the residue was digested with 1·5 ml 20N HF and 0·5 ml $HNO_3$ [$HNO_3$:$H_2O$ = 1:1 (volume ratio)] in Teflon screw-cap capsules. The solutions were heated at 130°C for 2 h, then their temperature was gradually increased up to 170°C over 24 h. The solutions were then maintained at

**Table 1**: Ages of the post-collisional K-rich magmatism in south Tibet

| Field no. | Sample no. | Field name | Dating method | Materials dated | Age (Ma) | Data sources |
|---|---|---|---|---|---|---|
| 1 | 97–7–16–2pk | Shiquanhe | $^{40}$Ar/$^{39}$Ar | Biotite | 22·6 ± 0·1 (a) | [1] |
| 1 | JPT24C | Shiquanhe | $^{40}$Ar/$^{39}$Ar | Phl | 24·0 ± 1·0 (b) | [2] |
| 1 | JPT24B | Shiquanhe | $^{40}$Ar/$^{39}$Ar | Phl | 22·3 ± 4·7 (b) | [2] |
| 1 | JPT23 | Shiquanhe | $^{40}$Ar/$^{39}$Ar | Phl | 21·2 ± 0·6 (b) | [2] |
| 3 | TE148/93 | Bongba | $^{40}$Ar/$^{39}$Ar | WR | 23·3 ± 0·2 (c) | [3] |
| 3 | TE150/93 | Bongba | $^{40}$Ar/$^{39}$Ar | WR | 25·4 ± 0·2 (c) | [3] |
| 4 | TE011/93 | Xungba | $^{40}$Ar/$^{39}$Ar | Phl | 23·0 ± 0·3 (d) | [3] |
| 4 | TE011/93 | Xungba | Rb–Sr | Phl–WR | 22·4 ± 0·3 (b) | [3] |
| 4 | TE011/93 | Xungba | $^{40}$Ar/$^{39}$Ar | Groundmass | 21·0 ± 0·4 (c) | [3] |
| 4 | TE138/93 | Xungba | $^{40}$Ar/$^{39}$Ar | Phl | 18·1 ± 0·3 (d) | [3] |
| 4 | TE025/93 | Xungba | $^{40}$Ar/$^{39}$Ar | WR | 22·8 ± 0·2 (d) | [3] |
| 4 | 10XB01 | Xungba | U–Pb | Zircon | 24·1 ± 0·3 (e) | [4] |
| 4 | 10XB06 | Xungba | U–Pb | Zircon | 23·3 ± 0·4 (e) | [4] |
| 4 | 10YR06 | Xungba | U–Pb | Zircon | 23·9 ± 0·6 (e) | [4] |
| 4 | 08YR05 | Xungba | U–Pb | Zircon | 23·2 ± 0·4 (e) | [5] |
| 4 | 10YR06 | Xungba | U–Pb | Zircon | 23·8 ± 1·0 (e) | [5] |
| 4 | 10XB10 | Xungba | U–Pb | Zircon | 22·7 ± 1·3 (e) | [5] |
| 10 | TE117/93 | Jarga | $^{40}$Ar/$^{39}$Ar | Phl | 18·5 ± 0·4 (d) | [3] |
| 10 | TE118/93 | Jarga | $^{40}$Ar/$^{39}$Ar | Phl | 18·3 ± 0·4 (d) | [3] |
| 11 | Not mentioned | Sailipu | $^{40}$Ar/$^{39}$Ar | WR | 15·47 ± 0·30 (c) | [6, 7] |
| 11 | Not mentioned | Sailipu | K–Ar | WR | 15·24 ± 0·30 (f) | [6] |
| 11 | Not mentioned | Sailipu | K–Ar | WR | 16·07 ± 0·32 (f) | [6] |
| 11 | Not mentioned | Sailipu | K–Ar | WR | 17·8 ± 0·3 (f) | [6, 7] |
| 11 | SL0619 | Sailipu | U–Pb | Zircon | 17·01 ± 3·99 (e) | [8] |
| 11 | SL0625 | Sailipu | U–Pb | Zircon | 16·28 ± 0·95 (e) | [8] |
| 11 | SL0628 | Sailipu | U–Pb | Zircon | 17·67 ± 0·33 (e) | [8] |
| 11 | 05SLP-8–1 | Sailipu | $^{40}$Ar/$^{39}$Ar | Phl | 17·58 ± 0·19 (d) | [9] |
| 11 | 08SLP4–2 | Sailipu | $^{40}$Ar/$^{39}$Ar | Phl | 18·48 ± 0·34 (d) | [10] |
| 11 | SLP1101 | Sailipu | U–Pb | Zircon | 18·1 ± 0·6 (e) | [5] |
| 12 | Not mentioned | Zabuye | K–Ar | WR | 15·8 ± 0·3 (f) | [11] |
| 12 | Not mentioned | Zabuye | K–Ar | WR | 15·9 ± 0·3 (f) | [11] |
| 12 | ZB1 | Zabuye | $^{40}$Ar/$^{39}$Ar | Sanidine | 16·16 ± 0·12 (d) | [12] |
| 12 | ZB4 | Zabuye | $^{40}$Ar/$^{39}$Ar | Sanidine | 16·12 ± 0·12 (d) | [12] |
| 12 | ZB10 | Zabuye | $^{40}$Ar/$^{39}$Ar | Sanidine | 16·02 ± 0·17 (d) | [12] |
| 12 | ZB10 | Zabuye | $^{40}$Ar/$^{39}$Ar | Biotite | 16·1 ± 0·2 (d) | [12] |
| 12 | ZB12 | Zabuye | $^{40}$Ar/$^{39}$Ar | Sanidine | 16·01 ± 0·12 (d) | [12] |
| 12 | ZB12 | Zabuye | $^{40}$Ar/$^{39}$Ar | Biotite | 16·11 ± 0·16 (d) | [12] |
| 12 | CQ1–04–02 | Zabuye | $^{40}$Ar/$^{39}$Ar | WR | 15·56 ± 0·07 (d) | [13] |
| 12 | ZB1 | Zabuye | $^{40}$Ar/$^{39}$Ar | Sanidine | 16·23 ± 0·05 (d) | [13] |
| 12 | ZB4 | Zabuye | $^{40}$Ar/$^{39}$Ar | Sanidine | 16·17 ± 0·04 (d) | [13] |
| 12 | ZB10 | Zabuye | $^{40}$Ar/$^{39}$Ar | Sanidine | 16·02 ± 0·03 (d) | [13] |
| 12 | ZB10 | Zabuye | $^{40}$Ar/$^{39}$Ar | Biotite | 16·19 ± 0·14 (d) | [13] |
| 12 | ZB12 | Zabuye | $^{40}$Ar/$^{39}$Ar | Sanidine | 16·07 ± 0·03 (d) | [13] |
| 12 | ZB12 | Zabuye | $^{40}$Ar/$^{39}$Ar | Biotite | 16·21 ± 0·13 (d) | [13] |
| 12 | ZB1102 | Zabuye | U–Pb | Zircon | 15·7 ± 0·4 (e) | [5] |
| 12 | ZB1106 | Zabuye | U–Pb | Zircon | 16·0 ± 0·6 (e) | [5] |
| 13 | 2003T405 | Maiga | $^{40}$Ar/$^{39}$Ar | Biotite | 17·4 ± 0·1 (d) | [14] |
| 13 | CQ01 | Maiga | $^{40}$Ar/$^{39}$Ar | WR | 16·10 ± 0·12 (c) | [15, 16] |
| 13 | CQ02 | Maiga | $^{40}$Ar/$^{39}$Ar | WR | 16·59 ± 0·13 (c) | [15, 16] |
| 16 | 99T60 | Garwa | $^{40}$Ar/$^{39}$Ar | Sanidine | 22·9 ± 0·7 (d) | [17] |
| 16 | 99T62 | Garwa | $^{40}$Ar/$^{39}$Ar | Sanidine | 17·8 ± 0·3 (c) | [17] |
| 17 | DR01–01 | Yaqian | $^{40}$Ar/$^{39}$Ar | Biotite | 13·4 ± 0·2 (d) | [18] |
| 17 | DR01–02 | Yaqian | $^{40}$Ar/$^{39}$Ar | Sanidine | 13·7 ± 0·2 (d) | [18] |
| 17 | DR03 | Yaqian | $^{40}$Ar/$^{39}$Ar | Sanidine | 14·2 ± 0·3 (d) | [18] |
| 17 | DR04 | Yaqian | $^{40}$Ar/$^{39}$Ar | Sanidine | 13·5 ± 0·2 (d) | [18] |
| 19 | 8030–5 | Mibale | K–Ar | WR | 19·04 ± 0·97 (f) | [19, 20] |
| 19 | 8030–5 | Mibale | K–Ar | WR | 12·60 ± 0·97 (f) | [19, 21] |
| 19 | 8030–18 | Mibale | K–Ar | WR | 14·22 ± 0·68 (f) | [19] |
| 20 | 2003T536 | Yiqian | $^{40}$Ar/$^{39}$Ar | Biotite | 13·5 ± 0·1 (d) | [14] |
| 20 | DR1104 | Yiqian | U–Pb | Zircon | 12·9 ± 0·5 (e) | [5] |
| 20 | DR1114 | Yiqian | U–Pb | Zircon | 11·2 ± 0·9 (e) | [5] |
| 21 | 99T132 | Chazi | $^{40}$Ar/$^{39}$Ar | Phl | 13·3 ± 0·4 (d) | [17] |
| 21 | 99T145 | Chazi | $^{40}$Ar/$^{39}$Ar | Sanidine | 8·2 ± 0·5 (d) | [17] |
| 21 | 99T154 | Chazi | $^{40}$Ar/$^{39}$Ar | Sanidine | 13·1 ± 0·3 (d) | [17] |
| 21 | XR01–03 | Chazi | $^{40}$Ar/$^{39}$Ar | Biotite | 11·2 ± 0·3 (a) | [18] |
| 21 | XR01–3 | Chazi | $^{40}$Ar/$^{39}$Ar | Biotite | 11·5 ± 0·2 (d) | [15] |
| 21 | G8 | Chazi | U–Pb | Zircon | 11·70 ± 0·15 (g) | [22] |
| 22 | JPT7 | Pabbai | $^{40}$Ar/$^{39}$Ar | Phl | 18·3 ± 2·7 (b) | [23] |
| 22 | T2A | Pabbai | $^{40}$Ar/$^{39}$Ar | Phl | 13·8 ± 3·5 (b) | [23] |
| 22 | T3B | Pabbai | $^{40}$Ar/$^{39}$Ar | Biotite | 13·8 ± 0·3 (b) | [23] |
| 22 | T5A | Pabbai | $^{40}$Ar/$^{39}$Ar | Phl | 13·3 ± 0·8 (b) | [23] |

Field number refers to number of the volcanic field in Fig. 1. Field name corresponds to that in Fig. 1. Sources of the age data for the magmatic rocks are as follows: [1] Kapp *et al.* (2003); [2] Williams *et al.* (2004); [3] Miller *et al.* (1999); [4] Liu *et al.* (2011*b*); [5] Liu *et al.* (2014*b*, c); [6] Geological Survey Bureau of Chengdu University of Technology (2006); [7] Sun *et al.* (2007); [8] Sun *et al.* (2008); [9] Wang *et al.* (2008); [10] Chen *et al.* (2012); [11] Ma *et al.* (2002); [12] Nomade *et al.* (2004); [13] Zhao *et al.* (2009*a*); [14] Ding *et al.* (2006); [15] Zhao *et al.* (2009*b*);[16] Mo *et al.* (2006); [17] Ding *et al.* (2003); [18] Zhao *et al.* (2006); [19] Xie *et al.* (2004); [20] Gao *et al.* (2007); [21] Liao *et al.* (2002); [22] Guo *et al.* (2013); [23] Williams *et al.* (2001). Age categories of the K-rich magmatic rocks, which are shown by letters in parentheses, are as follows: (a) inverse isochron age; (b) isochron age; (c) total gas age; (d) plateau age; (e) weighted mean age by LA-ICP-MS; (f) K–Ar age; (g) isochron age by SHRIMP. Phl, phlogopite; WR, whole-rock.

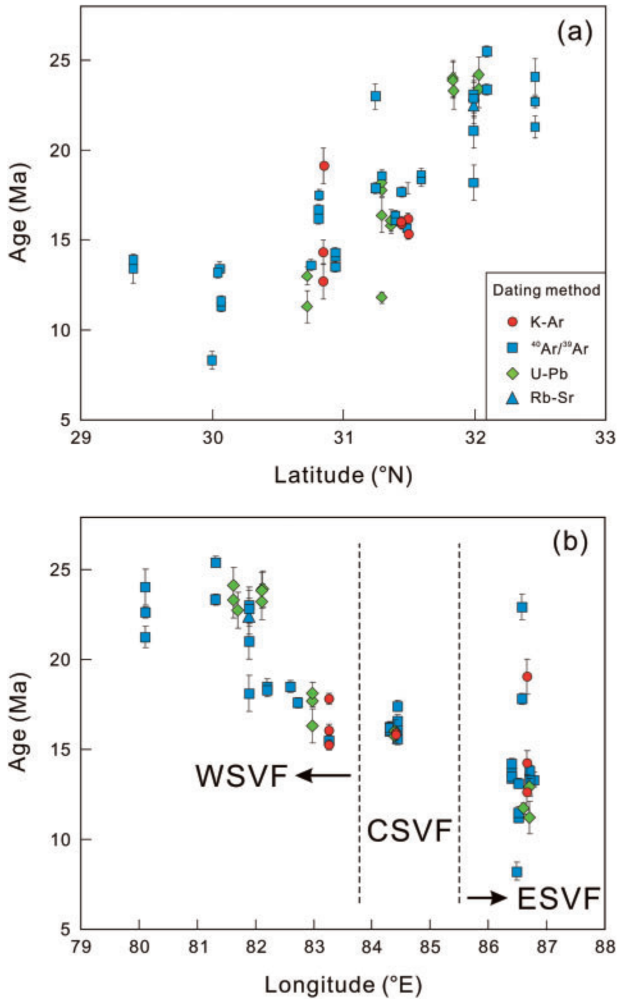

**Fig. 2.** Ages of the post-collisional ultrapotassic magmatic rocks from north to south (a) and from west to east (b) in south Tibet. WSVF, western subgroup volcanic fields; CSVF, central subgroup volcanic fields; ESVF, eastern subgroup volcanic fields. Data for the ages of the magmatic rocks are from Table 1.

170°C for 10 days, dried and redissolved in 2 ml $HNO_3$ [$HNO_3$:$H_2O$ = 1:1 (volume ratio)] in the capsules. The solutions were heated at 150°C for 5 h and then evaporated, dried and redissolved in 2 ml $HNO_3$ [$HNO_3$:$H_2O$ = 1:1 (volume ratio)] and 2 ml 1% $HNO_3$ at 150°C for 5 h in screw-cap capsules to ensure that the samples were completely dissolved. The solutions were put into plastic beakers and then 1 ml 500 ppb In was added as an internal standard. Finally, the solutions were diluted in 1% $HNO_3$ to 50 ml for analysis by ICP-MS. A blank solution was prepared; the total procedural blanks were <50 ng for all the trace elements reported in Table 3. During the analytical runs, frequent standard calibrations were performed to correct for instrumental signal drift following the procedure of Guo *et al.* (2006). Four replicates and two international standards (BHVO-1 and AGV-1) were prepared using the same procedure to monitor the analytical reproducibility. The discrepancy, based on repeated analyses of samples and international standards, is less than 4% for the trace elements reported in Table 3. Analyses of the international standards are in excellent agreement with the recommended values (Govindaraju, 1994), and deviate less than 5% from the published values (Table 3). The detailed analytical procedures follow those of Guo *et al.* (2006, 2013).

## Whole-rock Sr–Nd–Pb isotope analyses

Whole-rock Sr–Nd–Pb isotope analyses were performed on a Finnigan MAT262 mass spectrometer at IGGCAS. Whole-rock powders (60 mg) were spiked with mixed isotope tracers ($^{87}$Rb–$^{84}$Sr for Rb–Sr isotope analyses and $^{149}$Sm–$^{150}$Nd for Sm–Nd isotope analyses), then dissolved with a mixed acid (HF:$HClO_4$ = 3:1; volume ratio) in Teflon capsules for 7 days at room temperature. Rb and Sr and rare earth element (REE) fractions were separated in solution using AG50W × 8 ($H^+$) cationic ion-exchange resin columns. Sm and Nd were separated from the other rare earth element fractions in solution using AG50W × 8 ($H^+$) cationic ion-exchange columns and P507 extraction and eluviation resin. The collected Sr and Nd fractions were evaporated and dissolved in 2% $HNO_3$ to give solutions for analysis by mass spectrometry. The mass fractionation corrections for Sr and Nd isotopic ratios were based on $^{86}$Sr/$^{88}$Sr = 0·1194 and $^{146}$Nd/$^{144}$Nd = 0·7219, respectively. The international standard NBS987 yielded $^{87}$Sr/$^{86}$Sr = 0·710254 ± 16 ($n$ = 8, 2$\sigma$) (the recommended value is 0·710240) and international standard NBS607 yielded $^{87}$Sr/$^{86}$Sr = 1·20032 ± 30 ($n$ = 12, 2$\sigma$) (the recommended value is 1·20039). The international La Jolla standard gave $^{143}$Nd/$^{144}$Nd = 0·511862 ± 7 ($n$ = 12, 2$\sigma$) (the recommended value is 0·511859) and international standard BCR-1 gave $^{143}$Nd/$^{144}$Nd = 0·512626 ± 9 ($n$ = 12, 2$\sigma$) (the recommended value is 0·512638). The whole procedure blank is less than 200 pg for Rb–Sr isotopic analysis and 50 pg for Sm–Nd isotopic analysis. Analytical errors for Sr and Nd isotopic ratios are reported as 2$\sigma$ in Table 4. The initial $^{87}$Sr/$^{86}$Sr and $^{143}$Nd/$^{144}$Nd ratios were calculated using the average ages of the samples based on $^{40}$Ar/$^{39}$Ar, K–Ar and U–Pb zircon dating methods (Table 1).

For whole-rock Pb isotope analyses, 150 mg powder was weighed and dissolved in Teflon capsules using concentrated HF at 120°C for 7 days. Pb was separated from the silicate matrix and purified using AG1 × 8 anionic ion-exchange columns with dilute HBr as eluant. The whole procedure blank is less than 1 ng. During the period of analysis repeat analyses of the international standard NBS981 gave $^{204}$Pb/$^{206}$Pb = 0·059003 ± 0·000084 ($n$ = 6, 2$\sigma$) (the certified value is 0·058998), $^{207}$Pb/$^{206}$Pb = 0·91449 ± 0·00017 ($n$ = 6, 2$\sigma$) (the certified value is 0·914598) and $^{208}$Pb/$^{206}$Pb = 2·16691 ± 0·00097 ($n$ = 6, 2$\sigma$) (the certified value is 2·168099). Pb isotope fractionations were corrected using correction factors based on replicate analyses of the international standard NBS981. The Pb isotope data are reported in

**Table 2**: Phenocryst and groundmass minerals of the K-rich mafic magmatic rocks in south Tibet

| Field. no. | Sample no. | Field name | Facies | Mg-no. | Phenocrysts | Groundmass |
|---|---|---|---|---|---|---|
| 1 | GZ-S05 | Shiquanhe | lava flow | 0·72 | Cpx + Ol + Phl | Phl + Cpx + Sa + Fe–Ti + G |
| 1 | GZ-S06 | Shiquanhe | lava flow | 0·72 | Phl + Cpx + Sa | Cpx + Phl + Sa + G |
| 1 | GZ-S12 | Shiquanhe | lava flow | 0·76 | Ol + Phl + Cpx + Fe–Ti | Cpx + Phl + Sa + Fe–Ti + G |
| 1 | GZ-S15 | Shiquanhe | lava flow | 0·70 | Phl + Cpx + Fe–Ti | Phl + Cpx + Sa + G |
| 1 | GZ-S27 | Shiquanhe | lava flow | 0·72 | Ol + Cpx + Fe–Ti | Cpx + Ol + Phl + Sa + Fe–Ti |
| 1 | SQH-08 | Shiquanhe | lava flow | 0·78 | Ol + Phl + Cpx | Ol + Phl + Cpx + Sa + Fe–Ti + G |
| 1 | SQH-15 | Shiquanhe | lava flow | 0·74 | Ol + Phl + Cpx + Fe–Ti | Cpx + Sa + Phl + Ap |
| 3 | 16YS | Bongba | lava flow | 0·75 | Ol + Phl + Cpx + Sa | Phl + Cpx + Sa + Ap |
| 3 | 20YS | Bongba | lava flow | 0·74 | Phl + Ol + Cpx + Ap | Cpx + Phl + Sa + Fe–Ti + G |
| 3 | 23YS | Bongba | lava flow | 0·72 | Ol + Phl + Cpx + Ap | Cpx + Sa + Phl + Fe–Ti + Ap + G |
| 3 | 25YS | Bongba | lava flow | 0·77 | Ol + Cpx + Phl | Ol + Cpx + Phl + Sa + Ap + Pl + G |
| 3 | JS07 | Bongba | lava flow | 0·74 | Cpx + Ol + Phl | Cpx + Sa + Phl + Ap + Fe–Ti |
| 4 | 99-B06 | Xungba | lava flow | 0·80 | Ol + Cpx + Phl + Fe–Ti | Sa + Cpx + Phl + Fe–Ti |
| 4 | 99-B09 | Xungba | lava flow | 0·73 | Ol + Cpx + Phl | Phl + Ol + Sa + Cpx + G |
| 4 | 99-B23 | Xungba | lava flow | 0·74 | Ol + Cpx + Phl | Cpx + Sa + Phl + Fe–Ti + Ap |
| 4 | 99-C12 | Xungba | lava flow | 0·74 | Ol + Phl + Cpx | Cpx + Ol + Sa + Pl + Fe–Ti + Ap |
| 11 | 99-C15 | Sailipu | lava flow | 0·76 | Ol + Cpx + Phl | Ol + Phl + Cpx + G |
| 11 | 99-C28 | Sailipu | lava flow | 0·76 | Ol + Cpx + Sa | Ol + Phl + Cpx + Sa |
| 11 | XB-06 | Sailipu | lava flow | 0·76 | Ol + Cpx + Phl | Ol + Phl + Cpx + Sa |
| 11 | XB-24 | Sailipu | lava flow | 0·78 | Cpx + Ol + Phl | Ol + Phl + Cpx + Ap |
| 12 | BG015 | Zabuye | lava flow | 0·83 | Ol + Cpx + Phl + Sa | Ol + Sa + Cpx + Ap + G |
| 12 | BG026 | Zabuye | lava flow | 0·77 | Ol + Phl + Sa + Cpx | Sa + Cpx + Phl + G |
| 12 | BG037 | Zabuye | lava flow | 0·77 | Cpx + Ol + Phl + Sa | Cpx + Ol + Sa + Fe–Ti |
| 12 | BG201 | Zabuye | lava flow | 0·72 | Sa + Cpx + Phl | Sa + Cpx + Pl + Ap |
| 12 | BG203 | Zabuye | lava flow | 0·80 | Ol + Cpx + Sa + Phl | Ol + Cpx + Sa + Ap |
| 13 | MG-008 | Maiga | lava flow | 0·88 | Ol + Phl | Ol + Sa + G |
| 13 | MG-012 | Maiga | plug | 0·81 | Ol + Phl | Cpx + Sa + Ap + Fe–Ti |
| 13 | MG-015 | Maiga | plug | 0·79 | Ol + Phl | Ol + Cpx + Phl + G |
| 13 | MG-016 | Maiga | dyke | 0·76 | Ol + Cpx | Cpx + Sa + Fe–Ti |
| 16 | GZF3 | Garwa | lava flow | 0·79 | Phl + Cpx + Lc + Ol | Sa + Cpx + Ap + Fe–Ti |
| 16 | GZF9 | Garwa | lava flow | 0·74 | Ol + Phl + Cpx + Lc | Cpx + Sa + Ap + Fe–Ti |
| 17 | G-029 | Yaqian | lava flow | 0·79 | Phl + Cpx | Cpx + Sa + Fe–Ti |
| 17 | GH03 | Yaqian | lava flow | 0·79 | Cpx + Ol | Ol + Cpx + Ap + Lc + G |
| 19 | GH05 | Mibale | lava flow | 0·71 | Ol + Cpx + Phl + Lc | Phl + Sa + Cpx + Lc |
| 19 | GH09 | Mibale | lava flow | 0·77 | Phl + Cpx + Sa | Sa + Cpx + Fe–Ti |
| 21 | ZFC004 | Chazi | lava flow | 0·75 | Phl + Cpx | Phl + Sa + G + Fe–Ti |
| 21 | ZFC008 | Chazi | lava flow | 0·72 | Ol + Cpx | Phl + Cpx + Ol + G |
| 21 | ZFC009 | Chazi | lava flow | 0·76 | Phl + Cpx + Lc | Cpx + Ol + Lc |
| 22 | GB036 | Pabbai | dyke | 0·75 | Phl + Ol + Cpx | Phl + Cpx + Ol + Sa |
| 4* | XB1307 | Xungba | lava flow | 0·72 | Cpx + Ol + Phl | Cpx + Ol + Phl + Sa + Fe–Ti |
| 11* | SLP1314 | Sailipu | lava flow | 0·80 | Ol + Phl + Cpx | Ol + Phl + Cpx + Fe–Ti |
| 11 | SLP1302 | Sailipu | lava flow | 0·77 | Ol + Phl + Cpx | Phl + Cpx + Sa + Ap |
| 11 | SLP1308 | Sailipu | lava flow | 0·73 | Phl + Cpx + Ol | Phl + Cpx + Ap + Fe–Ti |
| 11 | SLP1320 | Sailipu | lava flow | 0·77 | Ol + Phl + Cpx | Ol + Phl + Cpx + Lc + G |
| 12 | BGS1306 | Zabuye | lava flow | 0·69 | Phl + Cpx | Phl + Cpx + Ap + Fe–Ti |
| 13* | MG1301 | Maiga | plug | 0·81 | Ol + Cpx | Ol + Cpx + Ap + Fe–Ti |
| 13* | MG1303 | Maiga | lava flow | 0·82 | Ol + Cpx | Ol + Cpx + Ap |

Field number refers to number of the volcanic field in Fig. 1. Field name corresponds to that in Fig. 1. Ap, apatite; Cpx, clinopyroxene; Fe–Ti, Fe–Ti oxides; G, glass; Lc, leucite; Ol, olivine; Phl, phlogopite; Pl, plagioclase; Sa, sanidine. Samples (XB1307, SLP1314, SLP1302, SLP1308, SLP1320, BGS1306, MG1301, MG1303) have been analysed for olivine phenocryst compositions (Supplementary Data Appendix A).

*Samples contain xenocrystic olivine.

Table 5. Detailed sample preparation and analytical procedures for the Sr–Nd–Pb isotope measurements follow those of Guo *et al.* (2006, 2013).

### Olivine composition analyses

Compositions of olivine phenocrysts and xenocrysts were analyzed by electron microprobe (JEOLJXA-8100) at the IGGCAS. Operating conditions were 15 kV accelerating voltage, 10–20 nA beam current, 3–5 μm beam diameter and 15–20 s counting time. Well-defined natural and synthetic mineral standards were used for calibration. The analytical errors are generally less than 2%. Olivine compositions are reported in Supplementary Data Appendix A (supplementary data are available for downloading at http://www.petrology.oxfordjournals.org). The detailed analytical procedures follow those of Ding *et al.* (2003) and Wang *et al.* (2014*b*).

## RESULTS

### Major element characteristics

The ultrapotassic mafic magmatic rocks have relatively high Mg-numbers [molar Mg × 100/(Mg + Fe$^{2+}$) = 70–88, calculated assuming $Fe_2O_3/(FeO + Fe_2O_3) = 0{\cdot}20$], MgO

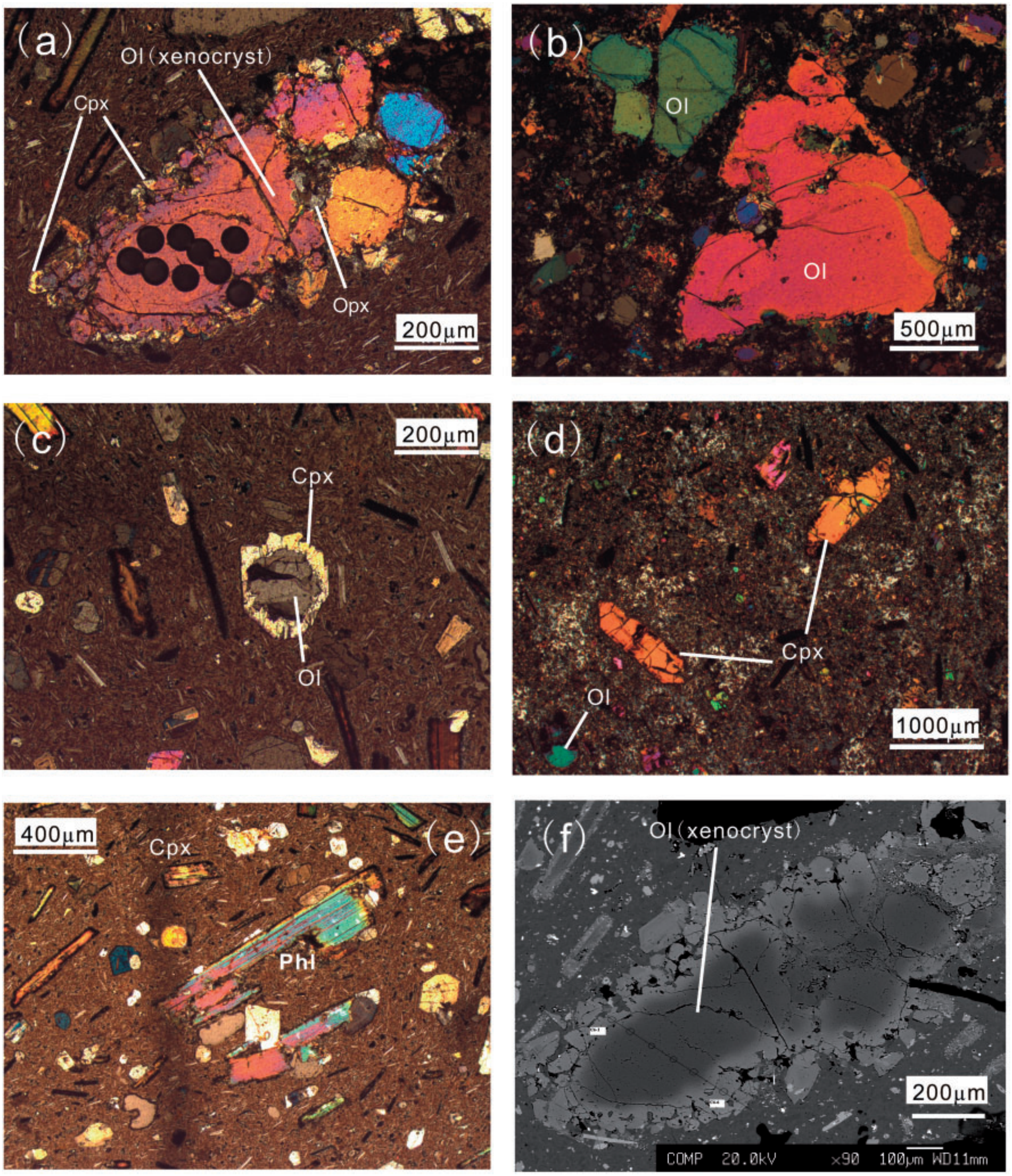

**Fig. 3.** Representative photomicrographs (a–e) of the ultrapotassic mafic volcanic rocks studied. (a) A complex reaction rim around a mantle olivine xenocryst from sample XB1307 from the Xungba volcanic field; this includes both orthopyroxene (Ca-poor pyroxene) and clinopyroxene (Ca-rich diopside) (cross-polarized light). This may be a fragment of the source olivine-bearing pyroxenite. Black circles represent points of electron microprobe analyses. (b) Corroded olivine phenocryst in sample MG1303 from the Maiga volcanic field (cross-polarized light). (c) Reaction rim of clinopyroxene on an olivine xenocryst in sample XB1307 from the Xungba volcanic field (cross-polarized light). (d) Phenocrysts of clinopyroxene and olivine in sample MG1301 from the Maiga volcanic field (cross-polarized light). (e) Phenocrysts of clinopyroxene and phlogopite in sample XB1307 from the Xungba volcanic field (cross-polarized light). (f) Back-scattered electron (BSE) image of the olivine grain in (a) clearly showing the xenocrystic olivine core (darker grey). Cpx, clinopyroxene; Ol, olivine; Opx, orthopyroxene; Phl, phlogopite.

contents (6·28–15·75 wt %) and Ni (106–527 ppm) concentrations (Table 3). The studied samples are thus considered to have relatively primitive compositions, minimizing the likelihood of significant crustal contamination and modification by magmatic differentiation. Although an $Fe_2O_3/(FeO + Fe_2O_3)$ ratio of 0·20 might be considered high, this is consistent with the observations of Brounce *et al.* (2014), who demonstrated that subduction-related magmas are more oxidizing.

The whole-rock geochemical data (Table 3) indicate that all the studied samples are ultrapotassic, with $K_2O > 3$ wt %, $MgO > 3$ wt % and $K_2O/Na_2O$ ratios ranging from 2·1 to 8·7 (wt %), based on the criteria of Foley *et al.* (1987) and Woolley *et al.* (1996). The studied rocks

**Table 3**: Major and trace element analyses of the K-rich mafic magmatic rocks in south Tibet

| Field no.: | 1 | 1 | 1 | 1 | 1 | 1 | 1 | 3 |
|---|---|---|---|---|---|---|---|---|
| Sample no.: | GZ-S05 | GZ-S06 | GZ-S12 | GZ-S15 | GZ-S27 | SQH-08 | SQH-15 | 16YS |
| Field name: | Shiquanhe | Shiquanhe | Shiquanhe | Shiquanhe | Shiquanhe | Shiquanhe | Shiquanhe | Bongba |
| Lat. (N): | 32°28′12″ | 32°28′33·6″ | 32°47′27·6″ | 32°31′8·4″ | 32°38′52·8″ | 32°48′57·6″ | 32°28′1·2″ | 32°6′3·6″ |
| Long. (E): | 80°6′0″ | 80°12′36″ | 80°10′48″ | 80°7′1·2″ | 80°3′36″ | 80°8′49·2″ | 80°16′44·4″ | 81°19′51·6″ |
| Age (Ma): | 22·5 | 22·5 | 22·5 | 22·5 | 22·5 | 22·5 | 22·5 | 24·4 |
| $SiO_2$ | 55·97 | 56·35 | 59·74 | 57·01 | 54·90 | 57·23 | 57·47 | 56·65 |
| $TiO_2$ | 0·93 | 1·26 | 0·56 | 1·17 | 0·90 | 1·58 | 1·35 | 1·52 |
| $Al_2O_3$ | 11·55 | 12·14 | 12·81 | 13·35 | 12·92 | 11·45 | 12·15 | 11·61 |
| $TFe_2O_3$* | 6·77 | 6·84 | 5·55 | 7·19 | 6·92 | 5·14 | 6·37 | 6·69 |
| MnO | 0·14 | 0·12 | 0·07 | 0·08 | 0·13 | 0·08 | 0·07 | 0·16 |
| MgO | 6·96 | 7·16 | 7·04 | 6·83 | 7·34 | 7·47 | 7·21 | 8·23 |
| CaO | 8·03 | 7·32 | 5·59 | 4·75 | 5·45 | 7·01 | 8·05 | 6·57 |
| $Na_2O$ | 2·57 | 2·15 | 2·50 | 2·05 | 2·39 | 3·01 | 2·16 | 1·74 |
| $K_2O$ | 6·21 | 5·78 | 5·18 | 6·87 | 8·05 | 6·51 | 4·76 | 5·92 |
| $P_2O_5$ | 0·87 | 0·88 | 0·97 | 0·71 | 0·99 | 0·53 | 0·41 | 0·92 |
| LOI | 1·69 | 2·15 | 1·08 | 0·69 | 1·07 | 1·34 | 0·89 | 1·47 |
| Mg-no. | 0·72 | 0·72 | 0·76 | 0·70 | 0·72 | 0·78 | 0·74 | 0·75 |
| La | 59·1 | 55·4 | 56·3 | 40·7 | 51·6 | 50·8 | 46·2 | 68·2 |
| Ce | 142 | 143 | 131 | 108 | 135 | 124 | 116 | 179 |
| Pr | 17·4 | 19·2 | 17·4 | 14·9 | 21·3 | 18·0 | 17·1 | 25·7 |
| Nd | 65·3 | 78·4 | 69·0 | 60·8 | 83·2 | 75·2 | 71·3 | 103 |
| Sm | 12·1 | 19·6 | 16·4 | 16·3 | 19·4 | 18·1 | 17·9 | 23·8 |
| Eu | 1·84 | 2·45 | 2·15 | 3·06 | 2·73 | 2·21 | 2·52 | 2·38 |
| Gd | 6·89 | 10·1 | 8·58 | 11·7 | 12·6 | 10·8 | 11·9 | 12·0 |
| Tb | 0·83 | 1·17 | 0·95 | 1·04 | 1·16 | 1·27 | 1·35 | 1·19 |
| Dy | 4·10 | 5·32 | 4·47 | 4·65 | 4·88 | 5·63 | 5·19 | 5·75 |
| Ho | 0·70 | 0·75 | 0·73 | 0·72 | 0·73 | 0·91 | 0·87 | 0·82 |
| Er | 1·74 | 1·63 | 1·71 | 1·58 | 1·60 | 2·24 | 1·92 | 1·69 |
| Tm | 0·26 | 0·22 | 0·24 | 0·20 | 0·21 | 0·30 | 0·28 | 0·23 |
| Yb | 1·66 | 1·43 | 1·52 | 1·26 | 1·28 | 1·87 | 1·93 | 1·41 |
| Lu | 0·25 | 0·21 | 0·23 | 0·19 | 0·20 | 0·29 | 0·30 | 0·22 |
| Sc | 17·6 | 33·3 | 10·3 | 38·8 | 21·6 | 28·4 | 19·1 | 23·5 |
| V | 108 | 139 | 168 | 146 | 125 | 153 | 171 | 114 |
| Cr | 390 | 473 | 563 | 453 | 422 | 362 | 443 | 513 |
| Co | 35·3 | 39·2 | 42·4 | 32·5 | 27·7 | 50·4 | 42·3 | 26·2 |
| Ni | 364 | 362 | 408 | 350 | 273 | 236 | 319 | 395 |
| Cu | 53·9 | 69·1 | 64·4 | 76·9 | 58·9 | 35·1 | 54·1 | 46·8 |
| Zn | 61·0 | 84·7 | 69·4 | 92·6 | 63·3 | 61·3 | 103 | 68·3 |
| Ga | 22·2 | 24·2 | 24·4 | 23·6 | 18·8 | 21·1 | 23·4 | 19·8 |
| Rb | 683 | 1030 | 674 | 719 | 643 | 672 | 841 | 917 |
| Sr | 503 | 683 | 481 | 735 | 691 | 411 | 331 | 464 |
| Y | 23·4 | 22·0 | 17·9 | 15·7 | 16·6 | 21·9 | 28·6 | 17·9 |
| Zr | 461 | 505 | 450 | 374 | 495 | 355 | 476 | 495 |
| Nb | 24·2 | 28·8 | 25·2 | 28·7 | 34·9 | 29·7 | 35·8 | 22·6 |
| Ba | 2138 | 3216 | 2320 | 1369 | 1407 | 2335 | 2969 | 2409 |
| Hf | 12·6 | 13·0 | 9·16 | 10·2 | 13·5 | 12·3 | 11·7 | 13·1 |
| Ta | 1·78 | 1·57 | 1·88 | 1·54 | 1·63 | 1·86 | 1·79 | 1·43 |
| Pb | 56·1 | 57·3 | 70·6 | 39·3 | 34·3 | 42·0 | 59·8 | 61·1 |
| Th | 128 | 221 | 112 | 232 | 174 | 185 | 135 | 184 |
| U | 14·5 | 21·4 | 20·9 | 18·4 | 23·0 | 16·8 | 16·5 | 21·8 |

(continued)

plot almost totally within the basaltic trachyandesite and trachyandesite fields (S2, S3) in an $Na_2O + K_2O$ versus $SiO_2$ classification diagram (Fig. 4a) and in the shoshonitic field in a plot of $K_2O$ versus $SiO_2$ (Fig. 4b), following the criteria of Peccerillo & Taylor (1976). Rare silica-poor samples plot in the basanite–tephrite field (U1, U2). Following the classification scheme of Foley *et al.* (1987), most of the post-collisional magmatic rocks studied are lamproitic, although they straddle the boundary between lamproites and Roman Province ultrapotassic rocks (Fig. 5).

With decreasing MgO contents, $SiO_2$, $Al_2O_3$ and $Na_2O$ abundances increase, but show considerable scatter at MgO < 10 wt %; CaO decreases, whereas $Fe_2O_3(T)$ is relatively constant (Fig. 6). The data suggest a role for both olivine and clinopyroxene fractionation from the most primitive magmas (MgO > 6 wt %). Whole-rock $K_2O$ contents are relatively constant at about 6–8 wt %, regardless of MgO variations, suggesting buffering by phlogopite (or amphibole) during partial melting of the mantle source. This is consistent with the presence of phlogopite phenocrysts in the ultrapotassic magmatic rocks (Table 2 and Fig. 3e).

## Trace element characteristics

The studied samples have light REE (LREE) enriched but relatively flat heavy REE (HREE) patterns and distinct negative Eu anomalies (Fig. 7). The REE patterns have a

**Table 3**: Continued

| Field no.: | 3 | 3 | 3 | 3 | 4 | 4 | 4 | 4 |
|---|---|---|---|---|---|---|---|---|
| Sample no.: | 20YS | 23YS | 25YS | JS07 | 99-B06 | 99-B09 | 99-B23 | 99-C12 |
| Field name: | Bongba | Bongba | Bongba | Bongba | Xungba | Xungba | Xungba | Xungba |
| Lat. (N): | 32°8′27·6″ | 32°12′14·4″ | 32°4′1·2″ | 32°4′55·2″ | 32°0·72′ | 32°3′39·6″ | 32°0·24′ | 32°2′27·6″ |
| Long. (E): | 81°22′19·2″ | 81°27′54″ | 81°21′50·4″ | 81°25′4·8″ | 81°47′27·6″ | 81°54′14·4″ | 81°52°33·6″ | 81°54′3·6″ |
| Age (Ma): | 24·4 | 24·4 | 24·4 | 24·4 | 22·6 | 22·6 | 22·6 | 22·6 |
| $SiO_2$ | 59·17 | 57·55 | 55·12 | 58·03 | 55·43 | 58·14 | 56·41 | 53·73 |
| $TiO_2$ | 1·10 | 1·19 | 1·19 | 1·25 | 1·47 | 1·24 | 1·06 | 0·98 |
| $Al_2O_3$ | 12·27 | 12·59 | 11·59 | 12·00 | 11·99 | 12·67 | 13·47 | 13·67 |
| $TFe_2O_3$* | 5·76 | 6·68 | 6·91 | 6·30 | 6·05 | 6·15 | 6·11 | 7·14 |
| MnO | 0·11 | 0·12 | 0·12 | 0·15 | 0·12 | 0·08 | 0·12 | 0·13 |
| MgO | 6·79 | 6·90 | 9·45 | 7·33 | 9·62 | 6·84 | 7·09 | 8·11 |
| CaO | 5·62 | 5·73 | 6·78 | 6·15 | 6·55 | 4·39 | 4·98 | 5·41 |
| $Na_2O$ | 2·83 | 2·72 | 1·92 | 2·18 | 2·12 | 2·30 | 2·24 | 2·27 |
| $K_2O$ | 5·97 | 6·16 | 6·07 | 5·36 | 5·48 | 7·34 | 7·69 | 7·86 |
| $P_2O_5$ | 0·38 | 0·35 | 0·86 | 1·23 | 1·16 | 0·86 | 0·83 | 0·69 |
| LOI | 1·28 | 0·63 | 0·92 | 1·45 | 1·59 | 1·64 | 1·87 | 0·91 |
| Mg-no. | 0·74 | 0·72 | 0·77 | 0·74 | 0·80 | 0·73 | 0·74 | 0·74 |
| La | 90·4 | 85·2 | 80·0 | 65·4 | 84·7 | 97·5 | 113 | 95·4 |
| Ce | 209 | 226 | 198 | 163 | 204 | 245 | 273 | 234 |
| Pr | 27·2 | 29·3 | 25·2 | 22·4 | 29·8 | 33·4 | 39·1 | 33·6 |
| Nd | 106 | 111 | 82·7 | 86·4 | 132 | 138 | 158 | 143 |
| Sm | 25·1 | 24·7 | 16·8 | 19·9 | 30·5 | 32·5 | 37·7 | 33·2 |
| Eu | 3·82 | 2·77 | 2·71 | 2·66 | 4·47 | 4·39 | 4·38 | 4·69 |
| Gd | 19·0 | 17·2 | 13·4 | 11·2 | 17·6 | 18·5 | 19·8 | 20·3 |
| Tb | 1·62 | 1·79 | 1·48 | 1·24 | 1·84 | 1·74 | 1·95 | 1·82 |
| Dy | 5·34 | 6·58 | 6·96 | 5·62 | 7·05 | 7·02 | 6·34 | 6·21 |
| Ho | 0·89 | 0·96 | 1·04 | 0·96 | 0·85 | 1·15 | 0·92 | 0·95 |
| Er | 2·04 | 2·16 | 2·35 | 2·24 | 1·68 | 2·39 | 2·25 | 2·26 |
| Tm | 0·29 | 0·32 | 0·31 | 0·29 | 0·23 | 0·33 | 0·32 | 0·31 |
| Yb | 1·94 | 2·19 | 2·06 | 1·94 | 1·53 | 1·99 | 1·98 | 2·17 |
| Lu | 0·32 | 0·30 | 0·31 | 0·32 | 0·25 | 0·29 | 0·29 | 0·32 |
| Sc | 28·9 | 29·0 | 21·1 | 27·8 | 38·3 | 19·2 | 26·2 | 23·5 |
| V | 267 | 246 | 136 | 148 | 318 | 198 | 119 | 137 |
| Cr | 459 | 563 | 584 | 655 | 584 | 352 | 419 | 527 |
| Co | 68·5 | 54·2 | 32·3 | 48·3 | 61·4 | 25·6 | 27·1 | 29·4 |
| Ni | 523 | 421 | 347 | 434 | 527 | 317 | 247 | 324 |
| Cu | 51·4 | 76·9 | 63·8 | 71·5 | 61·1 | 62·5 | 57·9 | 82·0 |
| Zn | 83·1 | 70·4 | 72·2 | 65·2 | 50·1 | 58·3 | 69·2 | 73·9 |
| Ga | 22·8 | 25·6 | 21·5 | 23·9 | 21·1 | 19·8 | 20·8 | 21·5 |
| Rb | 1428 | 1098 | 840 | 1025 | 916 | 675 | 719 | 759 |
| Sr | 435 | 452 | 615 | 657 | 809 | 716 | 1079 | 829 |
| Y | 20·1 | 22·0 | 21·4 | 18·3 | 16·6 | 23·1 | 21·1 | 25·2 |
| Zr | 401 | 386 | 480 | 416 | 538 | 718 | 580 | 635 |
| Nb | 26·3 | 21·6 | 16·1 | 21·7 | 25·3 | 24·0 | 24·2 | 12·9 |
| Ba | 3128 | 2899 | 2358 | 2944 | 2520 | 3418 | 3625 | 3124 |
| Hf | 11·0 | 13·4 | 11·5 | 19·3 | 13·5 | 20·4 | 13·7 | 17·9 |
| Ta | 1·96 | 2·51 | 0·77 | 2·41 | 1·68 | 1·81 | 1·58 | 1·13 |
| Pb | 79·3 | 81·4 | 58·6 | 76·5 | 86·7 | 93·8 | 73·3 | 85·3 |
| Th | 185 | 149 | 173 | 156 | 162 | 186 | 174 | 168 |
| U | 18·7 | 18·9 | 24·4 | 19·1 | 24·9 | 21·4 | 22·2 | 18·3 |

(continued)

very distinctive inverted 'spoon shape', which appears to be typical of collision-related ultrapotassic magmas (Davidson *et al.*, 2013). Primitive mantle-normalized incompatible element patterns (Fig. 8) are distinguished by significantly negative Nb–Ta–Ti and Sr–Ba–P anomalies and positive anomalies in large ion lithophile elements (LILE) (e.g. Rb, Pb, U and Th), despite the high concentrations of Nb, Ta and Ti (Table 3). One possible interpretation for the significant Nb–Ta–Ti anomalies would be the presence of residual high field strength element (HFSE)-rich mineral phases (e.g. titanite, rutile) in the mantle source because of their high partition coefficients for the HFSE. Similar trace element patterns have been observed in lamproites from SE Spain (Nixon *et al.*, 1984; Contini *et al.*, 1993; Prelević *et al.*, 2008; Conticelli *et al.*, 2009) and central Italy (Rogers *et al.*, 1985; Gasperini *et al.*, 2002; Perini *et al.*, 2004; Owen, 2008; Boari *et al.*, 2009; Conticelli *et al.*, 2009), which formed during the same Alpine–Himalayan orogenic cycle. A positive correlation between La/Yb and La (Fig. 9) suggests that the degree of partial melting of the mantle source decreases from west to east.

Mantle-derived magmas produced by partial melting of phlogopite-bearing source regions are higher in Rb/Sr and lower in Ba/Rb compared with those in equilibrium with amphibole-bearing sources (Furman & Graham, 1999). The whole-rock data indicate that both phlogopite and amphibole may have been present in

**Table 3**: Continued

| Field no.: | 11 | 11 | 11 | 11 | 12 | 12 | 12 | 12 |
|---|---|---|---|---|---|---|---|---|
| Sample no.: | 99-C15 | 99-C28 | XB-06 | XB-24 | BG015 | BG026 | BG037 | BG201 |
| Field name: | Sailipu | Sailipu | Sailipu | Sailipu | Zabuye | Zabuye | Zabuye | Zabuye |
| Lat. (N): | 31°18′6·13″ | 31°20′46·51″ | 31°24′50·29″ | 31°20′13·42″ | 31°26′24″ | 31°23′48″ | 31°24′24″ | 31°24′18″ |
| Long. (E): | 82°44′50·35″ | 82°58′28·4″ | 82°45′23·43″ | 82°52′37·16″ | 84°23′54″ | 84°18′6″ | 84°18′12″ | 84°18′18″ |
| Age (Ma): | 16·97 | 16·97 | 16·97 | 16·97 | 16·02 | 16·02 | 16·02 | 16·02 |
| $SiO_2$ | 55·45 | 58·02 | 54·64 | 56·78 | 53·73 | 54·23 | 53·87 | 54·29 |
| $TiO_2$ | 1·66 | 1·29 | 1·49 | 1·52 | 1·13 | 0·91 | 1·52 | 1·38 |
| $Al_2O_3$ | 13·48 | 13·61 | 12·99 | 11·47 | 13·91 | 11·73 | 13·57 | 12·08 |
| $TFe_2O_3$* | 6·35 | 6·34 | 6·14 | 5·98 | 4·58 | 6·62 | 5·50 | 7·28 |
| MnO | 0·11 | 0·09 | 0·12 | 0·13 | 0·26 | 0·12 | 0·15 | 0·13 |
| MgO | 8·08 | 8·28 | 7·97 | 8·75 | 8·91 | 9·14 | 7·49 | 7·58 |
| CaO | 5·86 | 4·25 | 5·62 | 4·85 | 7·24 | 7·25 | 6·50 | 7·73 |
| $Na_2O$ | 1·90 | 1·65 | 2·71 | 2·29 | 1·59 | 1·78 | 1·78 | 1·27 |
| $K_2O$ | 6·47 | 5·75 | 7·50 | 6·96 | 7·46 | 7·09 | 8·27 | 7·07 |
| $P_2O_5$ | 0·63 | 0·73 | 0·82 | 1·28 | 1·18 | 1·13 | 1·34 | 1·19 |
| LOI | 0·92 | 1·63 | 1·85 | 1·79 | 1·83 | 0·76 | 1·68 | 1·84 |
| Mg-no. | 0·76 | 0·76 | 0·76 | 0·78 | 0·83 | 0·77 | 0·77 | 0·72 |
| La | 90·2 | 78·4 | 109 | 84·1 | 97·5 | 127 | 74·1 | 82·9 |
| Ce | 237 | 202 | 287 | 225 | 262 | 324 | 189 | 190 |
| Pr | 34·9 | 29·2 | 42·3 | 33·2 | 33·8 | 46·6 | 27·0 | 26·3 |
| Nd | 161 | 138 | 187 | 152 | 125 | 204 | 111 | 108 |
| Sm | 38·4 | 36·4 | 49·0 | 40·6 | 28·0 | 43·4 | 25·2 | 23·1 |
| Eu | 6·18 | 4·51 | 6·73 | 7·06 | 4·47 | 4·63 | 3·78 | 4·12 |
| Gd | 26·2 | 22·6 | 27·2 | 32·9 | 17·6 | 14·3 | 12·3 | 11·9 |
| Tb | 2·52 | 1·48 | 2·43 | 2·37 | 1·83 | 1·74 | 1·43 | 1·46 |
| Dy | 6·84 | 5·04 | 6·41 | 7·92 | 8·52 | 7·89 | 6·39 | 5·57 |
| Ho | 0·78 | 0·66 | 0·72 | 1·22 | 1·28 | 1·24 | 1·02 | 0·85 |
| Er | 1·92 | 1·53 | 1·63 | 2·78 | 2·87 | 2·55 | 2·31 | 2·03 |
| Tm | 0·26 | 0·21 | 0·23 | 0·36 | 0·34 | 0·31 | 0·28 | 0·29 |
| Yb | 1·68 | 1·37 | 1·45 | 2·29 | 1·86 | 1·77 | 1·61 | 1·93 |
| Lu | 0·23 | 0·21 | 0·22 | 0·33 | 0·26 | 0·24 | 0·20 | 0·29 |
| Sc | 19·8 | 24·2 | 17·3 | 16·3 | 21·6 | 21·0 | 19·2 | 17·1 |
| V | 172 | 153 | 164 | 183 | 126 | 116 | 119 | 159 |
| Cr | 538 | 332 | 429 | 358 | 553 | 493 | 361 | 348 |
| Co | 40·5 | 25·9 | 24·5 | 39·2 | 33·2 | 35·1 | 26·8 | 41·2 |
| Ni | 387 | 263 | 347 | 353 | 465 | 315 | 475 | 390 |
| Cu | 42·2 | 39·6 | 52·0 | 66·6 | 76·8 | 53·3 | 72·0 | 68·3 |
| Zn | 69·5 | 101 | 50·3 | 91·7 | 52·7 | 37·2 | 46·2 | 34·3 |
| Ga | 23·2 | 24·6 | 23·9 | 26·4 | 21·1 | 19·4 | 20·9 | 24·2 |
| Rb | 867 | 643 | 827 | 709 | 621 | 710 | 583 | 457 |
| Sr | 801 | 672 | 637 | 758 | 1638 | 1619 | 1696 | 1718 |
| Y | 18·5 | 16·9 | 19·1 | 36·9 | 20·1 | 25·3 | 15·8 | 32·7 |
| Zr | 637 | 569 | 613 | 784 | 421 | 483 | 386 | 415 |
| Nb | 18·3 | 41·4 | 13·3 | 16·4 | 36·6 | 10·2 | 42·0 | 41·0 |
| Ba | 2113 | 2110 | 2508 | 2739 | 3351 | 3817 | 2634 | 2351 |
| Hf | 9·03 | 14·9 | 19·8 | 20·3 | 12·2 | 6·56 | 12·1 | 10·4 |
| Ta | 1·51 | 2·67 | 1·24 | 1·65 | 1·89 | 0·58 | 2·33 | 2·75 |
| Pb | 71·1 | 84·2 | 73·8 | 79·7 | 86·3 | 89·2 | 80·4 | 72·9 |
| Th | 212 | 253 | 279 | 289 | 95·2 | 102 | 83·5 | 70·2 |
| U | 36·2 | 37·4 | 39·3 | 41·2 | 13·5 | 7·21 | 12·4 | 14·6 |

(continued)

the mantle source region (Fig. 10), but that phlogopite dominates.

The studied mafic ultrapotassic rocks have flatter LREE patterns in the west than those in the east of the Lhasa terrane (Fig. 7). In addition, some trace element ratios (e.g. Th/La, Sm/La, Ba/La, Th/Yb, Th/Nd) display a decreasing trend from west to east (Fig. 11).

## Sr–Nd–Pb isotopes

The ultrapotassic mafic magmatic rocks have extremely radiogenic ($^{87}Sr/^{86}Sr$)$_i$ (0·712379–0·737616) and unradiogenic ($^{143}Nd/^{144}Nd$)$_i$ (0·511662–0·511984) compositions relative to Bulk Silicate Earth, and high ($^{207}Pb/^{204}Pb$)$_i$ (15·65–15·87) and ($^{208}Pb/^{204}Pb$)$_i$ (39·02–39·76) at a given ($^{206}Pb/^{204}Pb$)$_i$ (18·30–18·92) compared with the Northern Hemisphere Reference Line (NHRL; Hart, 1984) (Fig. 12). The data exhibit coherent trends between depleted mid-ocean ridge basalt (MORB)-source mantle (DMM) and Indian continental crust [proxied by the isotopic composition of the Higher Himalayan Crystalline Series (HHCS) (Pan *et al.*, 2004; Richards *et al.*, 2005; Guo *et al.*, 2013); see Pan *et al.* (2004) and Richards *et al.* (2005) and references therein for more detailed discussion] in the Sr–Nd–Pb isotope profiles (Fig. 12). There is a trend of increasing ($^{143}Nd/^{144}Nd$)$_i$ and decreasing ($^{87}Sr/^{86}Sr$)$_i$ and ($^{206}Pb/^{204}Pb$)$_i$ from west to east (Fig. 11). The Sr–Nd–Pb isotope compositions are similar to those of mafic ultrapotassic magmatic rocks from SE Spain

**Table 3**: Continued

| Field no.: | 12 | 13 | 13 | 13 | 13 | 16 | 16 | 17 |
|---|---|---|---|---|---|---|---|---|
| Sample no.: | BG203 | MG-008 | MG-012 | MG-015 | MG-016 | GZF3 | GZF9 | G-029 |
| Field name: | Zabuye | Maiga | Maiga | Maiga | Maiga | Garwa | Garwa | Yaqian |
| Lat. (N): | 31°24′24″ | 30°48′45·27″ | 30°48′45·27″ | 30°49′22·31″ | 30°49′22·31″ | 31°16′4·8″ | 31°15′14·4″ | 30°56′40·8″ |
| Long. (E): | 84°18′18″ | 84°25′47·59″ | 84°25′47·59″ | 84°25′20·46″ | 84°25′20·46″ | 86°33′57·6″ | 86°34′48·36″ | 86°23′33·46″ |
| Age (Ma): | 16·02 | 16·7 | 16·7 | 16·7 | 16·7 | 20·35 | 20·35 | 13·70 |
| $SiO_2$ | 53·40 | 53·62 | 52·65 | 54·95 | 53·11 | 55·59 | 55·13 | 55·97 |
| $TiO_2$ | 1·12 | 1·52 | 1·27 | 1·32 | 1·38 | 1·67 | 1·70 | 1·58 |
| $Al_2O_3$ | 11·69 | 11·85 | 11·12 | 10·86 | 12·01 | 12·40 | 12·54 | 11·97 |
| $TFe_2O_3$* | 6·17 | 4·62 | 6·35 | 6·20 | 7·16 | 5·55 | 6·47 | 5·60 |
| MnO | 0·15 | 0·15 | 0·11 | 0·08 | 0·14 | 0·12 | 0·13 | 0·05 |
| MgO | 9·83 | 13·10 | 11·29 | 9·33 | 9·26 | 8·63 | 7·43 | 8·33 |
| CaO | 7·45 | 4·65 | 6·73 | 6·72 | 6·94 | 4·59 | 6·19 | 6·96 |
| $Na_2O$ | 1·61 | 2·17 | 1·66 | 1·50 | 1·40 | 1·39 | 1·42 | 1·30 |
| $K_2O$ | 7·63 | 7·12 | 7·65 | 7·75 | 7·28 | 8·89 | 7·99 | 7·43 |
| $P_2O_5$ | 0·94 | 1·19 | 1·16 | 1·29 | 1·32 | 1·18 | 1·00 | 0·81 |
| LOI | 1·24 | 1·68 | 0·84 | 1·57 | 1·96 | 1·38 | 1·85 | 1·83 |
| Mg-no. | 0·80 | 0·88 | 0·81 | 0·79 | 0·76 | 0·79 | 0·74 | 0·79 |
| La | 101 | 96·8 | 163 | 148 | 153 | 271 | 267 | 353 |
| Ce | 263 | 257 | 435 | 412 | 398 | 574 | 545 | 735 |
| Pr | 38·9 | 35·5 | 66·3 | 61·5 | 56·8 | 76·5 | 72·9 | 91·6 |
| Nd | 173 | 148 | 297 | 284 | 244 | 285 | 280 | 359 |
| Sm | 36·3 | 32·2 | 57·2 | 54·6 | 51·9 | 38·8 | 51·2 | 64·4 |
| Eu | 4·68 | 5·16 | 7·48 | 7·76 | 7·19 | 5·49 | 6·84 | 6·18 |
| Gd | 15·0 | 16·8 | 25·1 | 26·0 | 24·3 | 15·6 | 31·6 | 16·6 |
| Tb | 1·71 | 1·95 | 2·44 | 2·28 | 2·43 | 1·36 | 2·63 | 1·58 |
| Dy | 7·63 | 7·84 | 8·73 | 7·89 | 8·64 | 5·03 | 6·51 | 6·15 |
| Ho | 1·19 | 1·16 | 1·28 | 1·16 | 1·26 | 0·70 | 0·78 | 0·84 |
| Er | 2·58 | 2·57 | 2·67 | 2·44 | 2·65 | 1·44 | 1·67 | 1·86 |
| Tm | 0·34 | 0·35 | 0·33 | 0·29 | 0·30 | 0·19 | 0·23 | 0·25 |
| Yb | 2·09 | 2·13 | 2·16 | 1·89 | 1·61 | 1·24 | 1·52 | 1·64 |
| Lu | 0·30 | 0·32 | 0·34 | 0·28 | 0·19 | 0·18 | 0·21 | 0·24 |
| Sc | 19·8 | 18·3 | 21·6 | 16·4 | 20·9 | 22·4 | 23·1 | 17·0 |
| V | 136 | 147 | 137 | 196 | 150 | 149 | 178 | 138 |
| Cr | 458 | 543 | 574 | 539 | 592 | 557 | 419 | 360 |
| Co | 42·8 | 32·7 | 40·7 | 34·0 | 35·8 | 47·9 | 26·2 | 46·8 |
| Ni | 327 | 379 | 401 | 357 | 441 | 296 | 211 | 218 |
| Cu | 45·9 | 44·2 | 59·6 | 38·7 | 72·3 | 61·4 | 56·0 | 62·2 |
| Zn | 49·2 | 97·3 | 47·0 | 33·0 | 82·4 | 87·3 | 65·3 | 71·5 |
| Ga | 22·8 | 26·8 | 22·4 | 19·4 | 25·8 | 19·4 | 24·5 | 25·9 |
| Rb | 553 | 521 | 532 | 537 | 610 | 371 | 324 | 463 |
| Sr | 1527 | 1339 | 1027 | 949 | 913 | 1448 | 1529 | 1420 |
| Y | 23·6 | 19·7 | 27·4 | 30·1 | 13·9 | 16·8 | 14·2 | 21·4 |
| Zr | 587 | 831 | 695 | 658 | 717 | 1515 | 1143 | 1038 |
| Nb | 43·4 | 32·1 | 31·6 | 28·4 | 29·7 | 80·3 | 61·1 | 63·0 |
| Ba | 3476 | 3603 | 2943 | 3153 | 4095 | 4820 | 3242 | 4179 |
| Hf | 8·98 | 28·7 | 23·1 | 18·9 | 25·7 | 49·0 | 36·3 | 27·4 |
| Ta | 2·44 | 2·77 | 1·95 | 1·81 | 2·45 | 5·51 | 5·42 | 3·82 |
| Pb | 82·1 | 109 | 113 | 115 | 101 | 125 | 102 | 189 |
| Th | 107 | 103 | 272 | 283 | 221 | 186 | 140 | 140 |
| U | 10·3 | 23·7 | 37·7 | 34·1 | 31·3 | 21·9 | 18·4 | 17·3 |

(continued)

(Nelson, 1992; Prelević *et al.*, 2008; Conticelli *et al.*, 2009) and central Italy (Gasperini *et al.*, 2002; Perini *et al.*, 2004; Owen, 2008; Boari *et al.*, 2009; Conticelli *et al.*, 2009) in Europe (Fig. 12), although with more radiogenic Sr isotope compositions.

## Olivine compositions

A positive correlation between olivine Fo content (mol %) and whole-rock Mg-number indicates that some of the olivine phenocrysts from the ultrapotassic mafic magmatic rocks are in equilibrium with the host magma, proxied by the bulk-rock composition (Fig. 13), based on the equilibrium Fe–Mg exchange coefficient ($K_D = 0{\cdot}3 \pm 0{\cdot}03$) between olivine and melt (Roeder & Emslie, 1970). Other olivine phenocrysts, however, have much lower Fo contents, which indicates crystallization from more evolved melts. The compositions of those olivine phenocrysts, which are in equilibrium with their host melts (bulk-rocks), may be used to provide constraints on the nature of the mantle source of the magmas (Foley *et al.*, 2013).

Previous studies (e.g. Prelević *et al.*, 2013) have indicated that mantle-derived olivine xenocrysts are characterized by low CaO contents (less than 0·1 wt %). In the Lhasa terrane ultrapotassic rocks the olivine xenocrysts exhibit distinct reaction rims with abrupt compositional changes between core and rim (Fig. 14), suggesting disequilibrium between the olivine xenocrysts and the

**Table 3**: Continued

| Field no.: | 17 | 19 | 19 | 21 | 21 | 21 | 22 | 4 |
|---|---|---|---|---|---|---|---|---|
| Sample no.: | GH03 | GH05 | GH09 | ZFC004 | ZFC008 | ZFC009 | GB036 | XB1307 |
| Field name: | Yaqian | Mibale | Mibale | Chazi | Chazi | Chazi | Pabbai | Xungba |
| Lat. (N): | 30°56′22·41″ | 30°50′54·29″ | 30°51′10·11″ | 30°50′41·34″ | 30°34′35·43″ | 30°07′12·47″ | 29°23′5·19″ | 31°58′41·68″ |
| Long. (E): | 86°23′31·04″ | 86°39′46·37″ | 86°40′10·27″ | 86°40′10·30″ | 86°41′20·41″ | 86°32′17·18″ | 86°43′18·35″ | 81°58′11·02″ |
| Age (Ma): | 13·70 | 15·29 | 15·29 | 11·50 | 11·50 | 11·50 | 14·80 | 22·6 |
| $SiO_2$ | 56·71 | 56·57 | 54·53 | 53·81 | 55·63 | 54·39 | 53·39 | 58·05 |
| $TiO_2$ | 1·61 | 1·54 | 1·60 | 1·73 | 1·56 | 1·57 | 1·27 | 1·11 |
| $Al_2O_3$ | 11·84 | 12·33 | 14·17 | 11·87 | 12·44 | 12·85 | 12·77 | 14·02 |
| $TFe_2O_3$* | 5·32 | 7·03 | 5·86 | 6·46 | 6·97 | 6·65 | 6·44 | 6·04 |
| MnO | 0·08 | 0·13 | 0·05 | 0·12 | 0·11 | 0·13 | 0·09 | 0·09 |
| MgO | 7·97 | 6·99 | 7·88 | 8·03 | 7·10 | 8·40 | 7·79 | 6·28 |
| CaO | 6·20 | 6·14 | 6·45 | 7·71 | 6·51 | 6·70 | 6·48 | 5·20 |
| $Na_2O$ | 1·53 | 1·62 | 1·36 | 2·34 | 1·75 | 1·73 | 2·45 | 2·53 |
| $K_2O$ | 8·02 | 6·71 | 6·91 | 6·77 | 6·86 | 6·41 | 8·10 | 5·87 |
| $P_2O_5$ | 0·72 | 0·95 | 1·19 | 1·16 | 1·07 | 1·16 | 1·20 | 0·81 |
| LOI | 1·52 | 1·67 | 1·89 | 2·27 | 1·83 | 2·36 | 3·25 | 1·06 |
| Mg-no. | 0·79 | 0·71 | 0·77 | 0·75 | 0·72 | 0·76 | 0·75 | 0·72 |
| La | 319 | 234 | 213 | 164 | 149 | 152 | 139 | 76·4 |
| Ce | 571 | 486 | 403 | 352 | 347 | 341 | 308 | 170 |
| Pr | 65·8 | 60·8 | 47·1 | 47·3 | 43·8 | 48·3 | 41·0 | 24·8 |
| Nd | 226 | 214 | 136 | 186 | 173 | 191 | 152 | 115 |
| Sm | 37·8 | 36·8 | 21·9 | 36·7 | 30·2 | 37·2 | 28·3 | 23·5 |
| Eu | 5·53 | 4·68 | 3·48 | 4·91 | 5·63 | 5·42 | 5·24 | 3·69 |
| Gd | 17·8 | 12·3 | 14·0 | 23·0 | 24·2 | 22·1 | 20·9 | 12·8 |
| Tb | 1·53 | 1·36 | 1·72 | 2·32 | 2·46 | 2·28 | 1·59 | 1·29 |
| Dy | 6·03 | 5·35 | 6·15 | 9·16 | 8·24 | 8·76 | 6·03 | 5·31 |
| Ho | 0·75 | 0·88 | 0·98 | 1·39 | 1·26 | 1·34 | 1·07 | 0·84 |
| Er | 1·55 | 2·05 | 2·26 | 3·16 | 2·67 | 2·91 | 2·43 | 2·02 |
| Tm | 0·21 | 0·29 | 0·28 | 0·38 | 0·33 | 0·35 | 0·32 | 0·27 |
| Yb | 1·32 | 1·98 | 1·77 | 2·31 | 1·96 | 2·19 | 2·13 | 1·66 |
| Lu | 0·20 | 0·28 | 0·27 | 0·34 | 0·29 | 0·31 | 0·31 | 0·25 |
| Sc | 18·3 | 16·3 | 19·3 | 19·8 | 18·4 | 19·0 | 22·7 | 17·6 |
| V | 136 | 144 | 171 | 120 | 133 | 148 | 172 | 124 |
| Cr | 356 | 515 | 590 | 574 | 486 | 536 | 465 | 244 |
| Co | 47·5 | 33·4 | 31·0 | 67·5 | 29·7 | 43·2 | 47·7 | 25·1 |
| Ni | 262 | 364 | 271 | 504 | 314 | 483 | 517 | 106 |
| Cu | 63·3 | 52·1 | 48·0 | 48·4 | 51·3 | 41·7 | 61·2 | 34·4 |
| Zn | 76·0 | 64·3 | 92·8 | 67·1 | 58·8 | 62·6 | 65·7 | 79·8 |
| Ga | 22·5 | 21·2 | 32·4 | 23·5 | 21·2 | 23·6 | 22·7 | 22·0 |
| Rb | 342 | 427 | 695 | 531 | 464 | 428 | 386 | 443 |
| Sr | 1294 | 1016 | 873 | 706 | 824 | 855 | 766 | 710 |
| Y | 15·0 | 28·7 | 33·9 | 34·9 | 32·3 | 35·4 | 25·7 | 19·3 |
| Zr | 890 | 844 | 729 | 729 | 571 | 893 | 564 | 372 |
| Nb | 62·4 | 62·7 | 57·2 | 43·2 | 31·7 | 59·4 | 19·3 | 23·4 |
| Ba | 3557 | 3069 | 2298 | 3271 | 2850 | 2713 | 2185 | 2268 |
| Hf | 25·8 | 25·6 | 16·4 | 23·8 | 20·0 | 26·4 | 11·7 | 10·9 |
| Ta | 4·81 | 3·02 | 2·18 | 1·98 | 2·01 | 3·39 | 1·51 | 1·40 |
| Pb | 191 | 94·6 | 110 | 120 | 128 | 115 | 83·2 | 53·3 |
| Th | 117 | 138 | 82·2 | 116 | 127 | 163 | 108 | 133 |
| U | 16·7 | 18·4 | 21·6 | 31·7 | 25·2 | 27·8 | 20·1 | 20·2 |

(continued)

host magma. The mantle olivine xenocrysts have high Fo [Fo (mol %) ~ 90] and low CaO (less than 0·1 wt %) contents in their cores (Fig. 14c), mantled by low-Fo (less than 80) and high-CaO (more than 0·15 wt %) rims (Fig. 14c).

The olivine phenocrysts have higher CaO (more than 0·1%) and MnO contents compared with the xenocrysts; Ni contents are more variable (Fig. 15). The olivine xenocrysts plot within a very restricted compositional range (CaO = 0·06–0·10 wt %, NiO = 0·31–0·51 wt %, MnO = 0·10–0·21 wt %). Some of the olivine phenocrysts in the most primitive ultrapotassic magmas (e.g. samples MG1303 and SLP1314; Table 3) are characterized by extremely high NiO contents (0·60–0·70 wt %) (Fig. 15c). This, together with low MnO and CaO contents (Fig. 15a and b), is consistent with an inference of pyroxenite as the mantle source of the host melts from which the olivine crystallized, as proposed in a number of recent studies (e.g. Sobolev *et al.*, 2005, 2007; Herzberg, 2011; Prelević *et al.*, 2013).

## DISCUSSION

Previous studies have shown that the post-collisional potassium-rich magmatism of the Tibetan Plateau can provide important constraints for understanding the geodynamic setting and evolution of the Plateau (e.g. Coulon *et al.*, 1986; Pearce & Mei, 1988; Arnaud *et al.*,

**Table 3**: Continued

| Field no.: | 11 | 11 | 11 | 11 | 12 | 13 | 13 |
|---|---|---|---|---|---|---|---|
| Sample no.: | SLP1314 | SLP1302 | SLP1308 | SLP1320 | BGS1306 | MG1301 | MG1303 |
| Field name: | Sailipu | Sailipu | Sailipu | Sailipu | Zabuye | Maiga | Maiga |
| Lat. (N): | 31°15′49·55″ | 31°26′7·37″ | 31°22′6·24″ | 31°17′38·64″ | 31°24′0·54″ | 30°48′16·08″ | 30°49′15·84″ |
| Long. (E): | 82°47′25·73″ | 82°44′20·23″ | 82°40′10·76″ | 82°58′29·64″ | 84°18′15·6″ | 84°26′23·94″ | 84°26′7·62″ |
| Age (Ma): | 16·97 | 16·97 | 16·97 | 16·97 | 16·02 | 16·7 | 16·7 |
| $SiO_2$ | 47·04 | 56·80 | 55·67 | 56·80 | 55·54 | 53·75 | 46·44 |
| $TiO_2$ | 1·44 | 1·54 | 1·56 | 1·42 | 1·26 | 1·54 | 1·20 |
| $Al_2O_3$ | 10·50 | 12·03 | 13·70 | 12·61 | 13·36 | 11·15 | 10·09 |
| $TFe_2O_3$* | 8·26 | 5·93 | 6·94 | 6·47 | 6·14 | 6·39 | 8·31 |
| MnO | 0·13 | 0·09 | 0·15 | 0·10 | 0·10 | 0·10 | 0·13 |
| MgO | 13·74 | 8·20 | 7·55 | 8·82 | 5·58 | 11·03 | 15·75 |
| CaO | 8·88 | 4·83 | 5·30 | 4·94 | 7·86 | 5·21 | 10·47 |
| $Na_2O$ | 0·91 | 2·13 | 2·71 | 1·95 | 2·89 | 1·61 | 0·90 |
| $K_2O$ | 7·89 | 7·29 | 5·61 | 6·04 | 6·10 | 7·97 | 5·73 |
| $P_2O_5$ | 1·21 | 1·18 | 0·82 | 0·86 | 1·16 | 1·25 | 0·98 |
| LOI | 1·36 | 0·86 | 0·26 | 0·32 | 2·08 | 0·22 | 2·20 |
| Mg-no· | 0·80 | 0·77 | 0·73 | 0·77 | 0·69 | 0·81 | 0·82 |
| La | 325 | 104 | 101 | 110 | 79·1 | 194 | 169 |
| Ce | 680 | 289 | 244 | 278 | 172 | 503 | 290 |
| Pr | 87·2 | 46·5 | 33·5 | 39·2 | 23·6 | 75·3 | 33·3 |
| Nd | 347 | 227 | 149 | 184 | 104 | 336 | 134 |
| Sm | 65·0 | 47·6 | 26·7 | 33·0 | 19·8 | 64·2 | 24·5 |
| Eu | 12·4 | 6·55 | 3·77 | 4·94 | 3·76 | 9·25 | 6·28 |
| Gd | 44·7 | 24·1 | 15·3 | 18·0 | 12·9 | 35·1 | 18·9 |
| Tb | 4·41 | 2·38 | 1·61 | 1·83 | 1·47 | 3·38 | 2·13 |
| Dy | 15·7 | 8·36 | 6·00 | 7·06 | 6·16 | 11·5 | 8·95 |
| Ho | 2·06 | 1·29 | 0·97 | 1·11 | 0·98 | 1·65 | 1·48 |
| Er | 4·44 | 2·97 | 2·32 | 2·69 | 2·28 | 3·61 | 3·47 |
| Tm | 0·47 | 0·37 | 0·30 | 0·34 | 0·30 | 0·41 | 0·44 |
| Yb | 2·59 | 2·18 | 1·80 | 2·08 | 1·79 | 2·41 | 2·57 |
| Lu | 0·34 | 0·31 | 0·26 | 0·31 | 0·26 | 0·33 | 0·37 |
| Sc | 26·6 | 18·2 | 16·4 | 20·2 | 16·7 | 22·6 | 27·6 |
| V | 172 | 112 | 127 | 136 | 131 | 143 | 148 |
| Cr | 499 | 460 | 289 | 503 | 144 | 717 | 516 |
| Co | 43·7 | 31·9 | 33·4 | 34·0 | 26·7 | 43·1 | 49·1 |
| Ni | 272 | 306 | 220 | 308 | 120 | 493 | 452 |
| Cu | 92·6 | 40·5 | 23·6 | 52·5 | 45·4 | 74·5 | 73·5 |
| Zn | 105 | 92·6 | 104 | 97·8 | 98·7 | 106 | 96·2 |
| Ga | 21·3 | 24·0 | 23·2 | 23·3 | 20·6 | 27·9 | 15·7 |
| Rb | 675 | 928 | 503 | 528 | 401 | 775 | 298 |
| Sr | 3476 | 732 | 912 | 931 | 1765 | 1264 | 3389 |
| Y | 51·8 | 33·4 | 24·4 | 27·4 | 24·8 | 39·5 | 36·4 |
| Zr | 538 | 722 | 618 | 598 | 340 | 908 | 311 |
| Nb | 22·1 | 35·2 | 34·9 | 35·2 | 31·0 | 41·0 | 11·9 |
| Ba | 10115 | 2795 | 2501 | 2400 | 3514 | 5323 | 14076 |
| Hf | 12·3 | 20·6 | 17·9 | 17·4 | 9·33 | 25·7 | 6·77 |
| Ta | 1·11 | 2·09 | 2·36 | 2·00 | 1·82 | 2·22 | 0·59 |
| Pb | 176 | 78·9 | 89·2 | 57·0 | 76·8 | 106 | 286 |
| Th | 172 | 299 | 131 | 186 | 69·0 | 336 | 83·4 |
| U | 16·0 | 40·6 | 15·6 | 23·2 | 17·8 | 42·5 | 11·9 |

Major element oxide contents are normalized to 100 wt % on a volatile-free basis. Field number refers to number of the volcanic field in Fig. 1. Age (Ma) is average value of the ages of the volcanic fields calculated from all of age data shown in Table 1. Mg-no. = Mg/(Mg + $Fe^{2+}$), calculated assuming $Fe_2O_3/(FeO + Fe_2O_3) = 0·20$. Samples (XB1307, SLP1314, SLP1302, SLP1308, SLP1320, BGS1306, MG1301, MG1303) have been analysed for olivine phenocryst compositions (Supplementary Data Appendix A).

*Total iron is given as $Fe_2O_3$.

1992; Turner *et al.*, 1993, 1996; Miller *et al.*, 1999; Williams *et al.*, 2001, 2004; Ding *et al.*, 2003; Nomade *et al.*, 2004; Mo *et al.*, 2006; Gao *et al.*, 2007; Zhao *et al.*, 2009*a*, *b*; Chen *et al.*, 2010; Wang *et al.*, 2012; Guo *et al.*, 2013, 2014). Primary magmas generated by equilibrium partial melting of peridotite in the upper mantle should have high Mg-numbers (>70) and high Ni concentrations (Frey *et al.*, 1978). The magmatic rocks in our study are considered to be candidates for primitive magmas because of their high MgO contents (6·28–15·75 wt %), high Mg-numbers (70–88), high Ni concentrations (106–527 ppm) (Table 3), and the presence of mantle-derived olivine xenocrysts (Figs 3 and 14) and rare mantle xenoliths (e.g. Liu *et al.*, 2011*a*, 2014*a*). Thus, their whole-rock major and trace element and Sr–Nd–Pb isotope compositions can be used to provide important constraints on the nature of their mantle source.

## Characteristics of the mantle source region of the primitive magmas

The ultrapotassic mafic magmatic rocks studied have distinct negative Nb–Ta–Ti anomalies and positive Pb

**Table 4**: Sr and Nd isotope compositions of the K-rich mafic magmatic rocks in south Tibet

| Field no. | Sample no. | Field name | $^{87}$Rb/$^{86}$Sr | $^{87}$Sr/$^{86}$Sr ± 2σ | ($^{87}$Sr/$^{86}$Sr)$_i$ | εSr(i) | $^{147}$Sm/$^{144}$Nd | $^{143}$Nd/$^{144}$Nd ± 2σ | ($^{143}$Nd/$^{144}$Nd)$_i$ | εNd(i) |
|---|---|---|---|---|---|---|---|---|---|---|
| 1 | GZ-S05 | Shiquanhe | 3·9444 | 0·736547 ± 13 | 0·735287 | 437·4 | 0·1117 | 0·511701 ± 7 | 0·511685 | –18·0 |
| 1 | GZ-S06 | Shiquanhe | 4·3681 | 0·725218 ± 11 | 0·723822 | 274·7 | 0·1510 | 0·511734 ± 9 | 0·511712 | –17·5 |
| 1 | GZ-S12 | Shiquanhe | 4·0669 | 0·738916 ± 10 | 0·737616 | 470·5 | 0·1439 | 0·511737 ± 6 | 0·511716 | –17·4 |
| 1 | GZ-S15 | Shiquanhe | 2·8370 | 0·737682 ± 12 | 0·736775 | 458·5 | 0·1621 | 0·511765 ± 9 | 0·511741 | –16·9 |
| 1 | GZ-S27 | Shiquanhe | 2·6983 | 0·732057 ± 16 | 0·731195 | 379·3 | 0·1405 | 0·511683 ± 11 | 0·511662 | –18·5 |
| 1 | SQH-08 | Shiquanhe | 4·7444 | 0·735113 ± 14 | 0·733597 | 413·4 | 0·1454 | 0·511716 ± 8 | 0·511695 | –17·8 |
| 1 | SQH-15 | Shiquanhe | 7·3703 | 0·736793 ± 15 | 0·734438 | 425·4 | 0·1514 | 0·511769 ± 6 | 0·511747 | –16·8 |
| 3 | 16YS | Bongba | 5·7284 | 0·725416 ± 13 | 0·723431 | 269·1 | 0·1389 | 0·511880 ± 7 | 0·511858 | –14·6 |
| 3 | 20YS | Bongba | 9·5209 | 0·734271 ± 12 | 0·730972 | 376·2 | 0·1426 | 0·511703 ± 7 | 0·511680 | –18·1 |
| 3 | 23YS | Bongba | 7·0429 | 0·731082 ± 10 | 0·728641 | 343·1 | 0·1346 | 0·511739 ± 9 | 0·511718 | –17·3 |
| 3 | 25YS | Bongba | 3·9564 | 0·728623 ± 11 | 0·727252 | 323·4 | 0·1230 | 0·511834 ± 8 | 0·511814 | –15·5 |
| 3 | JS07 | Bongba | 4·5272 | 0·737944 ± 18 | 0·736375 | 452·9 | 0·1392 | 0·511718 ± 6 | 0·511696 | –17·8 |
| 4 | 99-B06 | Xungba | 3·2795 | 0·726018 ± 15 | 0·724965 | 290·9 | 0·1393 | 0·511945 ± 7 | 0·511924 | –13·4 |
| 4 | 99-B09 | Xungba | 2·7297 | 0·721629 ± 14 | 0·720753 | 231·1 | 0·1420 | 0·511867 ± 7 | 0·511846 | –14·9 |
| 4 | 99-B23 | Xungba | 1·9282 | 0·718385 ± 17 | 0·717766 | 188·7 | 0·1441 | 0·511881 ± 8 | 0·511860 | –14·6 |
| 4 | 99-C12 | Xungba | 2·6537 | 0·719638 ± 16 | 0·718786 | 203·2 | 0·1407 | 0·511809 ± 9 | 0·511788 | –16·0 |
| 11 | 99-C15 | Sailipu | 3·1398 | 0·725834 ± 13 | 0·725077 | 292·4 | 0·1440 | 0·511833 ± 7 | 0·511817 | –15·6 |
| 11 | 99-C28 | Sailipu | 2·7726 | 0·726121 ± 13 | 0·725453 | 297·7 | 0·1601 | 0·511794 ± 9 | 0·511776 | –16·4 |
| 11 | XB-06 | Sailipu | 3·7600 | 0·729294 ± 12 | 0·728388 | 339·4 | 0·1587 | 0·511886 ± 8 | 0·511868 | –14·6 |
| 11 | XB-24 | Sailipu | 2·7114 | 0·724286 ± 15 | 0·723633 | 271·9 | 0·1613 | 0·511857 ± 5 | 0·511839 | –15·2 |
| 12 | BG015 | Zabuye | 1·0989 | 0·718163 ± 14 | 0·717913 | 190·7 | 0·1352 | 0·511816 ± 6 | 0·511802 | –15·9 |
| 12 | BG026 | Zabuye | 1·2704 | 0·715573 ± 14 | 0·715284 | 153·4 | 0·1284 | 0·511958 ± 10 | 0·511945 | –13·1 |
| 12 | BG037 | Zabuye | 0·9952 | 0·714098 ± 16 | 0·713872 | 133·3 | 0·1368 | 0·511857 ± 11 | 0·511843 | –15·1 |
| 12 | BG201 | Zabuye | 0·7695 | 0·712554 ± 13 | 0·712379 | 112·1 | 0·1297 | 0·511848 ± 9 | 0·511834 | –15·3 |
| 12 | BG203 | Zabuye | 1·0489 | 0·712828 ± 14 | 0·712589 | 115·1 | 0·1268 | 0·511932 ± 6 | 0·511919 | –13·6 |
| 13 | MG-008 | Maiga | 1·1260 | 0·721105 ± 17 | 0·720838 | 232·2 | 0·1313 | 0·511834 ± 6 | 0·511820 | –15·5 |
| 13 | MG-012 | Maiga | 1·4993 | 0·720519 ± 16 | 0·720163 | 222·6 | 0·1166 | 0·511821 ± 5 | 0·511808 | –15·8 |
| 13 | MG-015 | Maiga | 1·6402 | 0·724673 ± 18 | 0·724284 | 281·1 | 0·1160 | 0·511830 ± 8 | 0·511817 | –15·6 |
| 13 | MG-016 | Maiga | 1·9372 | 0·725438 ± 12 | 0·724979 | 291·0 | 0·1288 | 0·511782 ± 8 | 0·511768 | –16·6 |
| 16 | GZF3 | Garwa | 0·7429 | 0·715228 ± 11 | 0·715013 | 149·6 | 0·0824 | 0·511957 ± 7 | 0·511946 | –13·0 |
| 16 | GZF9 | Garwa | 0·6130 | 0·714435 ± 14 | 0·714258 | 138·9 | 0·1107 | 0·511974 ± 9 | 0·511959 | –12·7 |
| 17 | G-029 | Yaqian | 0·5222 | 0·718317 ± 15 | 0·718215 | 194·9 | 0·0868 | 0·511954 ± 6 | 0·511946 | –13·2 |
| 17 | GH03 | Yaqian | 0·7649 | 0·717498 ± 16 | 0·717349 | 182·6 | 0·1011 | 0·511919 ± 7 | 0·511910 | –13·9 |
| 19 | GH05 | Mibale | 1·2176 | 0·718412 ± 13 | 0·718148 | 194·0 | 0·1041 | 0·511971 ± 9 | 0·511961 | –12·8 |
| 19 | GH09 | Mibale | 2·3061 | 0·716591 ± 12 | 0·716090 | 164·8 | 0·0974 | 0·511994 ± 7 | 0·511984 | –12·4 |
| 21 | ZFC004 | Chazi | 2·1798 | 0·722832 ± 10 | 0·722476 | 255·4 | 0·1192 | 0·511914 ± 7 | 0·511905 | –14·0 |
| 21 | ZFC008 | Chazi | 1·6339 | 0·725266 ± 17 | 0·724999 | 291·2 | 0·1053 | 0·511867 ± 9 | 0·511859 | –14·9 |
| 21 | ZFC009 | Chazi | 1·4504 | 0·729849 ± 13 | 0·729612 | 356·7 | 0·1178 | 0·511808 ± 8 | 0·511799 | –16·1 |
| 22 | GB036 | Pabbai | 1·4569 | 0·713384 ± 14 | 0·713078 | 122·0 | 0·1126 | 0·511987 ± 8 | 0·511976 | –12·5 |

Field number refers to number of volcanic field in Fig. 1. Chondritic uniform reservoir (CHUR) at the present day [($^{87}$Rb/$^{86}$Sr)$_{CHUR}$ = 0·0847 (McCulloch & Black, 1984); ($^{87}$Sr/$^{86}$Sr)$_{CHUR}$ = 0·7045 (DePaolo, 1988); ($^{147}$Sm/$^{144}$Nd)$_{CHUR}$ = 0·1967 (Jacobsen & Wasserburg, 1980); ($^{143}$Nd/$^{144}$Nd)$_{CHUR}$ = 0·512638 (Goldstein *et al.*, 1984)] was used for the calculations. $\lambda_{Rb} = 1{\cdot}42 \times 10^{-11}$ a$^{-1}$ (Steiger & Jäger, 1977); $\lambda_{Sm} = 6{\cdot}54 \times 10^{-12}$ a$^{-1}$ (Lugmair & Marti, 1978). εSr(i) and εNd(i) were calculated using the average ages of the volcanic fields (Table 1).

anomalies (Fig. 8), consistent with a subduction-related origin. Relatively high contents of LILE and LREE (Figs 7 and 8) and high ($^{87}$Sr/$^{86}$Sr)$_i$ and low ($^{143}$Nd/$^{144}$Nd)$_i$ (Fig. 12) indicate that their parental magmas were derived from an enriched mantle source. Additionally, their Sr–Nd–Pb isotope compositions exhibit coherent trends between likely ambient asthenospheric mantle (MORB-source mantle) and Indian continental crust (Fig. 12), consistent with a subduction-related origin for the mantle source enrichment related to addition of subducted Indian continental crustally derived materials to their mantle source. The presence of a northward-subducted Indian continental lithosphere slab beneath the Lhasa terrane in south Tibet, identified in a number of geophysical studies (e.g. Li *et al.*, 2008; Nábělek *et al.*, 2009; Zhao *et al.*, 2010, 2011; Chen *et al.*, 2015), supports this inference. The decreases in Sr and Pb isotope initial ratios (Figs 11 and 12) in the ultrapotassic magmatic rocks from west to east may suggest decreasing involvement of the crustal component towards the east.

Nábělek *et al.* (2009) constructed a high-resolution, 800 km long, north–south cross-section of the lithosphere through the Lhasa terrane based on seismic data obtained as part of the Hi-CLIMB seismic experiment (Fig. 1). They identified a flat-lying, ~15 km thick layer above the seismic Moho, which they interpreted as subducted Indian lower continental crust. Such subducted Indian lower crust does not appear to extend further north than 31°N beneath Tibet. They suggested that this form of flat slab subduction must have developed in less than 20–25 Myr, based upon current rates of underthrusting of India beneath the Himalayas, and that before this Indian plate subduction was much steeper. Using the same seismic dataset Wittlinger *et al.* (2009) constrained the characteristics of this Indian

**Table 5**: Pb isotope compositions of the K-rich mafic magmatic rocks in south Tibet

| Field no. | Sample no. | Field name | $^{206}Pb/^{204}Pb$ | $^{207}Pb/^{204}Pb$ | $^{208}Pb/^{204}Pb$ | $^{238}U/^{204}Pb$ | $^{235}U/^{204}Pb$ | $^{232}Th/^{204}Pb$ | $(^{206}Pb/^{204}Pb)_i$ | $(^{207}Pb/^{204}Pb)_i$ | $(^{208}Pb/^{204}Pb)_i$ |
|---|---|---|---|---|---|---|---|---|---|---|---|
| 1 | GZ-S05 | Shiquanhe | 18·713 | 15·785 | 39·818 | 16·002 | 0·118 | 145·225 | 18·657 | 15·782 | 39·656 |
| 1 | GZ-S06 | Shiquanhe | 18·812 | 15·806 | 39·682 | 23·024 | 0·169 | 245·625 | 18·731 | 15·802 | 39·408 |
| 1 | GZ-S12 | Shiquanhe | 18·806 | 15·841 | 39·794 | 18·282 | 0·134 | 101·354 | 18·742 | 15·838 | 39·681 |
| 1 | GZ-S15 | Shiquanhe | 18·864 | 15·786 | 39·758 | 28·875 | 0·212 | 376·037 | 18·763 | 15·781 | 39·339 |
| 1 | GZ-S27 | Shiquanhe | 18·877 | 15·806 | 39·815 | 41·389 | 0·304 | 323·449 | 18·732 | 15·799 | 39·455 |
| 1 | SQH-08 | Shiquanhe | 19·005 | 15·796 | 39·801 | 24·723 | 0·182 | 281·129 | 18·919 | 15·792 | 39·488 |
| 1 | SQH-15 | Shiquanhe | 18·685 | 15·837 | 39·613 | 17·014 | 0·125 | 143·751 | 18·626 | 15·834 | 39·453 |
| 3 | 16YS | Bongba | 18·738 | 15·781 | 39·964 | 21·989 | 0·162 | 191·809 | 18·655 | 15·777 | 39·732 |
| 3 | 20YS | Bongba | 18·815 | 15·862 | 39·801 | 14·548 | 0·107 | 148·835 | 18·760 | 15·859 | 39·621 |
| 3 | 23YS | Bongba | 18·839 | 15·824 | 39·742 | 14·360 | 0·105 | 116·839 | 18·785 | 15·821 | 39·601 |
| 3 | 25YS | Bongba | 18·652 | 15·836 | 39·829 | 25·735 | 0·189 | 188·222 | 18·554 | 15·831 | 39·602 |
| 3 | JS07 | Bongba | 18·835 | 15·877 | 39·918 | 15·433 | 0·113 | 129·875 | 18·776 | 15·874 | 39·761 |
| 4 | 99-B06 | Xungba | 18·609 | 15·696 | 39·453 | 17·707 | 0·130 | 119·265 | 18·547 | 15·693 | 39·320 |
| 4 | 99-B09 | Xungba | 18·449 | 15·718 | 39·751 | 14·106 | 0·104 | 126·703 | 18·399 | 15·716 | 39·609 |
| 4 | 99-B23 | Xungba | 18·584 | 15·765 | 39·643 | 18·678 | 0·137 | 151·849 | 18·518 | 15·762 | 39·473 |
| 4 | 99-C12 | Xungba | 18·473 | 15·748 | 39·477 | 13·266 | 0·097 | 125·662 | 18·426 | 15·746 | 39·336 |
| 11 | 99-C15 | Sailipu | 18·721 | 15·751 | 39·772 | 31·470 | 0·231 | 190·487 | 18·638 | 15·747 | 39·612 |
| 11 | 99-C28 | Sailipu | 18·718 | 15·743 | 39·853 | 27·384 | 0·201 | 191·457 | 18·646 | 15·740 | 39·692 |
| 11 | XB-06 | Sailipu | 18·705 | 15·732 | 39·819 | 32·878 | 0·242 | 240·678 | 18·618 | 15·728 | 39·617 |
| 11 | XB-24 | Sailipu | 18·697 | 15·744 | 39·808 | 31·951 | 0·235 | 231·436 | 18·613 | 15·740 | 39·614 |
| 12 | BG015 | Zabuye | 18·502 | 15·679 | 39·316 | 9·669 | 0·071 | 70·423 | 18·478 | 15·678 | 39·260 |
| 12 | BG026 | Zabuye | 18·453 | 15·683 | 39·395 | 4·990 | 0·037 | 73·259 | 18·441 | 15·682 | 39·337 |
| 12 | BG037 | Zabuye | 18·474 | 15·725 | 39·518 | 9·539 | 0·070 | 66·240 | 18·450 | 15·724 | 39·465 |
| 12 | BG201 | Zabuye | 18·583 | 15·681 | 39·436 | 12·341 | 0·091 | 61·381 | 18·552 | 15·680 | 39·387 |
| 12 | BG203 | Zabuye | 18·457 | 15·729 | 39·403 | 7·709 | 0·057 | 83·126 | 18·438 | 15·728 | 39·337 |
| 13 | MG-008 | Maiga | 18·401 | 15·653 | 39·426 | 13·442 | 0·099 | 60·385 | 18·366 | 15·651 | 39·376 |
| 13 | MG-012 | Maiga | 18·419 | 15·706 | 39·561 | 20·513 | 0·151 | 152·739 | 18·366 | 15·704 | 39·435 |
| 13 | MG-015 | Maiga | 18·568 | 15·727 | 39·493 | 18·342 | 0·135 | 157·566 | 18·520 | 15·725 | 39·363 |
| 13 | MG-016 | Maiga | 18·528 | 15·686 | 39·325 | 19·058 | 0·140 | 139·246 | 18·479 | 15·684 | 39·210 |
| 16 | GZF3 | Garwa | 18·374 | 15·672 | 39·113 | 10·866 | 0·080 | 95·376 | 18·340 | 15·670 | 39·017 |
| 16 | GZF9 | Garwa | 18·326 | 15·681 | 39·105 | 11·101 | 0·082 | 87·172 | 18·291 | 15·679 | 39·017 |
| 17 | G-029 | Yaqian | 18·373 | 15·671 | 39·386 | 5·638 | 0·041 | 47·299 | 18·361 | 15·670 | 39·354 |
| 17 | GH03 | Yaqian | 18·352 | 15·746 | 39·402 | 5·406 | 0·040 | 39·171 | 18·340 | 15·745 | 39·375 |
| 19 | GH05 | Mibale | 18·533 | 15·745 | 39·514 | 12·018 | 0·088 | 92·859 | 18·504 | 15·744 | 39·444 |
| 19 | GH09 | Mibale | 18·427 | 15·752 | 39·484 | 12·109 | 0·089 | 47·536 | 18·398 | 15·751 | 39·448 |
| 21 | ZFC004 | Chazi | 18·659 | 15·762 | 39·273 | 16·354 | 0·120 | 61·705 | 18·630 | 15·761 | 39·238 |
| 21 | ZFC008 | Chazi | 18·706 | 15·783 | 39·391 | 12·202 | 0·090 | 63·358 | 18·684 | 15·782 | 39·355 |
| 21 | ZFC009 | Chazi | 18·543 | 15·826 | 39·285 | 14·956 | 0·110 | 90·573 | 18·516 | 15·825 | 39·233 |
| 22 | GB036 | Pabbai | 18·739 | 15·726 | 39·194 | 14·924 | 0·110 | 82·407 | 18·705 | 15·724 | 39·134 |

Field number refers to number of volcanic field in Fig. 1. $\lambda_{U238} = 0{\cdot}155125 \times 10^{-9}$ a$^{-1}$, $\lambda_{U235} = 0{\cdot}98485 \times 10^{-9}$ a$^{-1}$ and $\lambda_{Th232} = 0{\cdot}049475 \times 10^{-9}$ a$^{-1}$ (Steiger & Jäger, 1977). $(^{207}Pb/^{204}Pb)_{NHRL} = 0{\cdot}1084 \times (^{206}Pb/^{204}Pb)_i + 13{\cdot}491$ (Hart, 1984); $(^{208}Pb/^{204}Pb)_{NHRL} = 1{\cdot}209 \times (^{206}Pb/^{204}Pb)_i + 15{\cdot}627$ (Hart, 1984). Initial Pb isotope ratios were calculated using the average ages of the volcanic fields (Table 1).

lower crustal layer (thickness 19·3 ± 2·4 km, $V_s$ 4·73 ± 0·27 km s$^{-1}$, $\kappa$ 1·69 ± 0·06), which they attributed to eclogite-facies rocks. Schulte-Pelkum *et al.* (2005) demonstrated fast P-wave velocities of >7 km s$^{-1}$ in the lower crust of this region, which they attributed to partial eclogitization (~30%). Wittlinger *et al.* (2009) located the base of this high-grade metamorphic layer at ~80 km depth and showed that it extends up to 150 km north of the ITS (~31°N) and more than 1000 km laterally beneath the Lhasa terrane.

The seismic cross-section of Nábělek *et al.* (2009) may provide one of the best images we have of the present configuration of subduction beneath the Lhasa terrane. The geophysical recognition of an eclogite-facies crustal layer within the subducted Indian continental slab provides further support for our contention that the enrichment of the source of the ultrapotassic magmas originated from mixing between subducted Indian continental crustal materials and mantle wedge peridotite. The spatial distribution of the eclogite-facies lower crustal layer overlaps with that of the post-collisional potassic and ultrapotassic magmatic rocks in the Lhasa terrane (Fig. 1).

Rogers *et al.* (1985) proposed that abundances of the first row transition elements in post-collisional mafic ultrapotassic and potassic magmas are not affected by metasomatic enrichment of their mantle source region and may thus reflect the original protolith. Consequently, we use these transition elements to constrain the compositional characteristics of the mantle source region of the Tibetan ultrapotassic mafic magmas prior to its subsequent enrichment. Chondrite-normalized patterns of the first row transition elements (Fig. 16) are comparable with those of MORB, suggesting a DMM-like mantle protolith prior to its continental subduction-related enrichment. Moreover, the composition of the mantle source region of the ultrapotassic mafic magmas prior to this enrichment appears to be

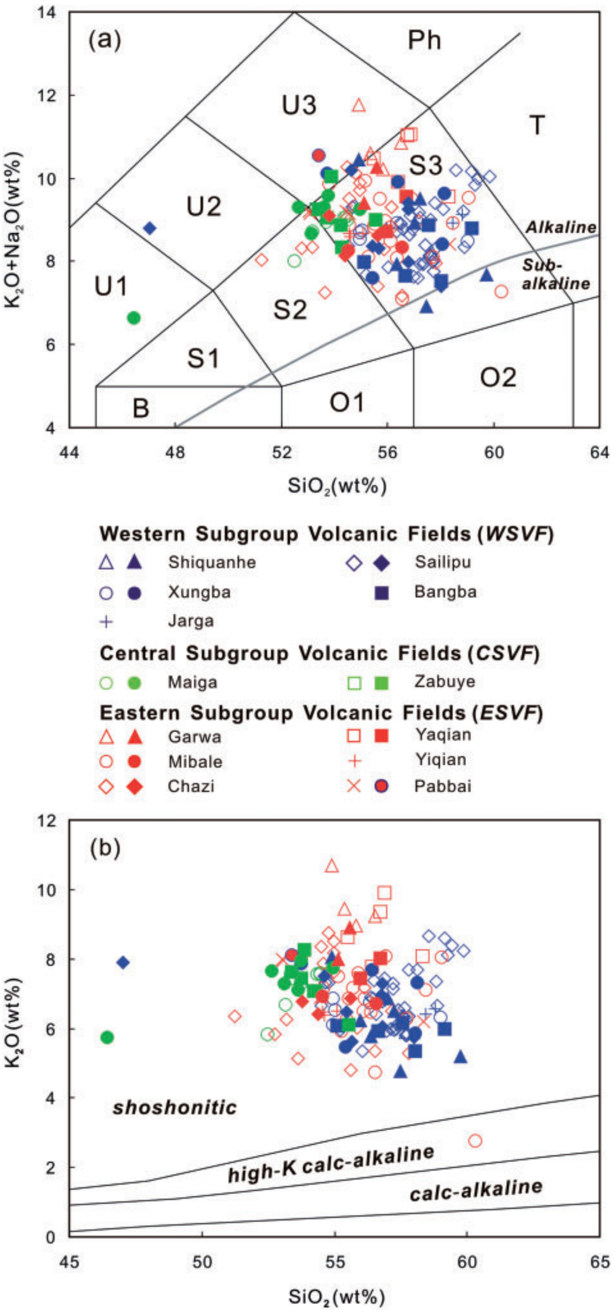

**Fig. 4**. (a) $K_2O + Na_2O$ (wt %) vs $SiO_2$ (wt %) for the post-collisional ultrapotassic mafic igneous rocks of the Lhasa terrane. All data plotted have been recalculated to 100 wt % on a volatile-free basis (Table 3). Classification boundaries are from Le Bas *et al.* (1986) and Le Maitre *et al.* (1989). Filled and open symbols represent, respectively, data from this study and the published data of Miller *et al.* (1999), Williams *et al.* (2001, 2004), Ding *et al.* (2003, 2006), Jiang (2003), Gao *et al.* (2007), Sun *et al.* (2007), Wang *et al.* (2008), Zhao *et al.* (2009*a*), Chen *et al.* (2012), Tian *et al.* (2012) and Guo *et al.* (2013). Classification fields shown by letters are as follows: B, basalt; Ph, phonolite; T, trachyte; O1, basaltic andesite; O2; andesite; S1, trachybasalt; S2, basaltic trachyandesite; S3, trachyandesite; U1, tephrite; U2, phonotephrite; U3, tephriphonolite. (b) $K_2O$ (wt %) vs $SiO_2$ (wt %) diagram for the same samples as plotted in (a). The dividing lines show the classification boundaries from Peccerillo & Taylor (1976) and Rickwood (1989). Data sources and symbols are as in (a).

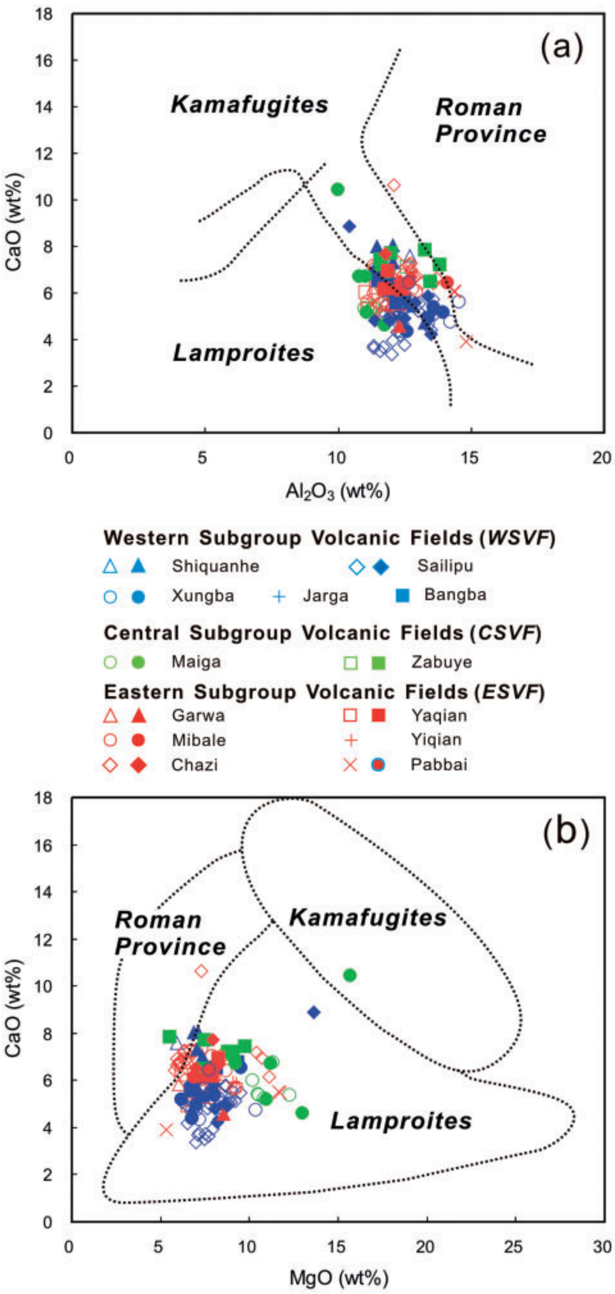

**Fig. 5**. (a) CaO (wt %) vs $Al_2O_3$ (wt %); (b) CaO (wt %) vs MgO (wt %) for the Lhasa terrane ultrapotassic magmatic rocks. Classification boundaries are from Foley *et al.* (1987). Data have been normalized to 100 wt % volatile-free as indicated in Table 3. Data sources are as in Fig. 4.

constant (i.e. MORB-source mantle, DMM) from west to east in south Tibet. This confirms that the decreases in Sr and Pb isotope initial ratios and trace-element ratios (Figs 11 and 12) of the magmas from west to east must result from a decreasing crustal component in the mantle source region of the magmas towards the east.

To constrain the composition of the crustal component in the mantle source region of the post-collisional mafic K-rich magmas we corrected the major element compositions of the most primitive mafic magmatic rocks to Mg-number [$100Mg/(Mg + Fe^{2+})$] = 72 for those

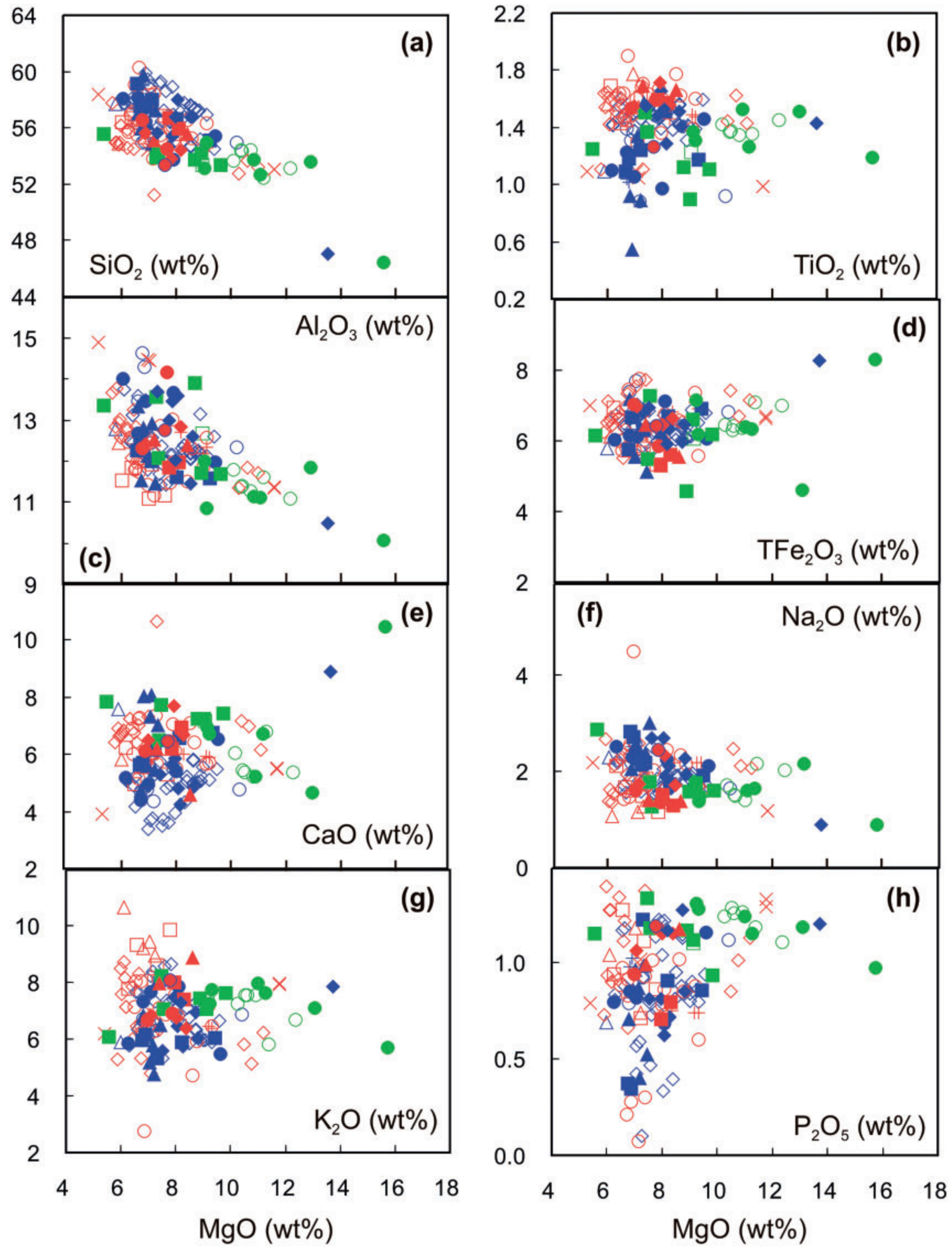

**Fig. 6.** Selected major elements vs MgO (wt %) indicating the compositional range of the post-collisional ultrapotassic igneous rocks in south Tibet. (a) SiO$_2$; (b) TiO$_2$; (c) Al$_2$O$_3$; (d) TFe$_2$O$_3$; (e) CaO; (f) Na$_2$O; (g) K$_2$O; (h) P$_2$O$_5$. Data have been normalized to 100 wt % volatile-free as indicated in Table 3. Data sources and symbols are as in Fig. 4. TFe$_2$O$_3$, all Fe is reported as Fe$_2$O$_3$.

samples with Mg-numbers less than 72, using an olivine–melt $K_D$ of 0·30 (see Roeder & Emslie, 1970), based on the approach of Niu *et al.* (1999) and Humphreys & Niu (2009). The compositional correction allows comparison of the major element compositions normalized to the same Mg-number (= 72) for the different volcanic fields in south Tibet, thus compensating for any effects of olivine fractionation and/or accumulation on the whole-rock composition of the magmatic rocks. Compared with MORB the K-rich magmatic rocks in south Tibet are characterized by higher SiO$_2$ and Ni contents, higher Sr and Pb isotope ratios, and lower CaO and MgO contents and Nd isotope ratios (Fig. 17). The correlations between Sr–Nd–Pb isotope and major

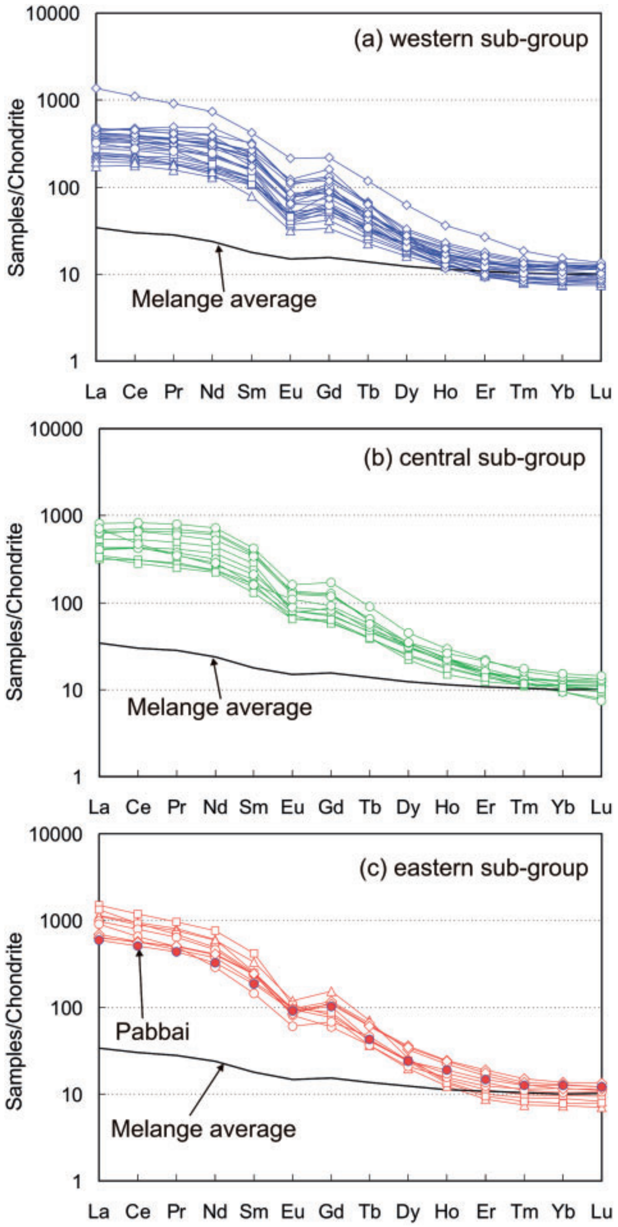

**Fig. 7.** Chondrite-normalized rare earth element (REE) patterns for the western (a), central (b) and eastern (c) subgroup volcanic fields of the Lhasa terrane in south Tibet; normalization factors are from Sun & McDonough (1989). The mélange average composition is from Marschall & Schumacher (2012). Data sources are as in Fig. 4.

element compositions indicate the presence of a component in the mantle source of the K-rich magmas that is enriched in $SiO_2$, $Al_2O_3$, Ni and $^{87}Sr/^{86}Sr$, and depleted in CaO, MnO and MgO. This component is consistent with the composition of a partial melt of eclogite-facies continental crust, generated from the crustal layer at the top of the subducted Indian continental lithosphere. This melt would have infiltrated the overlying mantle wedge causing metasomatic enrichment. This inference is consistent with seismological observations of the presence of eclogite-facies crustal materials on the top of the subducted Indian continental lithospheric slab beneath south Tibet (e.g. Nábělek *et al.*, 2009; Chen *et al.*, 2015).

### *A pyroxenite source for the magmas*

A number of recent studies (Sobolev *et al.*, 2005, 2007; Herzberg, 2011; Prelević *et al.*, 2013) have suggested that partial melts of subducted eclogite-facies crustal rocks may react with surrounding mantle peridotite to yield pyroxenite via reaction of olivine to form pyroxene. Partial melts derived from subsequent melting of such pyroxenites are characterized by higher Ni and $SiO_2$, and lower MgO contents, compared with melts of upper mantle peridotite (Sobolev *et al.*, 2005, 2007; Straub *et al.*, 2008; Herzberg, 2011). The compositional characteristics (e.g. high $SiO_2$ and Ni concentrations and relatively low MgO and CaO contents) of the mafic K-rich magmas in south Tibet are consistent with those of partial melts produced by pyroxenite melting (Fig. 18).

Olivine phenocrysts crystallized from partial melts of such mantle pyroxenites have lower Ca, Mn and Mg concentrations compared with those crystallized from melts of upper-mantle peridotite (Sobolev *et al.*, 2005, 2007; Herzberg, 2011). The olivine phenocrysts in the mafic K-rich magmas in south Tibet display similar compositional characteristics to those crystallized from partial melts of pyroxenite (Fig. 19).

Two types of pyroxenite can be recognized in the mantle source of the mafic K-rich magmas of the Lhasa terrane based upon the compositional characteristics of their olivine phenocrysts: (1) olivine-free pyroxenite (shown by the black–blue–green symbols in Fig. 19); (2) olivine-bearing pyroxenite (shown by the red symbols in Fig. 19). Olivine phenocrysts crystallized from partial melts of olivine-free pyroxenite are lower in Mg and Ca, higher in Mn, and lower in Fe/Mn compared with those crystallized from partial melts of olivine-bearing pyroxenite. The host melts produced from the olivine-bearing pyroxenite are higher in MgO (14–15·8 wt %) and lower in $SiO_2$ (46–47 wt %) (e.g. samples MG1303 and SLP1314 in Table 3) compared with those derived from the olivine-free pyroxenite (Fig. 18). However, partial melts derived from these two types of pyroxenite appear to show semi-continuous compositional variation trends (Fig. 18). The formation of the olivine-free pyroxenite in the mantle source region requires a higher proportion of partial melt from subducted Indian eclogite-facies crust reacting with a peridotite protolith compared with the olivine-bearing pyroxenite.

Recent studies (e.g. Sobolev *et al.*, 2005, 2007; Straub *et al.*, 2008; Prelević *et al.*, 2013) indicate that abundances of Ni in upper mantle peridotite-derived primary magmas are mainly governed by olivine, because this mineral has the highest solid–melt partition coefficient for Ni (e.g. $K_d{}^{olivine}{}_{Ni} = 10$; Straub *et al.*, 2008). The extremely high Ni concentrations in the olivine phenocrysts of the mafic K-rich magmas in south Tibet may be interpreted in terms of replacement of

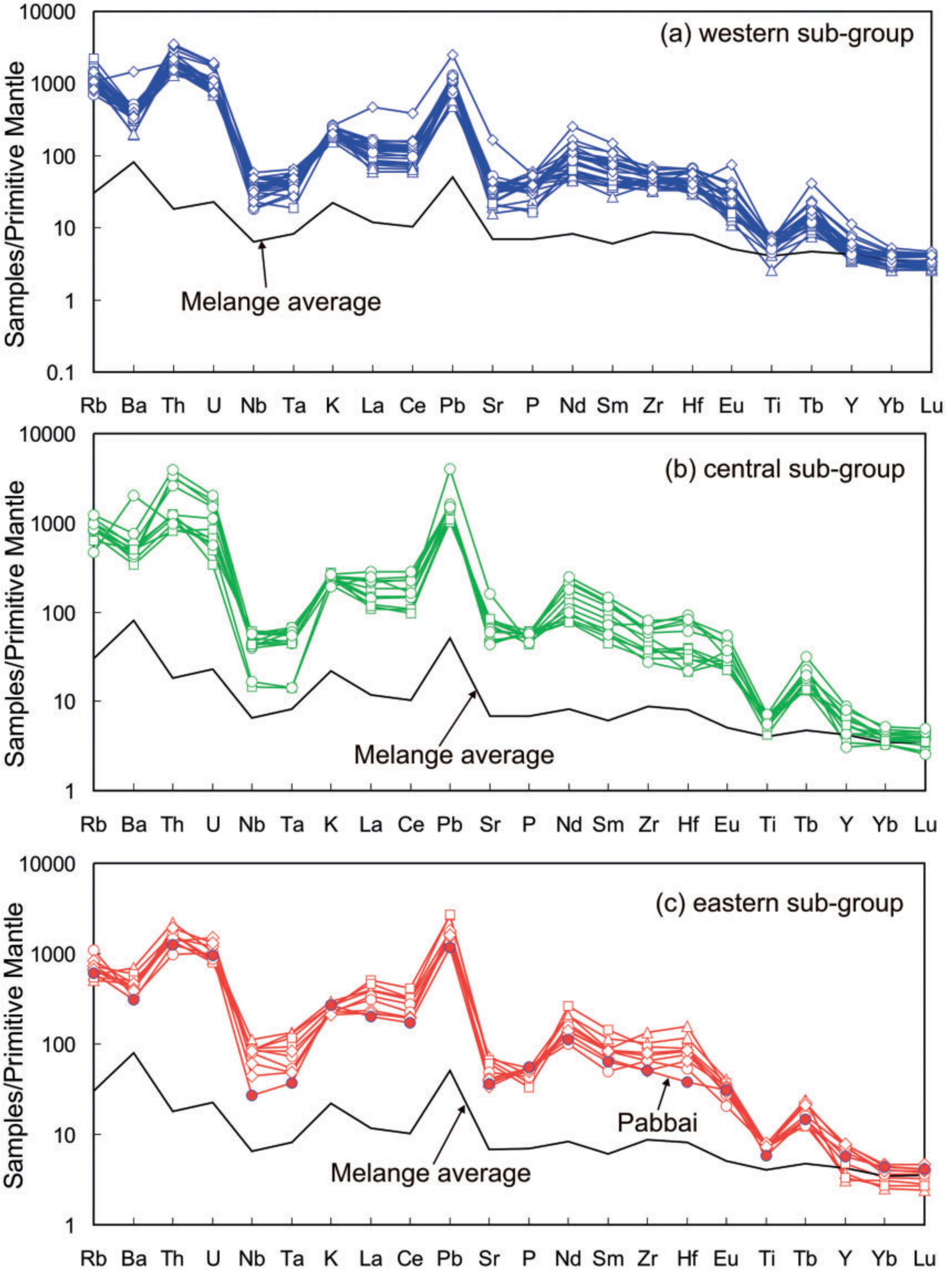

**Fig. 8.** Primitive mantle-normalized trace element patterns for the western (a), central (b) and eastern (c) subgroup volcanic fields of the Lhasa terrane in south Tibet; normalization factors are from Sun & McDonough (1989). The mélange average composition is from Marschall & Schumacher (2012). Data sources are as in Fig. 4.

olivine in their mantle source by orthopyroxene through reaction with partial melts of subducted Indian crustal materials. The Ni previously preserved in the olivine of the peridotite protolith must now be contained in orthopyroxene. The orthopyroxene in the reaction-formed pyroxenite has a lower solid–melt partition coefficient for Ni (e.g. $K_{\mathrm{d}}{}^{\mathrm{orthopyroxene}}{}_{\mathrm{Ni}} = 2$; Straub *et al.*, 2008; Prelević *et al.*, 2013) compared with the original olivine in the peridotite, suggesting that the pyroxenite-derived primary magmas would have about five times the Ni concentration compared with melts derived from peridotite. Olivine phenocrysts crystallized from such

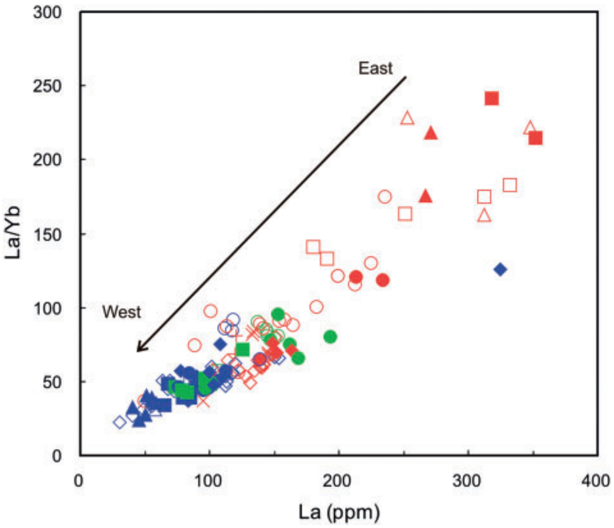

**Fig. 9.** La/Yb vs La (ppm) for the Lhasa terrane ultrapotassic magmatic rocks. Data sources and symbols are as in Fig. 4.

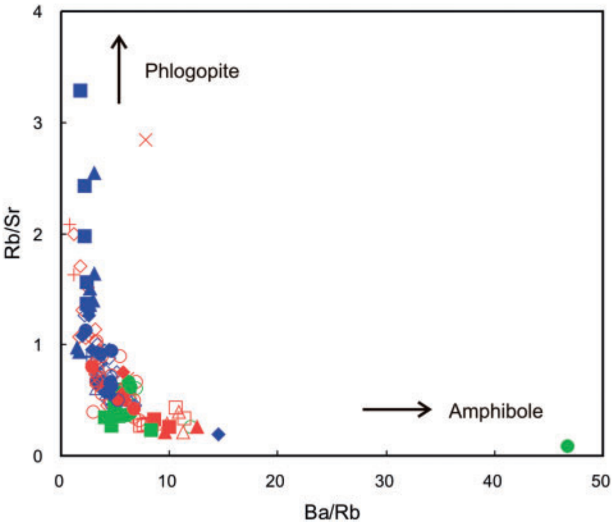

**Fig. 10.** Rb/Sr vs Ba/Rb for the Lhasa terrane ultrapotassic magmatic rocks. Amphibole and phlogopite on the arrows refer to these phases as residual phases in the mantle source region of the magmas. Data sources and symbols are as in Fig. 4.

Ni-rich primary magmas would have also high Ni concentrations.

The olivine–melt partition coefficients for Ni ($K_d{}^{olivine}{}_{Ni}$) in low-MgO and high-$SiO_2$ magmas are significantly higher than those in melts with MgO >10 wt % (e.g. Kinzler *et al.*, 1990; Beattie *et al.*, 1991; Straub *et al.*, 2008). Because magmas derived from pyroxenite melting are lower in MgO and higher in $SiO_2$ than those formed from peridotite melting (Fig. 18), the olivine–melt partition coefficient for Ni ($K_d{}^{olivine}{}_{Ni}$) during pyroxenite melting will be significantly higher (up to 35; Beattie *et al.*, 1991; Straub *et al.*, 2008). Consequently, olivine phenocrysts crystallized from the Ni-rich, $SiO_2$-rich and MgO-poor magmas resulting from pyroxenite melting should have extremely high Ni contents.

The compositions of the olivine phenocrysts in the Lhasa terrane ultrapotassic magmatic rocks appear to define three distinct curved trends (B1, B2 and B3) in a plot of Ni content in olivine versus Fo (mol %) (Fig. 20), shown by the black, blue and red symbols, respectively. They display concave-down trends. Previous studies (e.g. Straub *et al.*, 2008; Prelević *et al.*, 2013) have indicated that such concave-down trends may be explained by fractional crystallization of olivine from pyroxenite-derived parent magmas. Modelled variations in olivine composition induced by fractional crystallization of the host melt (see Supplementary Data Appendix B for more details of the modeling calculation) fit the B1, B2 and B3 trends of the olivine phenocrysts very well (Fig. 20). The different compositions of the parent magmas of each trend are interpreted to reflect varying proportions of eclogite partial melt involved in the formation of their pyroxenite sources. The B1 and B2 magma sources are olivine-poor to olivine-free pyroxenites whereas the B3 source is an olivine-rich pyroxenite. The proportion of the eclogite melt component in the pyroxenite source increases from B3 to B1 (shown by the blue arrow in Fig. 20).

The transition element Ni is enriched in the upper mantle, whereas it is strongly depleted in the continental and oceanic crust (e.g. Rudnick & Gao, 2003). Moreover, Ni is neither fluid-mobile, nor mobile in low-MgO melts of continental crust (e.g. Straub *et al.*, 2008). Thus, siliceous melts from subducted Indian eclogite-facies continental crust would have low Ni contents. Olivine phenocrysts defining the compositional trend B1 have lower Fo contents than the B2 and B3 trends, but similarly high Ni concentrations in the most forsteritic olivines (olivine composition field labeled ‘A’ in Fig. 20), which can reasonably be interpreted only in terms of a greater amount of melt derived from subducted Indian eclogite-facies continental crustal materials (as shown by the blue arrow in Fig. 20) in the generation of their pyroxenite source, compared with those of the B2 and B3 trends. We subsequently refer to their source as a $SiO_2$-rich pyroxenite.

The olivine phenocrysts that define the B3 trend are consistent with those crystallized from melts of olivine-bearing pyroxenite (Fig. 19). However, they could also reflect crystallization from mixtures of melts of olivine-free pyroxenite (‘R’ in Fig. 20) and melts of peridotite (‘P’ in Fig. 20). The corroded rims of the olivine phenocrysts (Fig. 3b) and reaction rims on xenocrystic olivine (Fig. 3a and c) are consistent with mixing of melts from such a hybridized peridotite–pyroxenite source. The hybrid melts have the highest MgO (14–15·8 wt %), moderate Ni (272–452 ppm) and relatively low $SiO_2$ contents (46–47 wt %) (e.g. samples MG1303 and SLP1314 in Table 3). These samples may indicate a more important contribution for peridotite in the mantle source.

The correlation between the Ni and Fo contents of olivine phenocrysts (Fig. 20) appears to be highly sensitive in distinguishing between different mantle source regions and their partial melts. Three distinct source

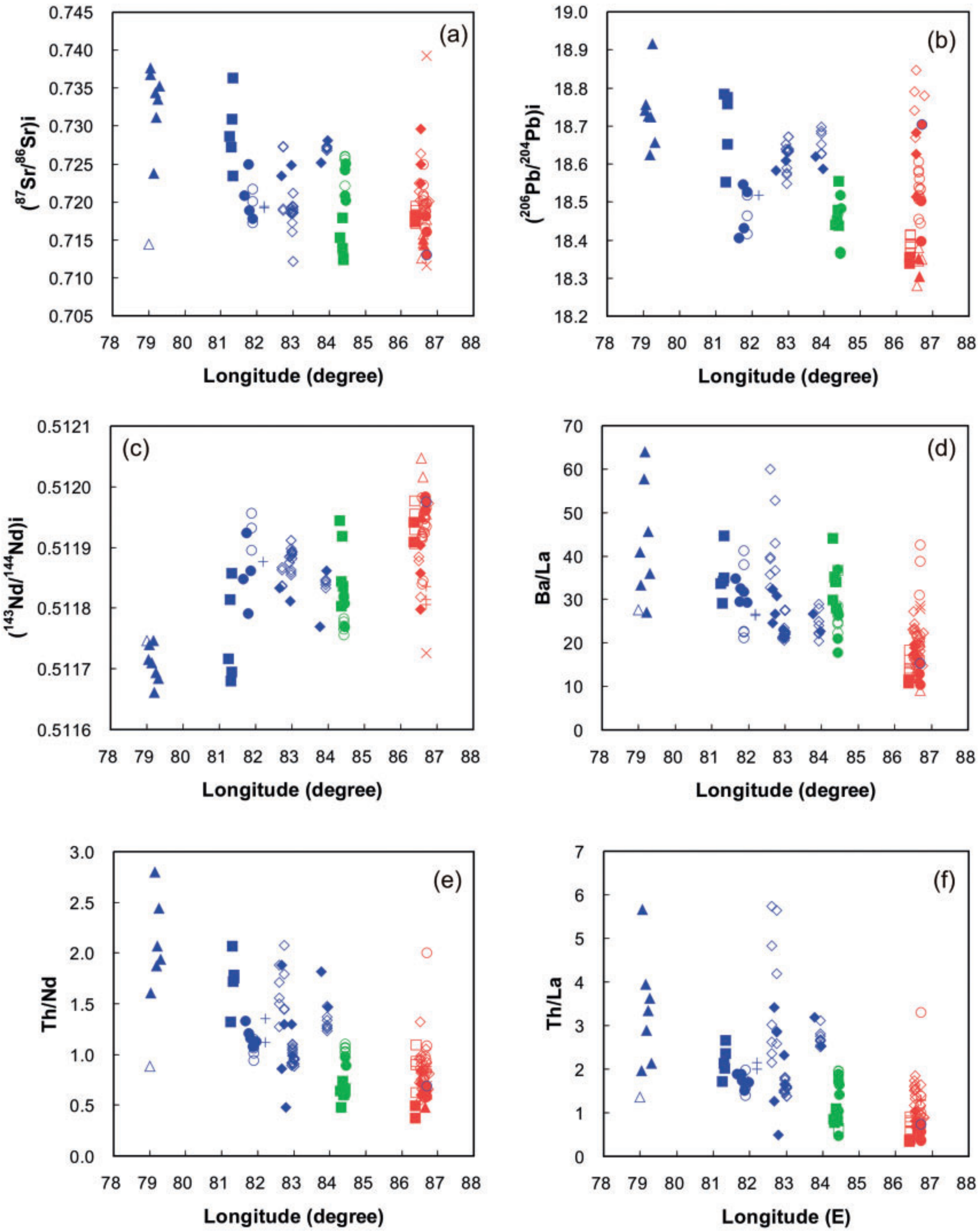

**Fig. 11.** Variation in Sr–Nd–Pb isotope and trace element ratios of the post-collisional ultrapotassic mafic magmatic rocks from west to east in the Lhasa terrane. Data are from Tables 3–5. Symbols are as in Fig. 4.

components are recognized from west to east in south Tibet: $SiO_2$-rich pyroxenite (compositional trend B1 in Fig. 20), olivine-free pyroxenite (compositional trend B2 in Fig. 20) and olivine-bearing pyroxenite (compositional trend B3 in Fig. 20). In detail, the mantle source region of the magmas in the western and central subgroups (Sailipu, Xungba, Zabuye and Maiga volcanic fields; Figs 1 and 20) contains all three types of pyroxenite, whereas that in the eastern subgroup (Mibale volcanic field; Figs 1 and 20) contains only olivine-bearing pyroxenite. In Fig. 21 we illustrate our understanding of the changing characteristics of the mantle source of the ultrapotassic magmas from west to east in the Lhasa terrane.

On the basis of the above discussion we propose that the mantle source region of the post-collisional mafic K-rich magmas in south Tibet has been metasomatized by partial melts of subducted Indian eclogite-facies continental crust that infiltrated the peridotite mantle wedge. These partial melts reacted to varying degrees with the

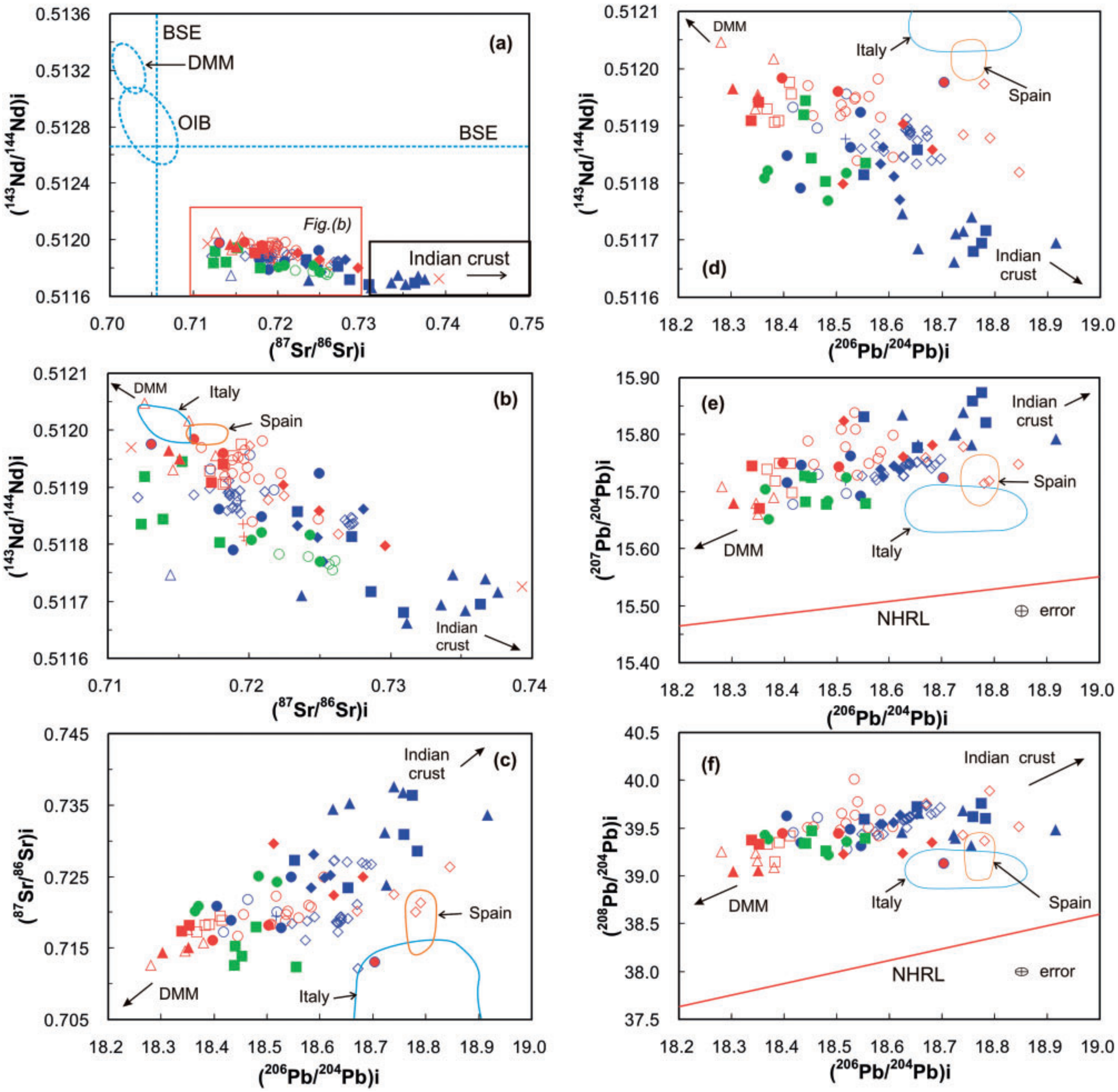

**Fig. 12.** (a) $(^{143}Nd/^{144}Nd)_i$ vs $(^{87}Sr/^{86}Sr)_i$ in the post-collisional ultrapotassic mafic magmatic rocks; (b) enlargement of the field of data in (a); (c) $(^{87}Sr/^{86}Sr)_i$ vs $(^{206}Pb/^{204}Pb)_i$; (d) $(^{143}Nd/^{144}Nd)_i$ vs $(^{206}Pb/^{204}Pb)_i$; (e) $(^{207}Pb/^{204}Pb)_i$ vs $(^{206}Pb/^{204}Pb)_i$; (f) $(^{208}Pb/^{204}Pb)_i$ vs $(^{206}Pb/^{204}Pb)_i$. Arrows (or outlined fields) indicate the composition of DMM (Workman & Hart, 2005) and Indian continental crust [see Inger & Harris (1993), Ahmad *et al.* (2000), Richards *et al.* (2005) and Guo & Wilson (2012) for more detailed discussion]. The Northern Hemisphere Reference Line (NHRL; Hart, 1984), and fields for OIB and Bulk Silicate Earth (BSE; Wilson, 1989; Hofmann, 1997) are shown for reference. Fields labeled Italy and Spain denote the compositions of Italian and Spanish lamproites, respectively, based on data from Gasperini *et al.* (2002), Perini *et al.* (2004), Owen (2008), Prelević *et al.* (2008), Boari *et al.* (2009) and Conticelli *et al.* (2009). Data are from Tables 4 and 5. Symbols are as in Fig. 4.

surrounding peridotite to yield olivine-bearing pyroxenite, olivine-free pyroxenite and $SiO_2$-rich pyroxenite, subsequent partial melting of which formed the most primitive K-rich mafic magmas in south Tibet (Figs 20 and 21). Partial melting of olivine-bearing pyroxenites resulted in more $SiO_2$-poor and higher MgO magmas in the eastern subgroup volcanic fields (Fig. 21). An increasing proportion of subducted Indian crust in the mantle source of the magmas westward resulted in more $SiO_2$-rich, K-rich magmas in the central–western subgroup volcanic fields (e.g. sample MG1301 in the Maiga volcanic field; Figs 20 and 21).

### *Trace element and Sr–Nd–Pb isotope indicators of the role of subducted continental crust*

Previous studies (e.g. Tommasini *et al.*, 2011; Prelević *et al.*, 2013) have suggested that Th (and Sm) enrichment in K-rich magmas may be attributed to the presence of continental crustal material in their mantle source. Zoisite–epidote and lawsonite in continentally

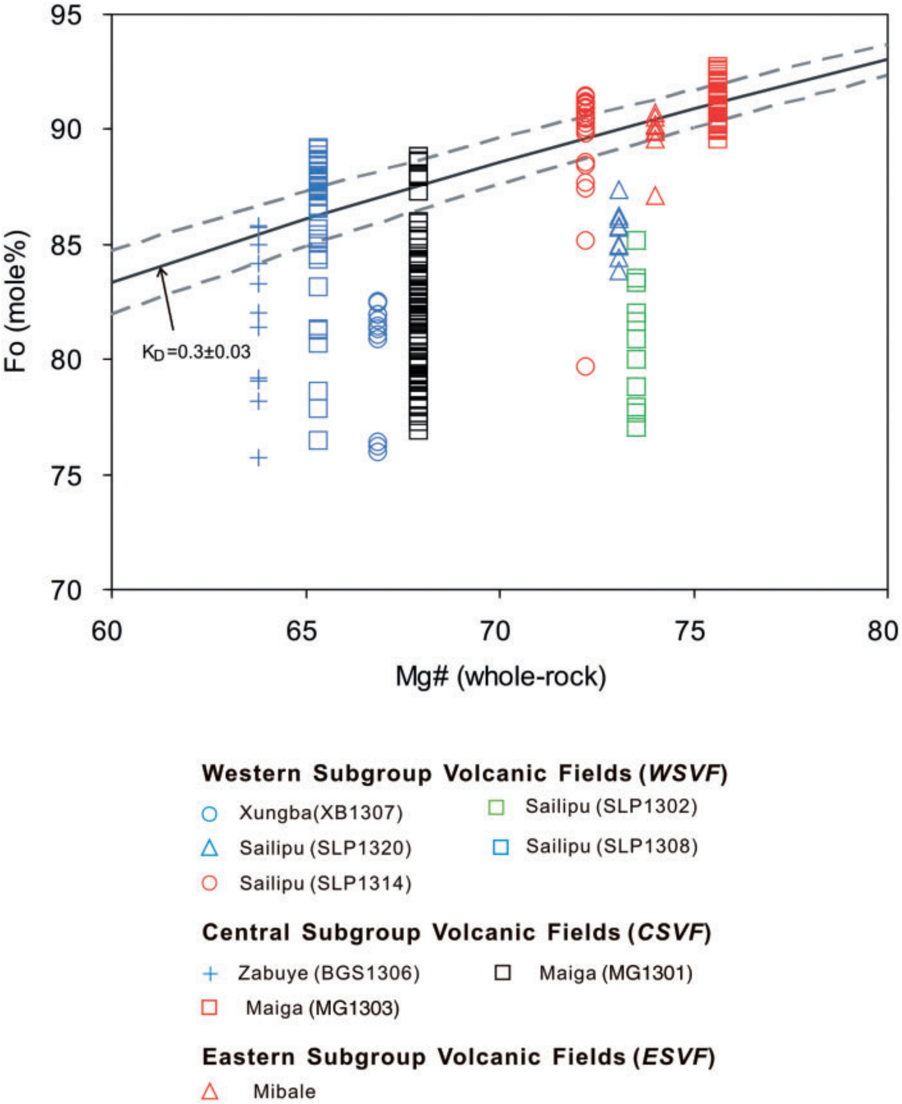

**Fig. 13.** Fo content (mol %) in olivine phenocrysts vs Mg# in the whole-rocks. Continuous and dashed curve lines show the Fe–Mg exchange equilibrium for $K_{D(Fe\text{–}Mg)} = 0{\cdot}3 \pm 0{\cdot}03$ between olivine and melt (Roeder & Emslie, 1970). The data for olivine phenocrysts in the Mibale volcanic rocks are from Yu *et al.* (2012). Because olivine phenocrysts from different samples in the same volcanic field were analysed, we use different symbols to distinguish them. Data are from Table 3 and Supplementary Data Appendix A.

derived metasedimentary materials (products of blueschist-facies metamorphism of subducted sediments) are likely repositories of Sr, Pb, U, Th and LREE (e.g. Brunsmann *et al.*, 2000; Spandler *et al.*, 2003; Frei *et al.*, 2004; Usui *et al.*, 2006; Feineman *et al.*, 2007; Tommasini *et al.*, 2011) based on their high partition coefficients for these elements. Partial melting of metasediments containing zoisite–epidote and lawsonite could thus lead to Th (and Sm) enrichment of the source of the K-rich magmas. The ultrapotassic mafic magmatic rocks of south Tibet exhibit such Th and Sm enrichments (Figs 8 and 22a).

Enrichment in LILE and the Sr–Nd–Pb isotope compositions of subduction-related magmas have been widely ascribed to the migration of fluids or melts from the subducted slab into their mantle source (e.g. Gill, 1981; Pearce, 1982; Hawkesworth *et al.*, 1997; Johnson & Plank, 1999). Geochemical distinctions have been recognized between subduction-related magmatic rocks whose mantle sources have been modified by fluids and those that have been enriched by slab-derived melts (e.g. Hawkesworth *et al.*, 1997; Johnson & Plank, 1999; Class *et al.*, 2000; Woodhead *et al.*, 2001; Guo *et al.*, 2014). Slab-derived fluids, which carry little REE and HFSE, can introduce significant amounts of LILE (e.g. K, Rb, Cs, Sr, Ba, U, Pb) from the subducting slab into the mantle source, whereas slab-derived melts are characterized by high Th and LREE contents.

We use the ratio of fluid-mobile Ba to fluid-immobile La to investigate the input of subduction-related fluids and Th/Nd to reflect the input of slab-derived melts because neither Ba/La nor Th/Nd is likely to be fractionated during partial melting of the mantle source. Within the Lhasa terrane the eastward decreases in Ba/La and Th/Nd in the post-collisional K-rich mafic magmatic rocks (Fig. 11d and e) could be explained by a

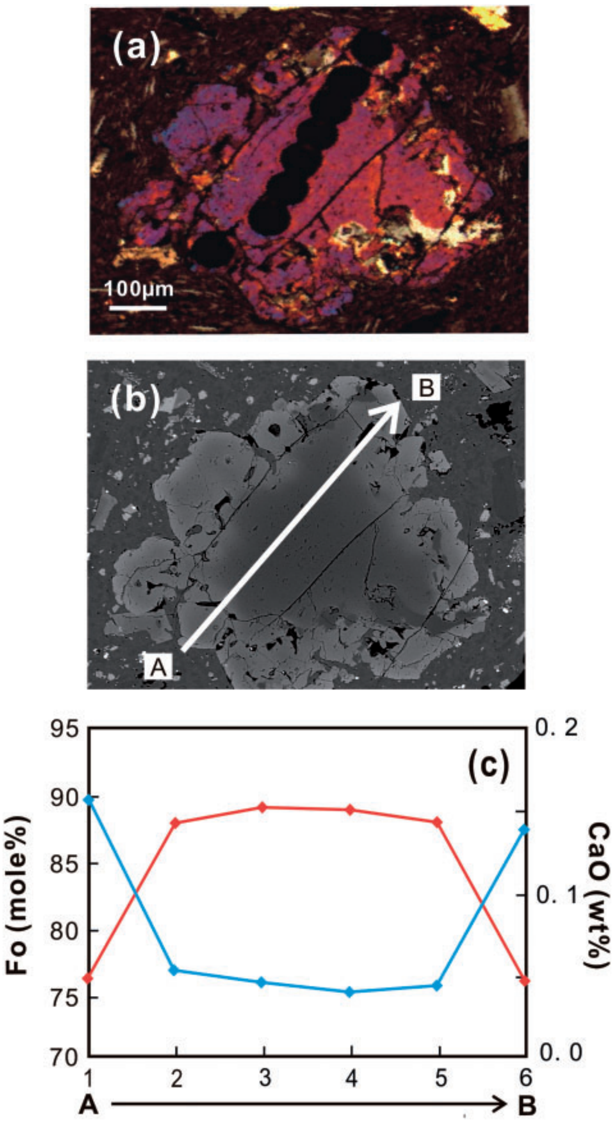

**Fig. 14.** Disequilibrium in a mantle olivine xenocryst. (a) Photomicrograph showing a disequilibrium texture between the olivine xenocryst and the surrounding melt (cross-polarized light; sample XB1307). Black circles indicate the locations of electron microprobe analyses. (b) Back-scattered electron image of the olivine xenocryst showing the location of the electron microprobe profile A–B. The xenocrystic core of the olivine is a darker grey. The lighter rim formed by reaction with the host melt. (c) Variation of Fo and CaO content along the profile A–B. The low CaO (less than 0·1 wt %; shown by the continuous blue line) content of the core of the olivine crystal, combined with its high Fo (>85%; shown by the continuous red line), is consistent with the core being xenocrystic (Prelević *et al.*, 2013). The rim of the olivine crystal is compositionally similar to the olivine phenocrysts in the sample.

decreasing flux of subducted Indian continental crust derived fluid and melt components into their mantle source region from west to east. This is consistent with the conclusions reached above based on the composition of olivine phenocrysts.

The ultrapotassic mafic magmatic rocks define a diffuse linear trend in a ($^{143}$Nd/$^{144}$Nd)$_i$ versus Th/La diagram (Fig. 22b), plotting between depleted MORB-source mantle (DMM) and an inferred Indian continental crustal sediment melt component with low ($^{143}$Nd/$^{144}$Nd)$_i$ and high Th/La, suggesting that their mantle source region comprises two end-members: (1) depleted MORB-source mantle (see Workman & Hart, 2005); (2) a melt derived from subducted Indian continental crust with ($^{143}$Nd/$^{144}$Nd)$_i < 0{\cdot}5117$ and high Th/La (>6). Because there is likely to be a wide variation of Th/La in the subducted Indian continental crustal component (Inger & Harris, 1993; Ahmad *et al.*, 2000; Richards *et al.*, 2005; Rehman *et al.*, 2008; Guo & Wilson, 2012), this can explain the dispersion in the data in Fig. 22b. Similarly, the ultrapotassic rocks display a negative correlation of ($^{143}$Nd/$^{144}$Nd)$_i$ versus Ba/La (Fig. 22c) plotting between a depleted MORB-source mantle (DMM) component and an Indian slab-derived fluid with low ($^{143}$Nd/$^{144}$Nd)$_i$ and high Ba/La. This suggests the presence of an Indian slab-derived fluid component in the mantle source region. The decreases in some trace element ratios (e.g. Th/La, Ba/La; Figs 11 and 22) and Sr–Pb initial isotope compositions (Fig. 11), together with increasing ($^{143}$Nd/$^{144}$Nd)$_i$, from west to east (Fig. 11), suggest an eastward decrease in the proportion of the Indian continental crustal components (including sediment melt and aqueous fluid) in the mantle source of the mafic K-rich magmas.

## *Dy/Dy* variations and Eu anomalies*

Davidson *et al.* (2013) have recently proposed the use of the parameter Dy/Dy* in the recognition of mantle source components and petrogenetic processes in the generation of subduction-related magmas. We have adapted their approach to show the role of subducted Indian continental crust in the petrogenesis of the post-collisional mafic ultrapotassic magmas in the Lhasa terrane (Fig. 22d). The relatively high Dy/Yb ratios of the magmatic rocks, combined with Dy/Dy* values less than 1·0, are distinct from those of MORB, ocean island basalt (OIB) and arc magmas. We interpret this distinctive signature to reflect the presence of an eclogite-facies crustal component derived from Indian continental lithosphere subduction in the mantle source of the ultrapotassic mafic magmas in south Tibet. The decreasing Dy/Dy* values of the magmas from west to east, combined with an increase in Dy/Yb ratios (Fig. 22d), may indicate a decrease in the degree of partial melting of the mantle source toward the east. The Dy/Yb ratios are higher in the western and central subgroup volcanic fields than in the eastern subgroup volcanic fields (Fig. 22d), suggesting that the proportion of the eclogite-facies crustal component derived from Indian continental crust subduction in the source of the magmas decreases from west to east.

The most primitive ultrapotassic rocks exhibit negative Eu anomalies in their chondrite-normalized REE patterns (Fig. 7). Although such negative Eu anomalies are typically attributed to plagioclase feldspar fractionation (or to the presence of residual plagioclase in the magma source) we consider that negative Eu anomalies

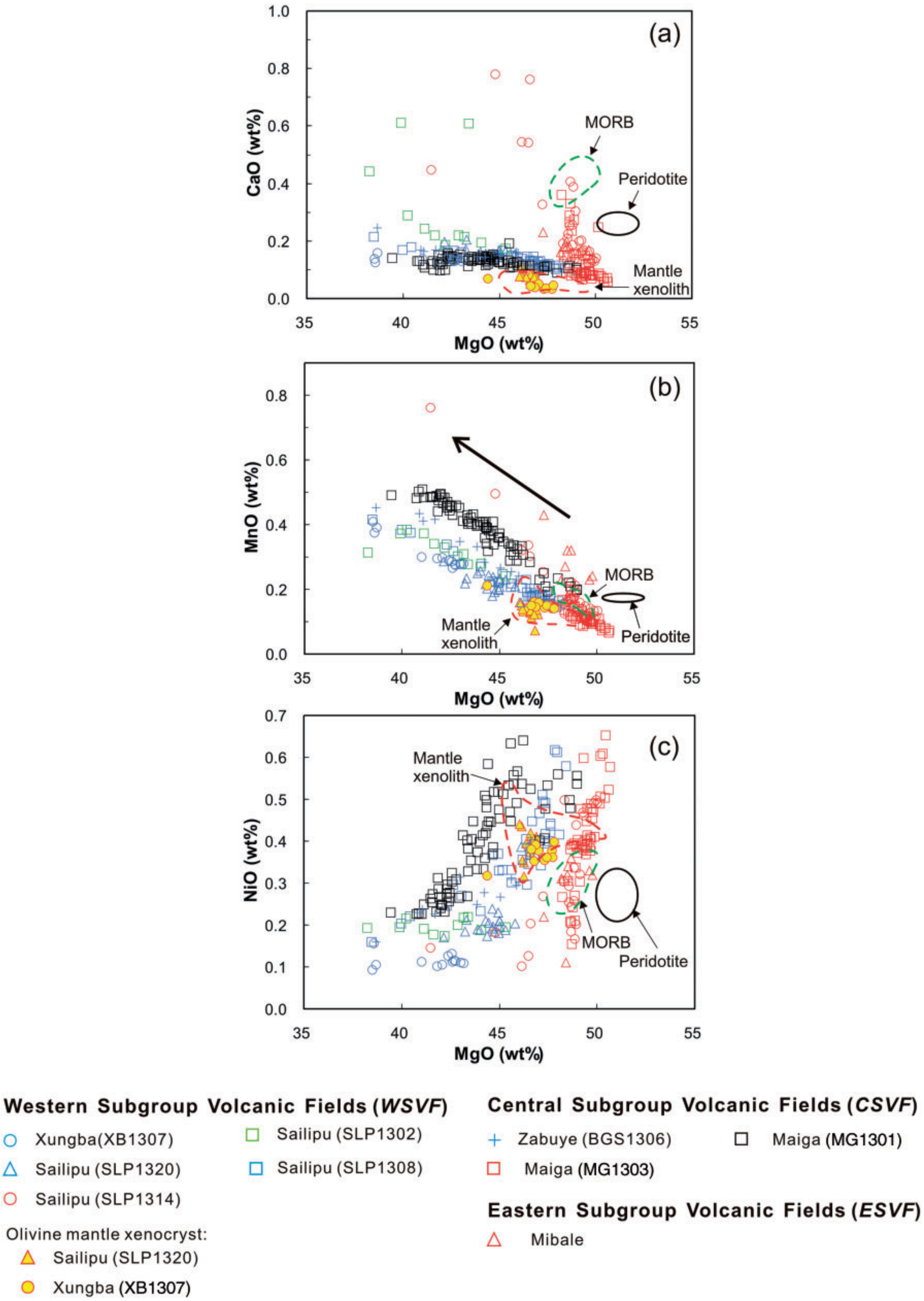

**Fig. 15.** Variation of CaO, MnO and NiO vs MgO (wt %) in olivine phenocrysts and xenocrysts. (a) CaO (wt %) vs MgO (wt %); (b) MnO (wt %) vs MgO (wt %); (c) NiO (wt %) vs MgO (wt %). The fields outlined by green dashed lines indicate the compositions of olivine phenocrysts in MORB (Sobolev *et al.*, 2007). The fields outlined by the black continuous lines denote the compositions of olivine phenocryst in partial melts of peridotite (Sobolev *et al.*, 2007). The fields outlined by red dashed lines indicate the compositions of olivine in mantle xenoliths from south Tibet (Liu *et al.*, 2011*a*). The arrow in (b) denotes olivine fractional crystallization (Sobolev *et al.*, 2007). Data are from Supplementary Data Appendix A.

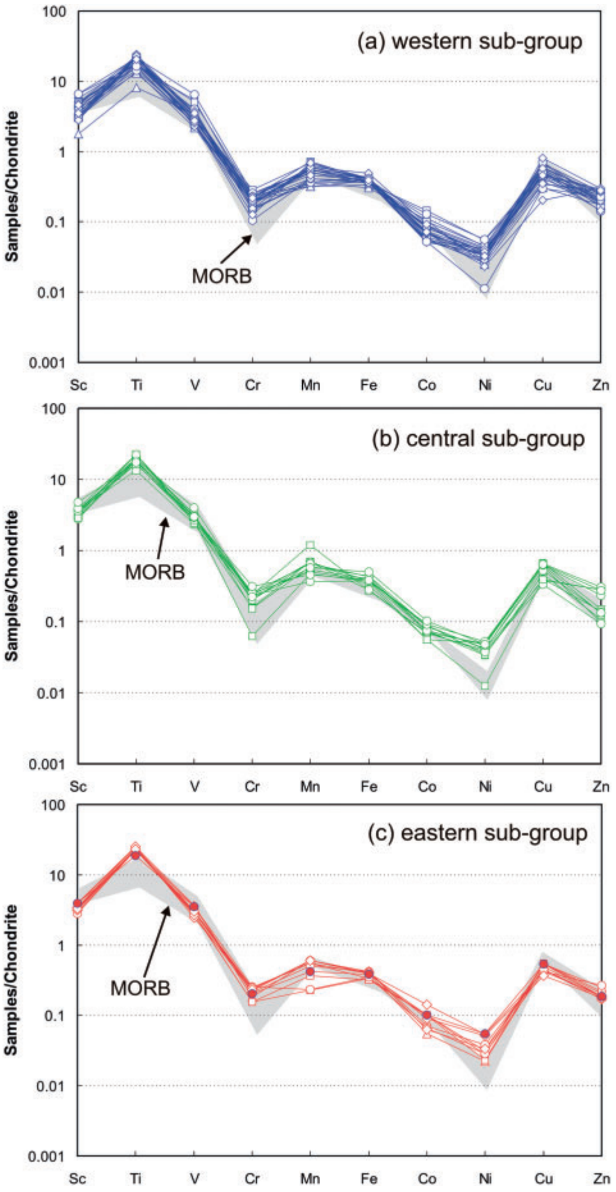

**Fig. 16.** Chondrite-normalized transition element variations in the western (a), central (b) and eastern (c) subgroup volcanic fields in south Tibet; normalization factors are from Langmuir *et al.* (1977). The grey fields indicate the composition of MORB (Rogers *et al.*, 1985; Hofmann, 1997; Workman & Hart, 2005; GERM website: http://www.earthref.org/). Data sources are as in Fig. 4.

in the Tibetan ultrapotassic magmatic rocks are an intrinsic feature inherited from their pyroxenite mantle source.

The diffuse negative correlation between $^{143}Nd/^{144}Nd$ and Dy/Dy* (Fig. 22e) may also indicate that the proportion of the eclogite-facies crustal component in the mantle source of the magmas decreases from west to east. The role of the Indian continental crustal component in the source of the magmas is also clearly demonstrated in a plot of Ce/Pb versus Nb/La (Fig. 22f).

## *Role of a subduction mélange*

Marschall & Schumacher (2012) have proposed a physical model by which components from a subducting slab and its overlying mantle wedge can be transported into the mantle source of subduction-related magmas. This involves formation of a mélange zone in a subduction channel on the top surface of the slab in which hydrated mantle rocks are mixed with material derived from the subducting slab, including trench sediments. The trace-element characteristics of exhumed metamorphic mélange rocks are similar to those of subduction-related magmas (Marschall & Schumacher, 2012), with distinctive enrichment in LILE and significant depletion in HFSE (e.g. Nb, Ta and Ti), indicating that subducted mélange rocks in the subduction channel could provide an important source component for arc magmas. Partial melting of well-mixed mélange rocks underplated below the base of the lithosphere via diapiric upwelling from the subduction channel is considered to generate subduction-related magmas in the Marschall & Schumacher (2012) model. Geophysical imaging of such underplated mélanges would clearly be extremely helpful in validating such a model. We propose that the eclogite-facies lower crustal layer on the top surface of the subducted Indian continental slab, recognized by seismic tomography (e.g. Nábělek *et al.*, 2009), might be the geophysical image of the final stage in the evolution of such a subduction channel beneath the Lhasa terrane, in which the mantle lithosphere of the Tibetan plate has effectively been removed by flat slab subduction. The seismic data clearly indicate the presence of eclogite–granulite-facies rocks in the crustal layer of the subducted Indian lithosphere. The subcontinental lithospheric mantle (SCLM) removed from the base of the Tibetan lithosphere during flat slab subduction probably represents the original mantle protolith involved in the petrogenesis of the ultrapotassic magmas. The similarity of this protolith to MORB-source mantle (Fig. 16) suggests that it may have been relatively recently accreted rather than ancient subcontinental lithospheric mantle. The termination of ultrapotassic magmatism at *c.* 8 Ma could reflect the timing of complete erosion of the Tibetan lithospheric mantle.

The primitive mantle-normalized incompatible trace element pattern of average subduction channel mélange rocks reported by Marschall & Schumacher (2012) is similar to those of the post-collisional ultrapotassic mafic magmas in south Tibet, characterized by enrichment in LILE and significant depletion in Nb, Ta and Ti (Fig. 8), although overall abundances are lower in the mélange rocks. In addition, the HREE abundances, together with some trace element ratios (e.g. Ce/Pb versus Nb/La; Fig. 22f), are similar between average subduction channel mélange rocks (Marschall & Schumacher, 2012) and the ultrapotassic magmas in south Tibet (Fig. 7).

## *Quantifying the proportion of the subducted Indian crustal component*

Based on our discussions of the mineral chemistry of olivine (Figs 15, 19 and 20) and whole-rock

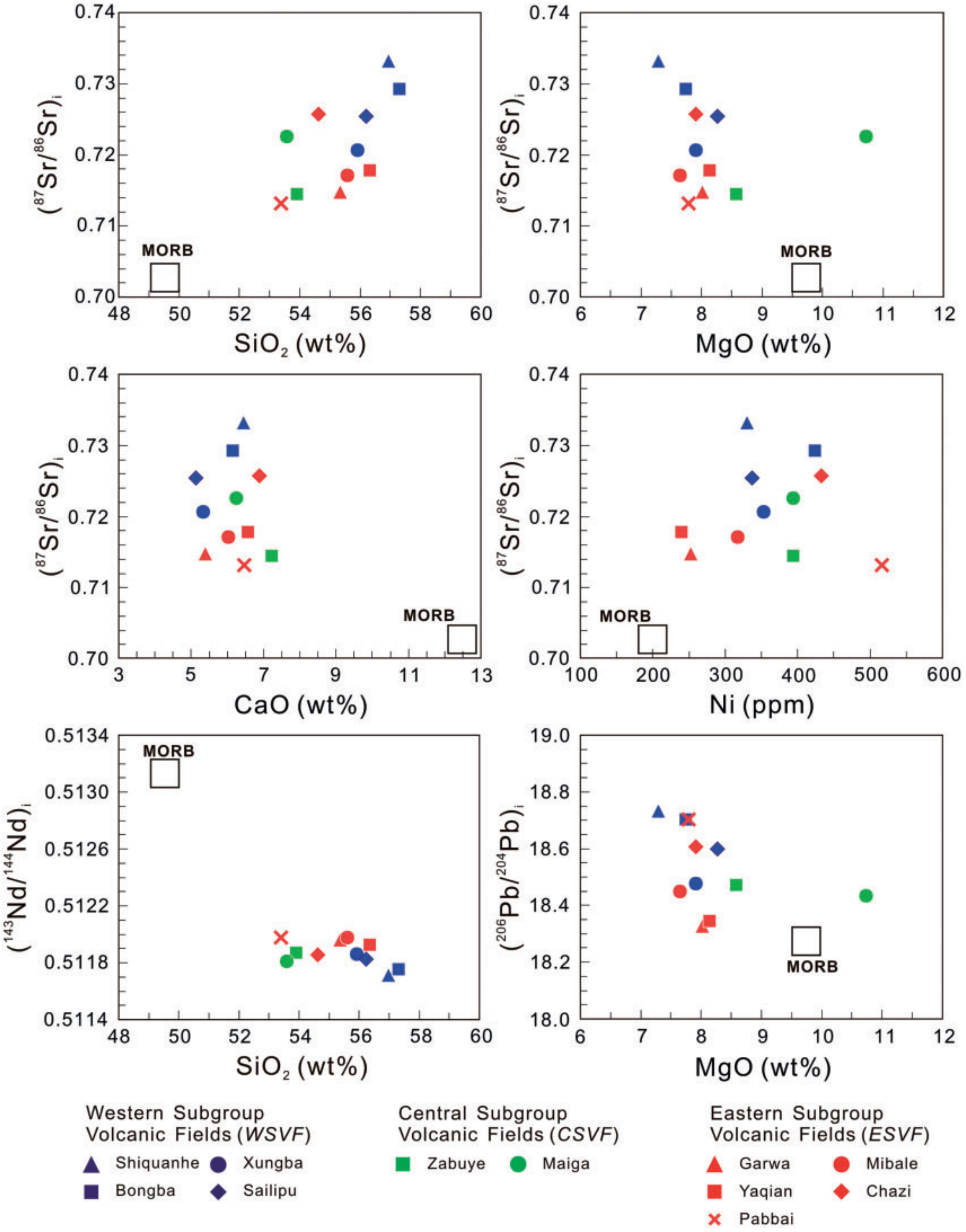

**Fig. 17.** Correlations between whole-rock Sr–Nd–Pb isotope initial ratios and selected major and trace element contents corrected to Mg# = 72 after Niu *et al.* (1999) and Humphreys & Niu (2009). Compositions of normal (N)-MORB (Presnall & Hoover, 1987; Rollinson, 1993; Hofmann, 1997; Workman & Hart, 2005) are shown for comparison. Data are from Tables 3–5.

geochemistry (Figs 11, 12, 17 and 22), together with the evidence from seismic tomography (e.g. Nábělek *et al.*, 2009), we conclude that the mantle source region of the ultrapotassic magmas comprises two components: (1) depleted MORB-source mantle (DMM) and (2) a subducted Indian eclogite-facies continental crustal component.

We have attempted to quantify the proportions of the subducted Indian eclogite-facies crustal component that contributes to the mantle source of the magmas from west to east in the Lhasa terrane, following the approach used in our earlier simulations (Guo *et al.*, 2005, 2006; Guo & Wilson, 2012). The modeling is subdivided into two steps: (1) simulation of partial melting of a subducted Indian eclogite-facies continental crustal component; (2) two-component mixing between this eclogite-facies continental crustal partial melt and the bulk peridotite of the pre-existing mantle wedge (i.e. depleted

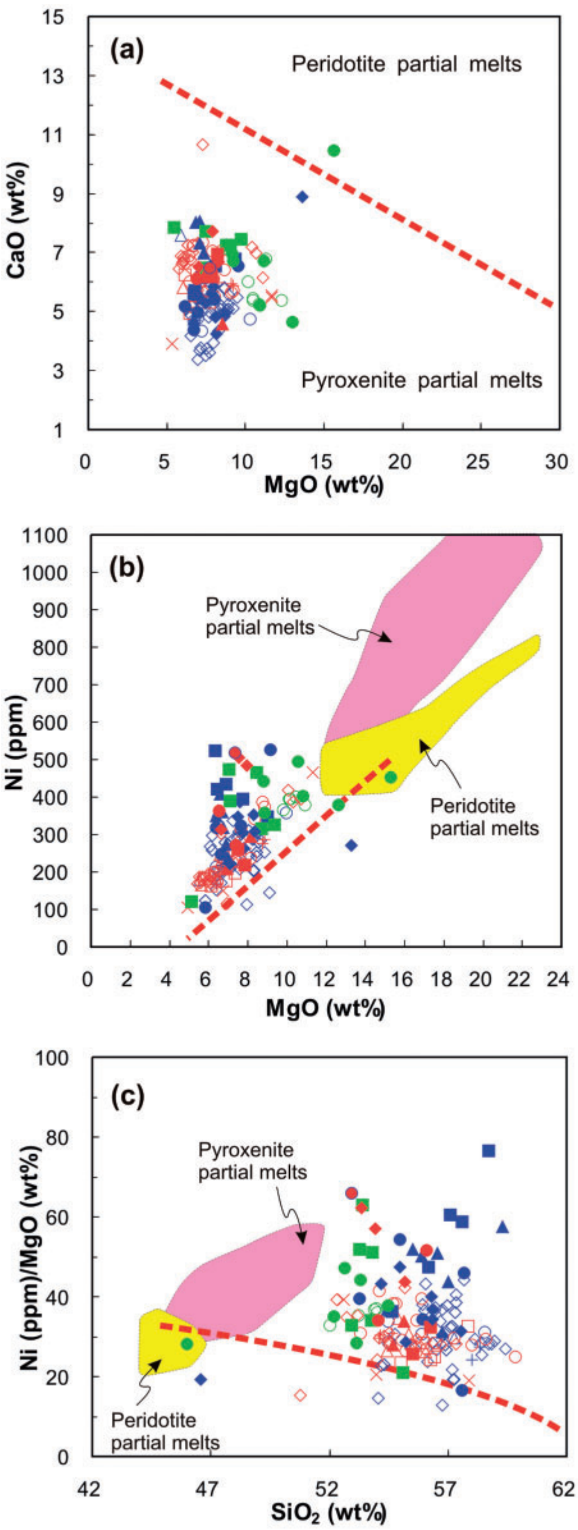

**Fig. 18.** (a) CaO (wt %) vs MgO (wt %) variations in the whole-rock compositions of the ultrapotassic magmatic rocks from the Lhasa terrane, indicating their origin as partial melts of pyroxenite. The red dashed line in (a) separates peridotite-derived melts (field above the line) from pyroxenite-derived melts (field below the line) (after Herzberg, 2011). (b) Ni (ppm) vs MgO (wt %). (c) Ni (ppm)/MgO (wt %) vs $SiO_2$ (wt %). The red dashed curves in (b) and (c) separate peridotite-derived melts (field below the curves) from pyroxenite-derived melts (field above the curves) (after Sobolev *et al.*, 2005). Compositional fields of pyroxenite-derived (pink field) and peridotite-derived (yellow field) partial melts in (b) and (c) are based on Hawaiian data (Sobolev *et al.*, 2005). Most of the ultrapotassic magmatic rocks plotted exhibit higher Ni concentrations than peridotite-derived melts in (b) and (c), suggesting a pyroxenite mantle source (see text for details). The ultrapotassic magmatic rocks from the Lhasa terrane have higher $SiO_2$ and lower MgO contents compared with those of partial melts of Hawaiian pyroxenite (Sobolev *et al.*, 2005), consistent with a contribution from a subducted continental crustal component to their mantle source. Data and symbols are as in Fig. 4a.

MORB-source mantle). Such a bulk-mixing scenario is clearly an oversimplification of the actual processes involved.

We selected the bulk-rock composition of an Indian eclogite from Rehman *et al.* (2008) as a proxy for the composition of the subducted continental crustal component in our modeling simulations. Considering the constraints on the compositional characteristics of the pre-existing mantle protolith of the source of the mafic K-rich magmas (Fig. 16), we used the composition of depleted MORB-source mantle (DMM; Workman & Hart, 2005) as a proxy for the mantle protolith. The mineral–melt partition coefficients used are given in Table 6. The model melting curve for partial melting of the eclogite (the red continuous curve with filled rhombs) and the DMM composition are shown in a plot of Dy/Yb versus La/Yb (Fig. 23). The Dy/Yb ratio of the eclogite melt is approximately constant (~7) for degrees of melting up to 50%. Two-component mixing between the eclogite-derived crustal partial melt and the pre-existing bulk mantle protolith (DMM) are shown by the black dashed lines with tick marks labeled M1, M2 and M3 (Fig. 23). The results of the modeling calculation are summarized in Tables 7 and 8.

The results of modeling the Dy/Yb vs La/Yb variations suggest that the whole-rock REE compositions of the ultrapotassic magmas could be explained by derivation from a mantle source produced by mixing between an eclogite-facies crust-derived melt and a pre-existing bulk mantle peridotite protolith (depleted MORB-source mantle) (Fig. 23), assuming that the Dy/Yb and La/Yb ratios of the ultrapotassic magmas are not significantly fractionated from those of their source. The degree of melting of the eclogite component in the western–central subgroup volcanic fields is 10–20%, whereas in the eastern subgroup volcanic field it is 2% (Fig. 23). The proportion of the eclogite-derived melt in the mixed source is 10–50% for the magmas of the western and central subgroup volcanic fields and 5–25% for the eastern subgroup volcanic field (Fig. 23). This is consistent with our inference of a decrease in the amount of the subducted Indian eclogite crustal component in the mantle source region eastward in south Tibet, as indicated by the composition of olivine phenocrysts (Figs 20 and 21).

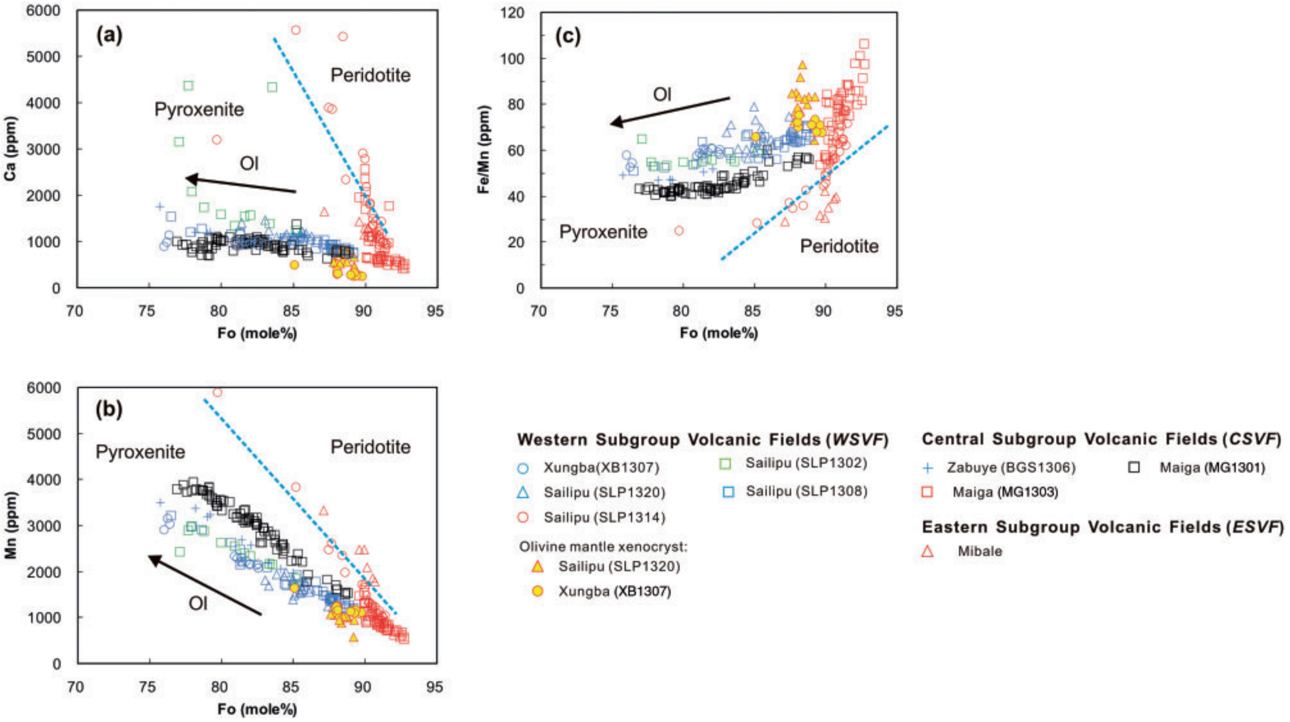

**Fig. 19.** Comparison of the olivine phenocryst compositions in the ultrapotassic magmatic rocks in south Tibet with those crystallized from partial melts of mantle peridotite and pyroxenite (after Herzberg, 2011). (a) Ca (ppm) vs Fo (mol %); (b) Mn (ppm) vs Fo (mol %); (c) Fe (ppm)/Mn (ppm) vs Fo (mol %). The olivine phenocrysts from the Lhasa terrane magmatic rocks are characterized by lower Ca and Mn contents compared with those crystallized from partial melts of mantle peridotite. This indicates a mantle pyroxenite source for the magmas, following the criteria of Herzberg (2011). We have further subdivided the pyroxenite source into olivine-bearing pyroxenite (red symbols) and olivine-free pyroxenite (other colour symbols) mantle sources according to the differences in the Ca, Mn and Fe/Mn of the olivine phenocrysts. Blue dashed lines, which separate the fields of olivine phenocrysts crystallized from partial melts of peridotite and pyroxenite, are from Herzberg (2011). The arrow labeled by 'Ol' denotes olivine fractional crystallization (Sobolev *et al.*, 2007). Data are from Supplementary Data Appendix A.

## Petrogenesis of the ultrapotassic mafic magmas in south Tibet

The mineral chemistry of olivine phenocrysts combined with whole-rock geochemical and Sr–Nd–Pb isotopic data suggest that the post-collisional ultrapotassic magmas in the Lhasa terrane are the products of partial melting of pyroxenites that were formed by reaction of partial melts and fluids derived from northward-subducted Indian eclogite-facies continental crustal materials with mantle peridotite that probably resided within the overlying mantle wedge, including the Tibetan SCLM. The significant Ta–Nb–Ti troughs and enrichment in LILE in the mantle-normalized trace element patterns of the most primitive ultrapotassic magmatic rocks (Fig. 8), combined with their similar Ce/Pb and Nb/La ratios to those in average subduction channel mélanges (Fig. 22f), further support their relationship to continental subduction. Previous studies (e.g. Li *et al.*, 2008; Zhao *et al.*, 2010, 2011; Chen *et al.*, 2015) suggested that onset of the northward underthrusting of Indian continental lithosphere beneath south Tibet immediately followed India–Asia continent–continent collision at ~55 Ma. However, the age (25–8 Ma) of the post-collisional K-rich magmatism in south Tibet (Table 1 and Fig. 2) post-dates India–Asia collision by about 30 Myr. The clear delay in the onset of K-rich magmatism and the finite duration of the magmatism (25–8 Ma) implies an existence of other factors in their petrogenesis in addition to the northward underthrusting of the Indian continental lithospheric slab. If partial melting of the mantle wedge was directly caused by the northward underthrusting of the Indian continental lithosphere, this should lead to decreasing ages for the resultant K-rich magmas from south to north, rather than the southward decreasing ages that are actually observed (Fig. 2).

On the basis of the above discussion, we conclude that northward underthrusting of the Indian continental lithosphere since India–Asia collision at ~55 Ma led to metasomatic enrichment of the overlying mantle wedge (including asthenospheric mantle and SCLM) and the formation of pyroxenites, which provided the two-component (crustal eclogite melt from the Indian continental slab reacting with MORB-source mantle) source region of the post-collisional K-rich magmas in south Tibet. Seismic tomography studies (e.g. Zhou & Murphy, 2005; Li *et al.*, 2008; Zhao *et al.*, 2010, 2011; Chen *et al.*, 2015) have indicated the continuous presence of a northward-dipping subducted slab of Indian continental lithosphere that increases in depth from south to north, suggesting the potential for continuous formation of pyroxenite in the mantle wedge since the

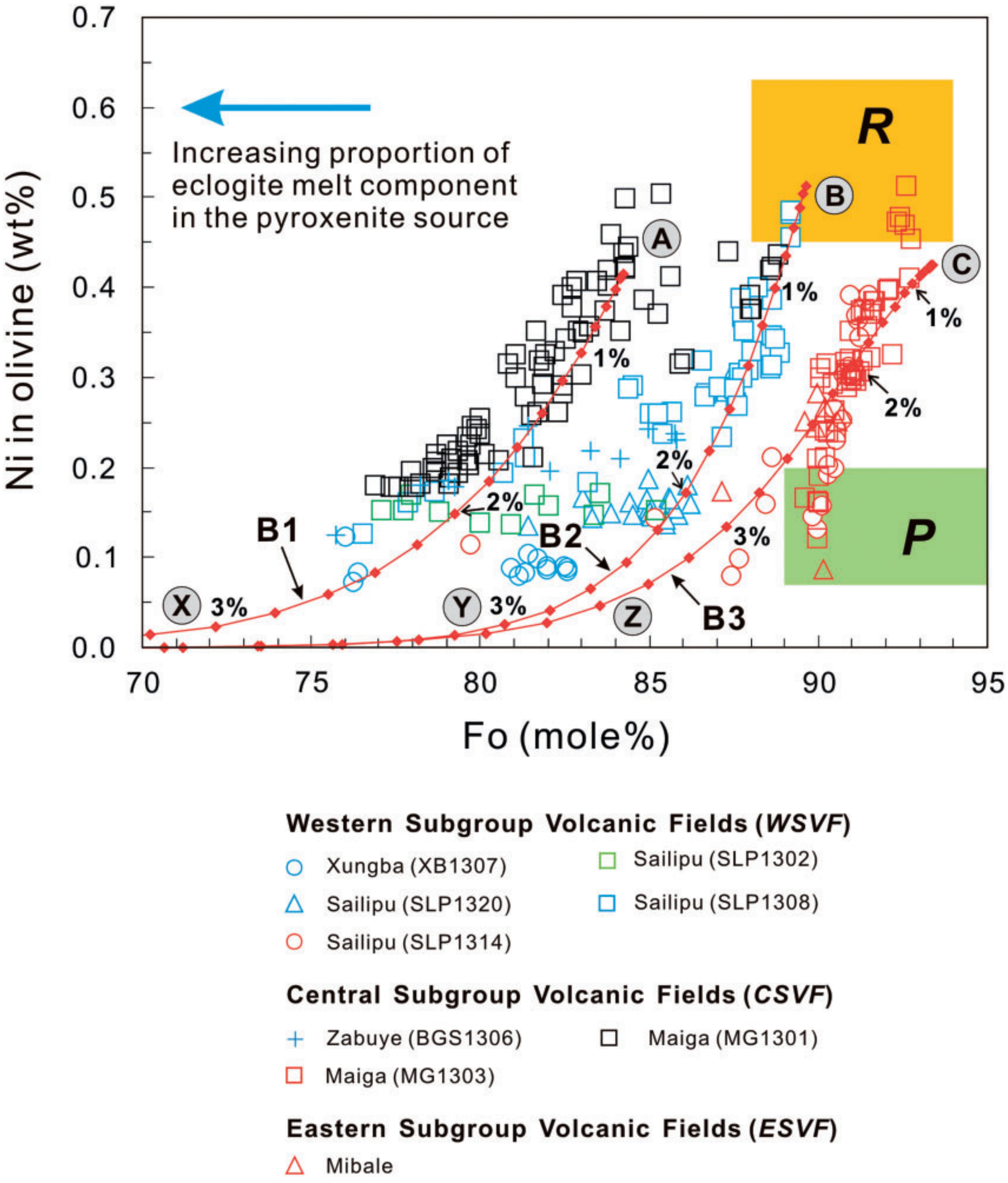

**Fig. 20.** Variation of Ni (wt %) vs Fo (mol %) in olivine phenocrysts in the post-collisional ultrapotassic magmas in south Tibet. The red modeling curves A–X, B–Y and C–Z simulate the variation trends (B1, B2 and B3) in olivine composition as a result of olivine fractionation from parental magmas A, B and C, respectively. The numbers in per cent shown on the tick marks of these three red modeling curves denote proportions of the olivine fractionation (see Supplementary Data Appendix B for the modeling calculation details). The blue arrow indicates that the parental magmas (A, B, C) were derived from pyroxenite sources containing an increasing component of partial melt from subducted Indian eclogite-facies crust from C to A. The field labeled 'R' represents the composition of olivine crystallized from partial melts of olivine-free pyroxenite. The field labeled 'P' represents the composition of olivine crystallized from partial melt of mantle peridotite. Data for the compositions of olivine phenocrysts in the Tibetan ultrapotassic magmatic rocks are from Supplementary Data Appendix A. The sample numbers shown in the legend are consistent with those in Table 3.

onset of continental subduction. However, the geodynamic event or process that could have caused melting of the pyroxenites in the metasomatized mantle wedge uniquely during the period 25–8 Ma is less clear. There must have been a critical geodynamic event between 25 and 8 Ma that resulted in the partial melting of the pyroxenites in the mantle wedge beneath south Tibet. The increasing age of the K-rich magmas from south to north in the Lhasa terrane (Table 1 and Fig. 2), combined with a northward decline in components derived from the subducted Indian continental lithosphere in the mantle source of the K-rich magmas in the eastern subgroup (Guo *et al.*, 2013), suggests that partial melting of the mantle wedge pyroxenites can be explained by the progressive roll-back of the northward-underthrusting Indian continental lithospheric slab

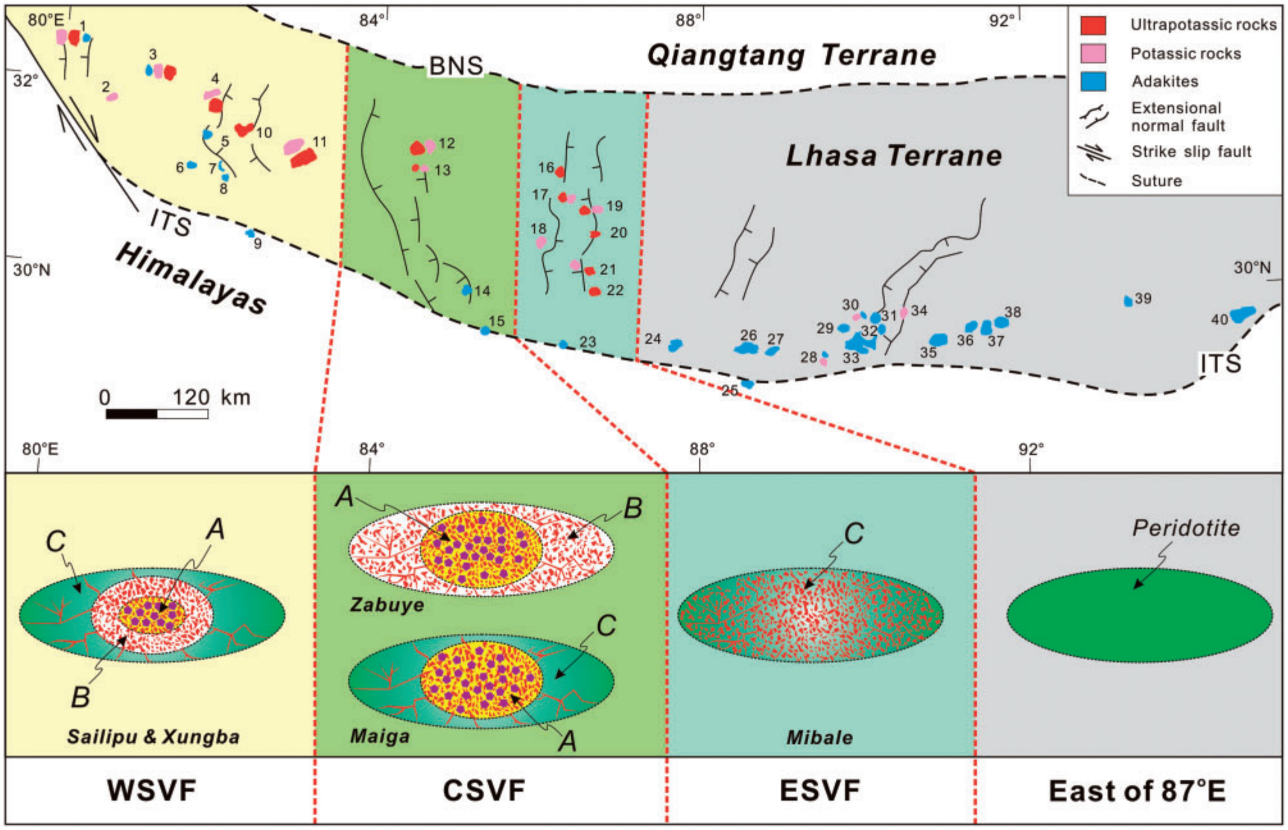

**Fig. 21.** Schematic illustration showing the mantle source components of the post-collisional mafic ultrapotassic magmas in south Tibet. A, silica-rich pyroxenite; B, olivine-free pyroxenite; C, olivine-bearing pyroxenite. WSVF, western subgroup volcanic fields; CSVF, central subgroup volcanic fields; ESVF, eastern subgroup volcanic fields. Sailipu, Xungba, Zabuye, Maiga and Mibale indicate single volcanic fields.

during the period 25–8 Ma. The decreasing trend in the age of the magmatism from west to east (Fig. 2b) may be consistent with break-off of the Indian continental slab that propagated eastwards from 25 to 8 Ma (e.g. Replumaz *et al.*, 2010, 2013, 2014; Chen *et al.*, 2015). Such slab break-off combined with slab roll-back during continental lithosphere subduction may have triggered asthenospheric mantle upwelling and caused thermal erosion of the Tibetan SCLM. Detached fragments of the Indian continental lithosphere may have undergone further melting as they subsided into the asthenosphere.

## SUMMARY

On the basis of the compositions of olivine phenocrysts, and whole-rock major element, trace element, Sr–Nd–Pb isotope and seismic tomography data, we propose a two-stage model to account for the petrogenesis of the post-collisional ultrapotassic mafic magmatism during the period 25–8 Ma in south Tibet. The first stage (55–25 Ma) involved the subduction of eclogite-facies continental crustal materials on the top of a subducted Indian continental lithospheric slab beneath south Tibet since India–Asia collision at ~55 Ma; these crustal materials could have undergone fluid release and partial melting, resulting in metasomatism of the overlying mantle wedge, forming pyroxenites. Alternatively, the subducted Indian crustal materials may have underplated the base of the Tibetan lithosphere (Fig. 24a) forming a subduction channel mélange. At this stage (55–25 Ma) there is no ultrapotassic magmatism within the Lhasa terrane and thus no evidence for pyroxenite melting (or indeed pyroxenite formation).

The second stage of the model (25–8 Ma) involved partial melting of pyroxenites caused by reaction between silica-rich melts derived from partial melting of subducted eclogite-facies crustal materials and the surrounding mantle peridotite in the mantle wedge and Tibetan SCLM (Fig. 24b). Partial melting of these pyroxenites was probably induced by upwelling of hot asthenospheric mantle in response to Indian slab roll-back and break-off, resulting in the generation of the ultrapotassic magmas (Fig. 24b). Indian slab roll-back has been linked to a sharp decrease in the convergence rate between India and Asia between 25 and 8 Ma (Lee & Lawver, 1995). There may be further metasomatism of the Tibetan lithospheric mantle during ascent of the ultrapotassic magmas (Fig. 24b).

The post-collisional ultrapotassic mafic magmatism in south Tibet is older than 8 Ma (Table 1 and Fig. 2). The absence of ultrapotassic mafic magmatism from

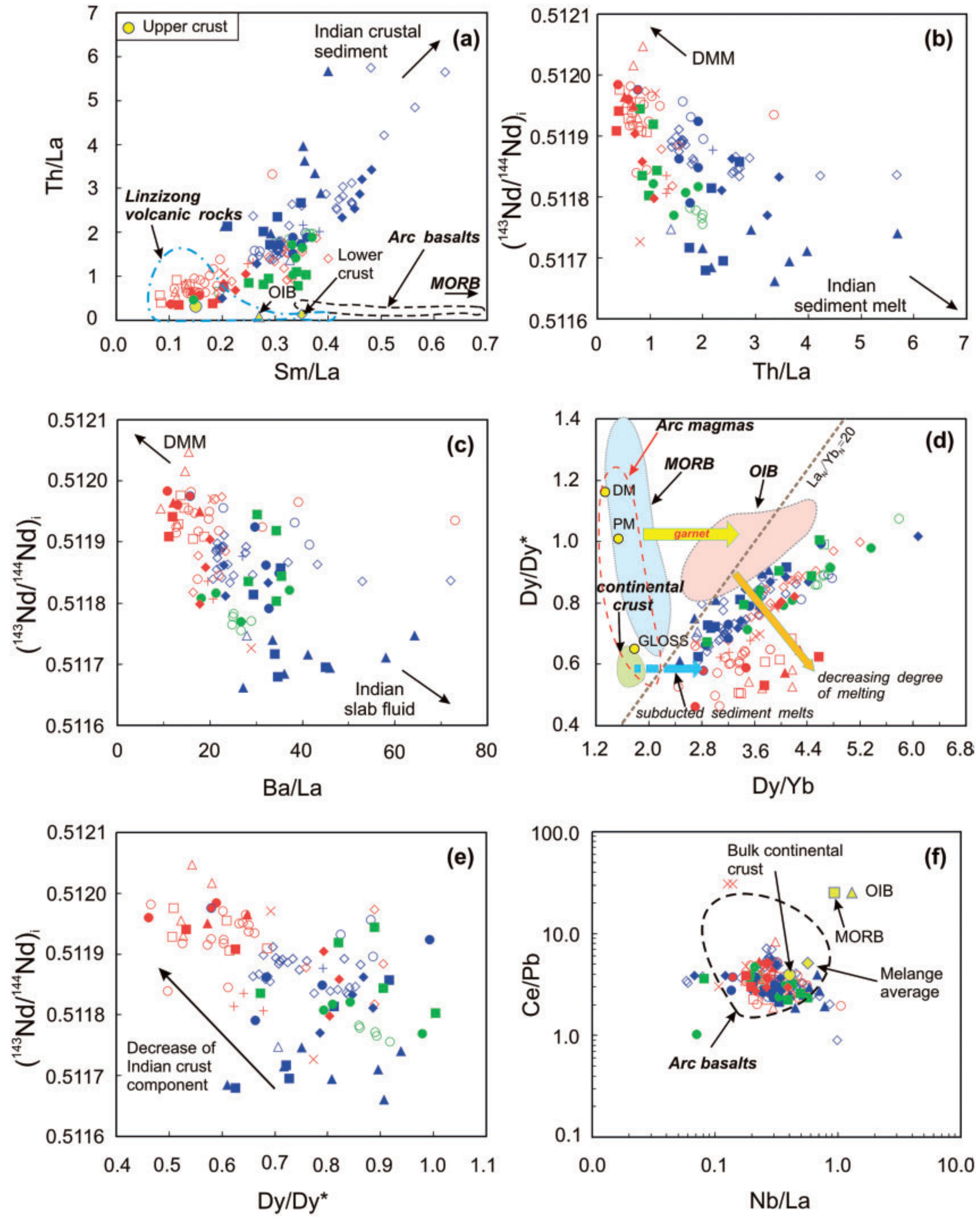

**Fig. 22.** (a) Th/La vs Sm/La. (b) $(^{143}\mathrm{Nd}/^{144}\mathrm{Nd})_i$ vs Th/La. (c) $(^{143}\mathrm{Nd}/^{144}\mathrm{Nd})_i$ vs Ba/La. (d) Dy/Dy* vs Dy/Yb. (e) $(^{143}\mathrm{Nd}/^{144}\mathrm{Nd})_i$ vs Dy/Dy*. (f) Ce/Pb vs Nb/La. The mélange average in (f) is from Marschall & Schumacher (2012). (d) is modified from Davidson *et al.* (2013); the definition of Dy/Dy* in (d) and (e) is from Davidson *et al.* (2013). Data for OIB and MORB are from Wilson (1989) and Sun & McDonough (1989). The field of arc basalts is from Plank (2005). Data for the Linzizong volcanic rocks are from Dong (2002), Mo *et al.* (2008) and Lee *et al.* (2009, 2012). The compositions of upper continental crust, lower continental crust and bulk continental crust are from Rudnick & Gao (2003). The composition of Indian continental crust is based on data from Inger & Harris (1993), Ahmad *et al.* (2000), Richards *et al.* (2005), Rehman *et al.* (2008) and Guo & Wilson (2012). Data for the Lhasa terrane ultrapotassic rocks are from Tables 3 and 4. Symbols are as in Fig. 4.

8 Ma to the present can be explained by flat slab subduction of the Indian continental lithosphere since 8 Ma, as indicated by the recent geophysical studies (e.g. Lee & Lawver, 1995; Nábělek *et al.*, 2009; Zhao *et al.*, 2011; Chen *et al.*, 2015). This flat slab subduction has eliminated the mantle wedge above the subducted Indian lithosphere, preventing the upwelling of hotter asthenospheric mantle through slab tears (Fig. 24c).

The compositions of olivine phenocrysts in the mafic K-rich magmas in the Lhasa terrane suggest a

**Table 6**: Mineral–melt partition coefficients for modeling calculations of partial melting of the Indian eclogite

| Indian eclogite | $D_{Cpx}$ | $D_{Gt}$ | $D_0$ | P |
|---|---|---|---|---|
| La | 0·0281 | 0·00270 | 0·01921 | 0·02556 |
| Dy | 0·4588 | 2·65940 | 1·22901 | 0·67886 |
| Yb | 0·5983 | 10·0544 | 3·90794 | 1·54391 |

Cpx, clinopyroxene; Gt, garnet. Data source: Liu *et al.* (2014*b*) and references therein. $D_0 = 0{\cdot}65D_{Cpx} + 0{\cdot}35D_{Gt}$ represents the bulk partition coefficient during partial melting. The proportions of the mineral phases (Cpx = 0·65, Gt = 0·35) in the Indian eclogite are from Rehman *et al.* (2008). $P = 0{\cdot}9D_{Cpx} + 0{\cdot}1D_{Gt}$ represents the bulk partition coefficient for the minerals entering the partial melt. The proportions of the mineral phases entering the melt (Cpx = 0·90, Gt = 0·10) during partial melting of the Indian eclogite are based on Guo & Wilson (2012).

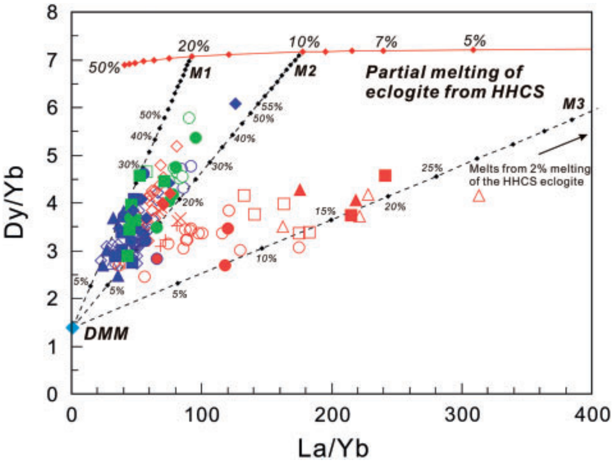

**Fig. 23.** Dy/Yb vs La/Yb variations in the ultrapotassic magmatic rocks indicating a decreasing proportion of the eclogite partial melt component in the mantle source of the magmas from west to east in south Tibet. The numbers in per cent shown on the filled rhombs of the red continuous modeling curve denote the degree of partial melting of the crustal eclogite. The bulk composition of the pre-existing mantle peridotite protolith (i.e. DMM) is from Workman & Hart (2005). The numbers in per cent shown on the filled rhombs of the black dashed modeling curves (M1, M2 and M3) represent the proportions of the eclogite-derived melt in the two-component mixture between the eclogite-derived melt and the mantle peridotite protolith (i.e. DMM). Data and symbols are as in Fig. 4.

**Table 7**: Result of the trace element modeling of partial melting of the Indian eclogite

| Degree of melting (%) | La (ppm) | Dy (ppm) | Yb (ppm) | La/Yb | Dy/Yb |
|---|---|---|---|---|---|
| 0·01 | 1165·20 | 9·45 | 1·30 | 897·06 | 7·28 |
| 0·05 | 1146·69 | 9·45 | 1·30 | 882·81 | 7·28 |
| 0·1 | 1130·32 | 9·45 | 1·30 | 870·29 | 7·28 |
| 0·5 | 966·99 | 9·44 | 1·30 | 744·43 | 7·27 |
| 1 | 853·25 | 9·42 | 1·30 | 657·43 | 7·26 |
| 2 | 672·08 | 9·39 | 1·30 | 518·49 | 7·25 |
| 3 | 556·75 | 9·36 | 1·29 | 430·38 | 7·24 |
| 5 | 398·68 | 9·30 | 1·29 | 309·13 | 7·21 |
| 7 | 307·65 | 9·23 | 1·28 | 239·54 | 7·19 |
| 8 | 275·83 | 9·20 | 1·28 | 215·36 | 7·18 |
| 9 | 249·08 | 9·17 | 1·28 | 195·00 | 7·18 |
| 10 | 226·47 | 9·13 | 1·27 | 177·80 | 7·17 |
| 15 | 153·11 | 8·98 | 1·26 | 121·21 | 7·11 |
| 20 | 115·27 | 8·82 | 1·25 | 92·32 | 7·06 |
| 25 | 92·31 | 8·65 | 1·23 | 74·93 | 7·02 |
| 30 | 76·95 | 8·49 | 1·21 | 63·39 | 6·99 |
| 35 | 65·96 | 8·32 | 1·19 | 55·23 | 6·96 |
| 40 | 57·72 | 8·14 | 1·17 | 49·17 | 6·94 |
| 45 | 51·30 | 7·97 | 1·15 | 44·54 | 6·92 |
| 50 | 46·17 | 7·79 | 1·13 | 40·90 | 6·90 |

Compositions of the Indian eclogite for the modeling calculation during partial melting are as follows: La 22·50 ppm, Dy 11·62 ppm, Yb 5·08 ppm, based on Indian eclogite sample Ph380 from Rehman *et al.* (2008). Similar modeling results can be obtained using other samples of eclogite from Rehman *et al.* (2008). The partial melting curve in Fig. 23 for Indian eclogite melting was calculated using a non-modal batch melting equation (Wilson, 1989).

**Table 8**: Modelling results for two-component mixing between an Indian eclogite-derived melt and a depleted MORB-source mantle (DMM) peridotite protolith

| Proportion of eclogite melt (%) | M1 | | M2 | | M3 | |
|---|---|---|---|---|---|---|
| | La/Yb | Dy/Yb | La/Yb | Dy/Yb | La/Yb | Dy/Yb |
| 5 | 14·53 | 2·25 | 28·03 | 2·28 | 82·09 | 2·31 |
| 10 | 25·81 | 2·95 | 50·06 | 3·00 | 147·08 | 3·04 |
| 15 | 35·08 | 3·52 | 68·09 | 3·59 | 200·08 | 3·64 |
| 20 | 42·84 | 4·00 | 83·12 | 4·08 | 244·12 | 4·14 |
| 25 | 49·43 | 4·41 | 95·85 | 4·49 | 281·30 | 4·56 |
| 30 | 55·10 | 4·76 | 106·76 | 4·85 | 313·11 | 4·92 |
| 35 | 60·02 | 5·06 | 116·23 | 5·16 | 340·63 | 5·23 |
| 40 | 64·34 | 5·33 | 124·51 | 5·43 | 364·68 | 5·51 |
| 45 | 68·16 | 5·57 | 131·81 | 5·67 | 385·87 | 5·75 |
| 50 | 71·56 | 5·78 | 138·31 | 5·88 | 404·69 | 5·96 |

M1, M2 and M3 represents modeling curves for two-component mixing (Fig. 23) between the DMM peridotite protolith and a 20%, 10% and 2% melt of the Indian eclogite, respectively. Compositions of the depleted MORB-source mantle (DMM) peridotite protolith (La 0·192 ppm, Dy 0·505 ppm, Yb 0 ·365 ppm) are from Workman & Hart (2005).

progressively increasing participation of peridotite in the mantle source region from west to east (Fig. 21). Previous studies (e.g. Hirschmann & Stolper, 1996) have shown that mantle peridotite has a higher temperature solidus and lower melt productivity relative to pyroxenite at a given pressure. Thus, pyroxenite in the mantle melts preferentially, and may produce a larger volume of melt. The eastward decrease in lava volumes and partial melting degree in south Tibet (Figs 1 and 9) is consistent with a reduction in the contribution of components from the subducted Indian continental crust to the upper-mantle wedge from west to east.

No ultrapotassic mafic magmatism (e.g. MgO >6 wt %) occurred to the east of 87°E during the period 25–8 Ma in the Lhasa terrane (Figs 1 and 21). This may indicate the absence of mantle pyroxenite to the east of 87°E, reflecting the reduction in components derived from subducted Indian continental crust. The Indian slab may also be subducting more steeply beneath the Lhasa terrane to the east of 87°E compared with further west (Zhou & Murphy, 2005; Negredo *et al.*, 2007; Chen *et al.*, 2015). Compared with west of 87°E, the lack of significant recycling of subducted Indian continental crustal materials during the northward underthrusting

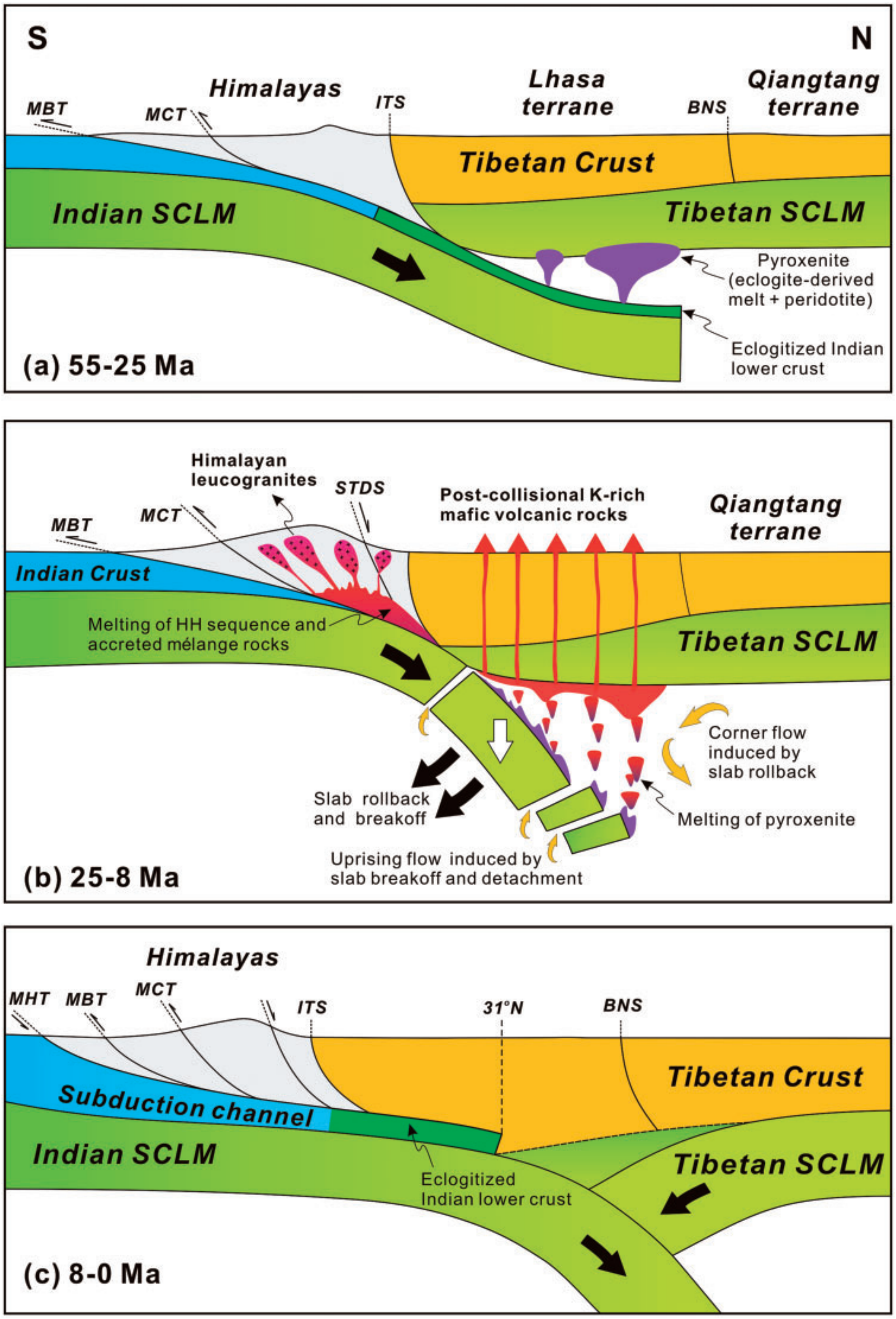

**Fig. 24**. Petrogenetic model for the post-collisional ultrapotassic mafic magmatism from 25 to 8 Ma in south Tibet. (a) 55–25 Ma: northward subduction of Indian continental lithosphere beneath the Lhasa terrane during this early stage resulted in compressional deformation in south Tibet, the occurrence of the eclogite-facies crustal materials on the top of the subducted Indian slab and formation of pyroxenites within the mantle wedge and in the Tibetan SCLM as a consequence of reaction of partial melts and fluids derived from subducted Indian eclogite-facies continental crustal materials with ambient mantle peridotite. (b) 25–8 Ma: generation of post-collisional leucogranites in the Himalayas and ultrapotassic mafic magmas in the Lhasa terrane of south Tibet. Slab rollback and break-off induced upper plate extension and asthenospheric upwelling as a counterflow. This is the period in which the pyroxenites that formed in the metasomatized SCLM and asthenospheric mantle wedge partially melted to produce the ultrapotassic magmas. The petrogenesis of the Himalayan leucogranites has been discussed by Guo & Wilson (2012). (c) 8 Ma–present: flat slab subduction of Indian continental lithosphere during this late stage has eliminated the wedge of upwelling asthenospheric mantle and Tibetan SCLM, terminating the mafic ultrapotassic magmatism. The cross-section of the India–Asia collision zone during the period 8 Ma to the present is based on geophysical constraints (e.g. Nábělek *et al.*, 2009, fig. 2D). The eclogite-facies Indian lower continental crust (green shading) underplates the Himalayas and Tibet to 31°N. BNS, Bangong–Nujiang suture; ITS, Indus–Tsangpo suture; MBT, Main Boundary thrust; MCT, Main Central thrust; MHT, Main Himalayan thrust; STDS, south Tibetan detachment system. Filled red triangles represent the locations of post-collisional potassium-rich mafic magmatism in south Tibet. The white arrow denotes the detachment of the Indian continental slab.

of the Indian slab may have led to a relatively hot and dry mantle wedge to the east of 87°E. This is consistent with the estimated temperatures of up to 1300°C and pressures of 24 kbar for granulite-facies crustal xenoliths entrained in a Miocene K-rich dyke intruded into the eastern Lhasa terrane (Chan *et al.*, 2009).

## ACKNOWLEDGEMENTS

We are grateful to Professor J. Liu, Dr S. Chen and Dr W. Guo for their support. We thank X. Liu, J. Qu and D. Yang for their assistance with the fieldwork and constructive discussions. Professor Q. Mao and Y. Ma are thanked for their help with electron microprobe analyses, Professor H. Li for help with major element analyses, and Professor X. Jin for her help with the trace element analyses. Professor C. Li, J. Qiu, R. Xu and Z. Chu are thanked for their assistance with the Sr–Nd–Pb isotope analyses. Professor N. W. Rogers, Yong-Jun Lu and an anonymous referee are acknowledged for their extremely constructive reviews of an earlier version of the paper. We thank the journal editor, Simon Turner, for his support.

## FUNDING

This study was supported by a grant from Strategic Priority Research Program (B) of the Chinese Academy of Sciences (Grant No. XDB03010600), grants from the National Natural Science Foundation of China (NSFC) (Nos 41020124002 and 41130314) and by a joint project between the Royal Society of London and NSFC.

## SUPPLEMENTARY DATA

Supplementary data for this paper are available at *Journal of Petrology* online.

## REFERENCES

Ahmad, T., Harris, N., Bickle, M., Chapman, H., Bunbury, J. & Prince, C. (2000). Isotopic constraints on the structural relationships between the Lesser Himalayan Series and the High Himalayan Crystalline Series, Garhwal Himalaya. *Geological Society of America Bulletin* **112**(**3**), 467–477.

Arnaud, N., Vidal, P., Tapponnier, P., Matte, P. & Deng, W. (1992). The high $K_2O$ volcanism of northwestern Tibet: geochemistry and tectonic implications. *Earth and Planetary Science Letters* **111**, 351–367.

Beattie, P., Ford, C. & Russell, D. (1991). Partition coefficients for olivine–melt and orthopyroxene–melt systems. *Contributions to Mineralogy and Petrology* **109**, 212–224.

Boari, E., Avanzinelli, R., Melluso, L., Giordano, G., Mattei, M., De Benedetti, A. A., Morra, V. & Conticelli, S. (2009). Isotope geochemistry (Sr–Nd–Pb) and petrogenesis of leucite-bearing volcanic rocks from 'Colli Albani' volcano, Roman Magmatic Province, Central Italy: inferences on volcano evolution and magma genesis. *Bulletin of Volcanology* **71**, 977–1005.

Brounce, M., Kelley, K. & Cottrell, E. (2014). Variations in $Fe^{3+}/\sum Fe$ of Mariana arc basalts and mantle wedge $f_{O2}$. *Journal of Petrology* **55**, 2513–2536.

Brunsmann, A., Franz, G., Erzinger, J. & Landwehr, D. (2000). Zoisite- and clinozoisite-segregations in metabasites (Tauern Window, Austria) as evidence for high-pressure fluid–rock interaction. *Journal of Metamorphic Geology* **18**, 1–22.

Chan, G. H. N., Waters, D. J., Searle, M. P., Aitchison, J., Horstwood, M., Crowley, Q., Lo, C. H. & Chan, J. S. L. (2009). Probing the basement of southern Tibet: evidence from crustal xenoliths entrained in a Miocene ultrapotassic dyke. *Journal of the Geological Society, London* **166**, 45–52.

Chen, J., Xu, J., Wang, B., Kang, Z. & Jie, L. (2010). Origin of Cenozoic alkaline potassic volcanic rocks at KonglongXiang, Lhasa terrane, Tibetan Plateau: Products of partial melting of a mafic lower-crustal source? *Chemical Geology* **273**, 286–299.

Chen, J., Xu, J., Zhao, W., Dong, Y., Wang, B. & Kang, Z. (2011). Geochemical variations in Miocene adakitic rocks from the western and eastern Lhasa terrane: implications for lower crustal flow beneath the Southern Tibetan Plateau. *Lithos* **125**, 928–939.

Chen, J., Zhao, W., Xu, J., Wang, B. & Kang, Z. (2012). Geochemistry of Miocene trachytes in Bugasi, Lhasa block, Tibetan Plateau: mixing products between mantle- and crust-derived melts? *Gondwana Research* **21**, 112–122.

Chen, Y., Zhang, Y., Graham, D., Su, S. & Deng, J. (2007). Geochemistry of Cenozoic basalts and mantle xenoliths in northeast China. *Lithos* **96**, 108–126.

Chen, Y., Li, W., Yuan, X. H., Badal, J. & Teng, J. W. (2015). Tearing of the Indian lithospheric slab beneath southern Tibet revealed by SKS-wave splitting measurments. *Earth and Planetary Science Letters* **413**, 13–24.

Chung, S., Liu, D., Ji, J., Chu, M., Lee, H., Wen, D., Lo, C., Lee, T., Qian, Q. & Zhang, Q. (2003). Adakites from continental collision zones: melting of thickened lower crust beneath southern Tibet. *Geology* **31**, 1021–1024.

Chung, S., Chu, M., Zhang, Y., Xie, Y., Lo, C., Lee, T., Lan, C., Li, X., Zhang, Q. & Wang, Y. (2005). Tibetan tectonic evolution inferred from spatial and temporal variations in post-collisional magmatism. *Earth-Science Reviews* **68**, 173–196.

Class, C., Miller, D. M., Goldstein, S. L. & Langmuir, C. H. (2000). Distinguishing melt and fluid subduction components in Umnak Volcanics, Aleutian Arc. *Geochemistry, Geophysics, Geosystems* **1**, 1004–1030.

Conticelli, S., Guarnieri, L., Farinelli, A., Mattei, M., Avanzinelli, R., Bianchini, G., Boari, E., Tommasini, S., Tiepolo, M. & Prelević, D. (2009). Trace elements and Sr–Nd–Pb isotopes of K-rich, shoshonitic, and calc-alkaline magmatism of the western Mediterranean Region: genesis of ultrapotassic to calc-alkaline magmatic associations in a post-collisional geodynamic setting. *Lithos* **107**, 68–92.

Contini, S., Venturelli, G., Toscani, L., Capedri, S. & Barbieri, M. (1993). Cr–Zr-armalcolite-bearing lamproites of Cancarix, SE Spain. *Mineralogical Magazine* **57**, 203–216.

Coulon, C., Maluski, H., Bollinger, C. & Wang, S. (1986). Mesozoic and Cenozoic volcanic rocks from central and southern Tibet: $^{39}Ar$–$^{40}Ar$ dating, petrological characteristics and geodynamical significance. *Earth and Planetary Science Letters* **79**, 281–302.

Davidson, J., Turner, S. & Plank, T. (2013). Dy/Dy*: variations arising from mantle sources and petrogenetic processes. *Journal of Petrology* **54**, 525–537.

DeCelles, P. G. (2002). Implications of shortening in the Himalayan fold–thrust belt for uplift of the Tibetan Plateau. *Tectonics* **21**, 1062, doi:10.1029/2001TC001322.

DePaolo, D. J. (1988). *Neodymium Isotope Geochemistry: an Introduction*. Springer, 230 pp.

Ding, L., Kapp, P., Zhong, D. & Deng, W. (2003). Cenozoic volcanism in Tibet: evidence for a transition from oceanic to continental subduction. *Journal of Petrology* **44**, 1833–1865.

Ding, L., Yue, Y., Cai, F., Xu, X., Zhang, Q. & Lai, Q. (2006). $^{40}$Ar/$^{39}$Ar geochronology, geochemical and Sr–Nd–O isotopic characteristics of the high-Mg ultrapotassic rocks in Lhasa block of Tibet: implications in the onset time and depth of NS-striking rift system. *Acta Geologica Sinica* **80**, 1252–1261 (in Chinese with English abstract).

Dong, G. C. (2002). Linzizong volcanic rocks in Linzhou volcanic basin, south Tibet: implication for India–Eurasia collision process. PhD thesis, China University of Geosciences, Beijing, 134 pp. (in Chinese).

Feineman, M. D., Ryerson, F. J., DePaolo, D. J. & Plank, T. (2007). Zoisite–aqueous fluid trace element partitioning with implications for subduction zone fluid composition. *Chemical Geology* **239**, 250–265.

Foley, S. F., Venturelli, G., Green, D. H. & Toscani, L. (1987). The ultrapotassic rocks: Characteristics, classification, and constraints for petrogenetic models. *Earth-Science Reviews* **24**, 81–134.

Foley, S. F., Prelević, D., Rehfeldt, T. & Jacob, D. E. (2013). Minor and trace elements in olivines as probes into early igneous and mantle melting process. *Earth and Planetary Science Letters* **363**, 181–191.

Frei, D., Liebscher, A., Franz, G. & Dulski, P. (2004). Trace element geochemistry of epidote minerals. In: Liebscher, A. & Franz, G. (eds) *Epidotes. Mineralogical Society of America and Geochemical Society, Reviews in Mineralogy and Geochemistry* **56**, 553–605.

Frey, F. A., Green, D. H. & Roy, S. D. (1978). Integrated models of basalt petrogenesis: a study of quartz tholeiites to olivine melilitites from southeastern Australia utilizing geochemical and experimental petrological data. *Journal of Petrology* **19**(**3**), 463–513.

Furman, T. & Graham, D. (1999). Erosion of lithospheric mantle beneath the East African Rift system: geochemical evidence from the Kivu volcanic province. *Lithos* **48**, 237–262.

Gao, Y., Hou, Z., Kamber, B. S., Wei, R., Meng, X. & Zhao, R. (2007). Lamproitic rocks from a continental collision zone: evidence for recycling of subducted Tethyan oceanic sediments in the mantle beneath southern Tibet. *Journal of Petrology* **48**, 729–752.

Gasperini, D., Blichert-Toft, J., Bosch, D., Del Moro, A., Macera, P. & Albarède, F. (2002). Upwelling of deep mantle material through a plate window: evidence from the geochemistry of Italian basaltic volcanics. *Journal of Geophysical Research* **107**, 2367–2386.

Geological Survey Bureau of Chengdu University of Technology (2006). *Geological Survey Report of the Sailipu region in the Lhasa terrane, south Tibet*. Press of Chengdu University of Technology, 374 pp. (in Chinese).

Gill, J. B. (1981). *Orogenic Andesites and Plate Tectonics*. Springer, 390 pp.

Goldstein, S., O'Nions, R. & Hamilton, P. (1984). A Sm–Nd isotopic study of atmospheric dusts and particulates from major river systems. *Earth and Planetary Science Letters* **70**, 221–236.

Govindaraju, K. (1994). Compilation of working values and sample description for 383 geostandards. *Geostandards Newsletter* **18**(**special issue**), 1–158.

Guo, Z., Hertogen, J., Liu, J., Pasteels, P., Boven, A., Punzalan, L., He, H., Luo, X. & Zhang, W. (2005). Potassic magmatism in western Sichuan and Yunnan provinces, SE Tibet, China: petrological and geochemical constraints on petrogenesis. *Journal of Petrology* **46**, 33–78.

Guo, Z. F. & Wilson, M. (2012). The Himalayan leucogranites: constraints on the nature of their crustal source region and geodynamic setting. *Gondwana Research* **22**, 360–376.

Guo, Z. F., Wilson, M., Liu, J. Q. & Mao, Q. (2006). Post-collisional, potassic and ultrapotassic magmatism of the northern Tibetan Plateau: constraints on characteristics of the mantle source, geodynamic setting and uplift mechanisms. *Journal of Petrology* **47**, 1177–1220.

Guo, Z. F., Wilson, M. & Liu, J. Q. (2007). Post-collisional adakites in south Tibet: products of partial melting of subduction-modified lower crust. *Lithos* **96**, 205–224.

Guo, Z. F., Wilson, M., Zhang, M. L., Cheng, Z. H. & Zhang, L. H. (2013). Post-collisional, K-rich mafic magmatism in south Tibet: constraints on Indian slab-to-wedge transport processes and plateau uplift. *Contributions to Mineralogy and Petrology* **165**, 1311–1340.

Guo, Z. F., Wilson, M., Zhang, L. H., Zhang, M. L., Cheng, Z. H. & Liu, J. Q. (2014). The role of subduction channel mélanges and convergent subduction systems in the petrogenesis of post-collisional K-rich mafic magmatism in NW Tibet. *Lithos* **198–199**, 184–201.

Hart, S. R. (1984). A large–scale isotope anomaly in the Southern Hemisphere mantle. *Nature* **309**, 753–757.

Hauri, E. H. (1996). Major-element variability in the Hawaiian mantle plume. *Nature* **382**, 415–419.

Hawkesworth, C., Turner, S., McDermott, F., Peate, D. & Van Calsteren, P. (1997). U–Th isotopes in arc magmas: implications for element transfer from the subducted crust. *Science* **276**, 551–555.

Herzberg, C. (2011). Identification of source lithology in the Hawaiian and Canary Islands: implications for origins. *Journal of Petrology* **52**, 113–146.

Hirschmann, M. M. & Stolper, E. M. (1996). A possible role for garnet pyroxenite in the origin of the 'garnet signature' in MORB. *Contributions to Mineralogy and Petrology* **124**, 185–208.

Hofmann, A.W. (1997). Mantle geochemistry: the message from oceanic volcanism. *Nature* **385**, 219–229.

Hou, Z., Gao, Y., Qu, X., Rui, Z. & Mo, X. (2004). Origin of adakitic intrusives generated during mid-Miocene east–west extension in southern Tibet. *Earth and Planetary Science Letters* **220**, 139–155.

Hou, Z. Q., Zheng, Y. C., Yang, Z. M., Rui, Z. Y., Zhao, Z. D., Jiang, S. H., Qu, X. M. & Sun, Q. Z. (2013). Contribution of mantle components within juvenile lower-crust to collisional zone porphyry Cu systems in Tibet. *Mineralium Deposita* **48**, 173–192.

Humphreys, E. R. & Niu, Y. (2009). On the composition of ocean island basalts (OIB): The effects of lithospheric thickness variation and mantle metasomatism. *Lithos* **112**, 118–136.

Inger, S. & Harris, N. (1993). Geochemical constraints on leucogranite magmatism in the Langtang Valley, Nepal Himalaya. *Journal of Petrology* **34**, 345–368.

Jacobsen, S. B. & Wasserburg, G. (1980). Sm–Nd isotopic evolution of chondrites. *Earth and Planetary Science Letters* **50**, 139–155.

Jiang, Y. (2003). Mesozoic and Cenozoic tectonomagmatic evolution and mineralization in the Cuoqin area, Mid-Gangdise, Tibet. PhD thesis, Chengdu University of Technology, Beijing, 205 pp. (in Chinese with English abstract).

Johnson, M. C. & Plank, T. (1999). Dehydration and melting experiments constrain the fate of subducted sediments. *Geochemistry, Geophysics, Geosystems* **1**, 1007, doi:10.1029/1999GC000014.

Kapp, P., Yin, A., Manning, C. E., Harrison, T. M., Taylor, M. H. & Ding, L. (2003). Tectonic evolution of the early Mesozoic blueschist-bearing Qiangtang metamorphic belt, central Tibet. *Tectonics* **22**, 1043, doi:10.1029/2002TC001383.

Kinzler, R. J., Grove, T. L. & Recca, S. I. (1990). An experimental study on the effect of temperature and melt composition on the partitioning of nickel between olivine and silicate melt. *Geochimica et Cosmochimica Acta* **54**, 1255–1265.

Klootwijk, C. T., Gee, J. S., Peirce, J. W., Smith, G. M. & McFadden, P. L. (1992). An early India–Asia contact: paleomagnetic constraints from Ninetyeast ridge, ODP Leg 121. *Geology* **20**(**5**), 395–398.

Langmuir, C. H., Bender, J. F., Bence, A. E., Hanson, G. N. & Taylor, S. R. (1977). Petrogenesis of basalts from the FAMOUS area: Mid-Atlantic ridge. *Earth and Planetary Science Letters* **36**, 133–156.

Langmuir, C. H., Klein, E. M. & Plank, T. (1992). Petrological systematics of mid-ocean ridge basalts: constraints on melt generation beneath ocean ridges. In: Morgan, J. P., Blackman, D. K. & Sinton, J. M. (eds) *Mantle Flow and Melt Generation at Mid-Ocean Ridges. American Geophysical Union, Geophysical Monograph* **71**, 183–280.

Le Bas, M., Le Maitre, R., Streckeisen, A. & Zanettin, B. (1986). A chemical classification of volcanic rocks based on the total alkali–silica diagram. *Journal of Petrology* **27**, 745–750.

Lee, H., Chung, S., Lo, C., Ji, J., Lee, T., Qian, Q. & Zhang, Q. (2009). Eocene Neotethyan slab breakoff in southern Tibet inferred from the Linzizong volcanic record. *Tectonophysics* **477**, 20–35.

Lee, H., Chung, S., Ji, J., Qian, Q., Gallet, S., Lo, C., Lee, T. & Zhang, Q. (2012). Geochemical and Sr–Nd isotopic constraints on the genesis of the Cenozoic Linzizong volcanic successions, southern Tibet. *Journal of Asian Earth Sciences* **53**, 96–114.

Lee, T. & Lawver, L. A. (1995). Cenozoic plate reconstruction of Southeast Asia. *Tectonophysics* **251**, 85–138.

Leech, M. L., Singh, S., Jain, A., Klemperer, S. L. & Manickavasagam, R. (2005). The onset of India–Asia continental collision: early, steep subduction required by the timing of UHP metamorphism in the western Himalaya. *Earth and Planetary Science Letters* **234**, 83–97.

Le Maitre, R. W., Bateman, P., Dudek, A., Keller, J., Lameyre, J., Le Bas, M., Sabine, P., Schmid, R., Sorensen, H. & Streckeisen, A. (1989). *A Classification of Igneous Rocks and Glossary of Terms: Recommendations of the International Union of Geological Sciences Subcommission on the Systematics of Igneous Rocks*. Blackwell Scientific.

Li, C., Van der Hilst, R. D., Meltzer, A. S. & Engdahl, E. R. (2008). Subduction of the Indian lithosphere beneath the Tibetan Plateau and Burma. *Earth and Planetary Science Letters* **274**, 157–168.

Liao, S., Chen, Z., Luo, Z. & Zhou, A. (2002). Discovery of leucite phonolite in the Tangra Yumco area, Tibet and its geological significance. *Geological Bulletin of China* **21**, 735–738 (in Chinese with English abstract).

Liu, C. Z., Wu, F. Y., Chung, S. L. & Zhao, Z. D. (2011a). Fragments of hot and metasomatized mantle lithosphere in Middle Miocene ultrapotassic lavas, southern Tibet. *Geology* **39**, 923–926.

Liu, D., Zhao, Z. D., Zhu, D. C., Wang, Q., Sui, Q. L., Liu, Y. S., Hu, Z. C. & Mo, X. X. (2011b). The petrogenesis of post-collisional potassic–ultrapotassic rocks in Xungba basin, western Lhasa terrane: constraints from zircon U–Pb geochronology and geochemistry. *Acta Petrologica Sinica* **27**, 2045–2059 (in Chinese with English abstract).

Liu, C. Z., Wu, F. Y., Chung, S. L., Li, Q. L., Sun, W. D. & Ji, W. Q. (2014a). A 'Hidden' $^{18}$O-enriched reservoir in the sub-arc mantle. *Scientific Reports* **4**, 4232–4238.

Liu, D., Zhao, Z. D., Zhu, D., Niu, Y. L., DePaolo, D. J., Harrison, T. M., Mo, X. X., Dong, G. C., Zhou, S., Sun, C. G., Zhang, Z. C. & Liu, J. L. (2014b). Post-collisional potassic and ultrapotassic rocks in southern Tibet: Mantle and crustal origins in response to India–Asia collision and convergence. *Geochimica et Cosmochimica Acta* **143**, 207–231.

Liu, D., Zhao, Z., Zhu, D., Niu, Y. & Harrison, T. M. (2014c). Zircon xenocrysts in Tibetan ultrapotassic magmas: imaging the deep crust through time. *Geology* **42**, 43–46.

Lugmair, G. & Marti, K. (1978). Lunar initial $^{143}$Nd/$^{144}$Nd: Differential evolution of the lunar crust and mantle. *Earth and Planetary Science Letters* **39**, 349–357.

Ma, R., Liu, D., Tao, X., Shi, H. & Hu, X. (2002). Discovery of Tertiary potassium-rich magmatic rocks in the Coqen area, Tibet. *Geological Bulletin of China* **21**, 728–731 (in Chinese with English abstract).

Mahéo, G., Guillot, S., Blichert-Toft, J., Rolland, Y. & Pêcher, A. (2002). A slab breakoff model for the Neogene thermal evolution of South Karakorum and South Tibet. *Earth and Planetary Science Letters* **195**, 45−58.

Marschall, H. R. & Schumacher, J. C. (2012). Arc magmas sourced from mélange diapirs in subduction zones. *Nature Geoscience* **5**, 862–867.

McCulloch, M. & Black, L. (1984). Sm–Nd isotopic systematics of Enderby Land granulites and evidence for the redistribution of Sm and Nd during metamorphism. *Earth and Planetary Science Letters* **71**, 46–58.

Meng, L., Wang, C. S., Zhao, X. X., Coe, R., Li, Y. L. & Finn, D. (2012). Indian–Asia collision was at 24°N and 50 Ma: palaeomagnetic proof from southernmost Asia. *Scientific Reports* **2**, 925–936.

Miller, C., Schuster, R., Klötzli, U., Frank, W. & Purtscheller, F. (1999). Post-collisional potassic and ultrapotassic magmatism in SW Tibet: geochemical and Sr–Nd–Pb–O isotopic constraints for mantle source characteristics and petrogenesis. *Journal of Petrology* **40**, 1399–1424.

Mo, X., Dong, G., Zhao, Z., Guo, T., Wang, L. & Chen, T. (2005). Timing of magma mixing in the Gangdise magmatic belt during the India–Asia collision: zircon SHRIMP U–Pb dating. *Acta Geologica Sinica, English Edition* **79**, 66–76.

Mo, X., Zhao, Z., Deng, J., Flower, M., Yu, X., Luo, Z., Li, Y., Zhou, S., Dong, G. & Zhu, D. (2006). Petrology and geochemistry of post-collisional volcanic rocks from the Tibetan plateau: Implications for lithosphere heterogeneity and collision-induced asthenospheric mantle flow. In: Dilek, Y. & Pavlides, S. (eds) *Post-collisional tectonics and magmatism in the Mediterranean Region and Asia. Geological Society of America, Special Papers* **409**, 507–530.

Mo, X., Niu, Y., Dong, G., Zhao, Z., Hou, Z., Zhou, S. & Ke, S. (2008). Contribution of syn-collisional felsic magmatism to continental crust growth: a case study of the Paleogene Linzizong volcanic succession in southern Tibet. *Chemical Geology* **250**, 49–67.

Nábělek, J., Hetényi, G., Vergne, J., Sapkota, S., Kafle, B., Jiang, M., Su, H., Chen, J., Huang, B. S. & Hi-CLIMB Team (2009). Underplating in the Himalaya–Tibet collision zone revealed by the Hi-CLIMB experiment. *Science* **325**, 1371–1374.

Najman, Y., Appel, E., Boudagher-Fadel, M., Bown, P., Carter, A., Garzanti, E., Godin, L., Han, J., Liebke, U. & Oliver, G. (2010). Timing of India–Asia collision: geological, biostratigraphic, and palaeomagnetic constraints. *Journal of Geophysical Research (Solid Earth)* **115**, 12416.

Negredo, A. M., Replumaz, A., Villaseñor, A. & Guillot, S. (2007). Modeling the evolution of continental subduction processes in the Pamir–Hindu Kush region. *Earth and Planetary Science Letters* **259**, 212–225.

Nelson, D. R. (1992). Isotopic characteristics of potassic rocks: evidence for the involvement of subducted sediments in magma genesis. *Lithos* **28**, 403–420.

Niu, Y., Zhao, Z., Zhu, D. & Mo, X. (2013). Continental collision zones are primary sites for net continental crust growth-A testable hypothesis. *Earth-Science Reviews* **127**, 96–110.

Niu, Y., Collerson, K. D., Batiza, R., Wendt, J. I. & Regelous, M. (1999). Origin of enriched-type mid-ocean ridge basalt at ridges far from mantle plumes: The East Pacific Rise at 1°20′N. *Journal of Geophysical Research* **104**, 7067–7087.

Nixon, P., Thirlwall, M., Buckley, F. & Davies, C. (1984). Spanish and Western Australian lamproites: aspects of whole rock geochemistry. In: Kornprobst, J. (ed.) *Proceedings of the Third International Kimberlite Conference: I. Kimberlites and Related Rocks*. Amsterdam: Elsevier, 285–296.

Nomade, S., Renne, P. R., Mo, X., Zhao, Z. & Zhou, S. (2004). Miocene volcanism in the Lhasa block, Tibet: spatial trends and geodynamic implications. *Earth and Planetary Science Letters* **221**, 227–243.

Owen, J. (2008). Geochemistry of lamprophyres from the Western Alps, Italy: implications for the origin of an enriched isotopic component in the Italian mantle. *Contributions to Mineralogy and Petrology* **155**, 341–362.

Pan, G., Zhu, D., Wang, L., Liao, Z., Geng, Q. & Jiang, X. (2004). Bangong Lake–Nu River suture zone—the northern boundary of Gondwanaland: evidence from geology and geophysics. *Earth Science Frontiers* **11**, 371–382 (in Chinese with English abstract).

Patriat, P. & Achache, J. (1984). India–Eurasia collision chronology has implications for crustal shortening and driving mechanism of plates. *Nature* **311**, 615–621.

Pearce, J. A. (1982). Trace element characteristics of lavas from destructive plate boundaries. In: Thorpe, R. S. (eds) *Andesites*. John Wiley, pp. 525–548.

Pearce, J. A. & Mei, H. (1988). Volcanic rocks of the 1985 Tibet Geotraverse: Lhasa to Golmud. *Philosophical Transactions of the Royal Society of London, Series A* **327**, 169–201.

Peccerillo, A. & Taylor, S. R. (1976). Geochemistry of Eocene calc-alkaline volcanic rocks from the Kastamonu area, northern Turkey. *Contributions to Mineralogy and Petrology* **58**, 63–81.

Perini, G., Francalanci, L., Davidson, J. P. & Conticelli, S. (2004). Evolution and genesis of magmas from Vico Volcano, central Italy: multiple differentiation pathways and variable parental magmas. *Journal of Petrology* **45**, 139–182.

Plank, T. (2005). Constraints from thorium/lanthanum on sediment recycling at subduction zones and the evolution of the continents. *Journal of Petrology* **46**, 921–944.

Prelević, D., Foley, S., Romer, R. & Conticelli, S. (2008). Mediterranean Tertiary lamproites derived from multiple source components in postcollisional geodynamics. *Geochimica et Cosmochimica Acta* **72**, 2125–2156.

Prelević, D., Jacob, D. E. & Foley, S. F. (2013). Recycling plus: A new recipe for the formation of Alpine–Himalayan orogenic mantle lithosphere. *Earth and Planetary Science Letters* **362**, 187–197.

Presnall, D. & Hoover, J. (1987). High pressure phase equilibrium constraints on the origin of mid-ocean ridge basalts. In: Mysen, B. O. (ed.) *Magmatic Processes: Physicochemical Principles. Geochemical Society Special Publication* **1**, 75–89.

Rehman, H. U., Yamamoto, H., Khalil, M. A. K., Nakamura, E., Zafar, M. & Khan, T. (2008). Metamorphic history and tectonic evolution of the Himalayan UHP eclogites in Kaghan valley, Pakistan. *Journal of Mineralogical and Petrological Sciences* **103**, 242–254.

Replumaz, A., Negredo, A. M., Villaseñor, A. & Guillot, S. (2010). Indian continental subduction and slab break-off during Tertiary collision. *Terra Nova* **22**, 290–296.

Replumaz, A., Guillot, S., Villaseñor, A. & Negredo, A. M. (2013). Amount of Asian lithospheric mantle subducted during the India/Asia collision. *Gondwana Research* **24**, 936–945.

Replumaz, A., Capitanio, F. A., Guillot, S., Negredo, A. M. & Villaseñor, A. (2014). The coupling of Indian subduction and Asian continental tectonics. *Gondwana Research* **26**, 608–626.

Richards, A., Argles, T., Harris, N., Parrish, R., Ahmad, T., Darbyshire, F. & Draganits, E. (2005). Himalayan architecture constrained by isotopic tracers from clastic sediments. *Earth and Planetary Science Letters* **236**, 773–796.

Rickwood, P. C. (1989). Boundary lines within petrologic diagrams which use oxides of major and minor elements. *Lithos* **22**, 247–263.

Roeder, P. L. & Emslie, R. F. (1970). Olivine–liquid equilibrium. *Contributions to Mineralogy and Petrology* **29**, 275–289.

Rogers, N., Hawkesworth, C., Parker, R. & Marsh, J. (1985). The geochemistry of potassic lavas from Vulsini, central Italy and implications for mantle enrichment processes beneath the Roman region. *Contributions to Mineralogy and Petrology* **90**, 244–257.

Rollinson, H. R. (1993). Using Geochemical Data: Evaluation, Presentation, Interpretation. New York: Longman Scientific & Technical, Longman House, 352 pp.

Royden, L. H., Burchfiel, B. C. & van der Hilst, R. D. (2008). The geological evolution of the Tibetan Plateau. *Science* **321**, 1054–1058.

Rudnick, R. L. & Gao, S. (2003). Composition of the continental crust. In: Holland, H. D. & Turekian, K. K. (eds) *Treatise on Geochemistry*. Elsevier, pp. 1–63.

Schärer, U. (1984). The effect of initial $^{230}$Th disequilibrium on young U–Pb ages: the Makalu case, Himalaya. *Earth and Planetary Science Letters* **67**, 191–204.

Schulte-Pelkum, V., Monsalve, G., Sheehan, A., Pandey, M., Sapkota, S., Bilham, R. & Wu, F. (2005). Imaging the Indian subcontinent beneath the Himalaya. *Nature* **435**, 1222–1225.

Sobolev, A. V., Hofmann, A. W., Sobolev, S. V. & Nikogosian, I. K. (2005). An olivine-free mantle source of Hawaiian shield basalts. *Nature* **434**, 590–597.

Sobolev, A. V., Hofmann, A. W., Kuzmin, D. V., Yaxley, G. M., Arndt, N. T., Chung, S. L., Danyushevsky, L. V., Elliott, T., Frey, F. A., Garcia, M. O., Gurenko, A. A., Kamenetsky, V. S., Kerr, A. C., Krivolutskaya, N. A., Matvienkov, V. V., Nikogosian, I. K., Rocholl, A., Sigurdsson, I. A., Sushchevskaya, M. M. & Teklay, M. (2007). The amount of recycled crust in sources of mantle-derived melts. *Science* **316**, 412–417.

Spandler, C., Hermann, J., Arculus, R. & Mavrogenes, J. (2003). Redistribution of trace elements during prograde metamorphism from lawsonite blueschist to eclogite facies; implications for deep subduction-zone processes. *Contributions to Mineralogy and Petrology* **146**, 205–222.

Steiger, R. H. & Jäger, E. (1977). Subcommission on geochronology: convention on the use of decay constants in geo- and cosmochronology. *Earth and Planetary Science Letters* **36**, 359–362.

Straub, S. M., LaGatta, A. B., Martin-Del Pozzo, A. L. & Langmuir, C. H. (2008). Evidence from high-Ni olivines for a hybridized peridotite/pyroxenite source for orogenic andesites from the central Mexican Volcanic Belt. *Geochemistry, Geophysics, Geosystems* **9**, Q03007, doi:10.1029/2007GC001583.

Sun, C., Zhao, Z., Mo, X., Zhu, D., Dong, G., Zhou, S., Dong, X. & Xie, G. (2007). Geochemistry and origin of the Miocene

Sailipu ultrapotassic rocks in western Lhasa block, Tibetan plateau. *Acta Petrologica Sinica* **23**, 2715–2726 (in Chinese with English abstract).

Sun, C., Zhao, Z., Mo, X., Zhu, D., Dong, G., Zhou, S., Chen, H., Xie, L., Sun, Y. & Yu, F. (2008). Enriched mantle source and petrogenesis of Sailipu ultrapotassic rocks in southwestern Tibetan plateau: constraints from zircon U–Pb geochronology and Hf isotopic compositions. *Acta Petrologica Sinica* **24**, 249–264 (in Chinese with English abstract).

Sun, S. & McDonough, W. F. (1989). Chemical and isotopic systematics of oceanic basalts: implications for mantle composition and processes. In: Saunders, A. D. & Norry, M. J. (eds) *Magmatism in the Ocean Basins. Geological Society, London, Special Publications* **42**, 313–345.

Sun, Z., Pei, J., Li, H., Xu, W., Jiang, W., Zhu, Z., Wang, X. & Yang, Z. (2012). Palaeomagnetism of late Cretaceous sediments from southern Tibet: evidence for the consistent palaeolatitudes of the southern margin of Eurasia prior to the collision with India. *Gondwana Research* **21**, 53–63.

Tapponnier, P. (2001). Oblique stepwise rise and growth of the Tibet Plateau. *Science* **294**, 1671–1677.

Tian, S., Hu, W., Hou, Z., Mo, X., Yang, Z., Zhao, Y., Hou, K., Zhu, D., Su, A. & Zhang, Z. (2012). Enriched mantle source and petrogenesis of Miocene Sailipu ultrapotassic rocks in western Lhasa block, Tibetan Plateau: lithium isotopic constraints. *Mineral Deposits* **4**, 791–812 (in Chinese with English abstract).

Tommasini, S., Avanzinelli, R. & Conticelli, S. (2011). The Th/La and Sm/La conundrum of the Tethyan realm lamproites. *Earth and Planetary Science Letters* **301**, 469–478.

Turner, S., Hawkesworth, C., Liu, J., Rogers, N., Kelley, S. & Van Calsteren, P. (1993). Timing of Tibetan uplift constrained by analysis of volcanic rocks. *Nature* **364**, 50–54.

Turner, S., Arnaud, N., Liu, J., Rogers, N., Hawkesworth, C., Harris, N., Kelleyv, S., Calsteren, P. V. & Deng, W. (1996). Post-collision, shoshonitic volcanism on the Tibetan Plateau: implications for convective thinning of the lithosphere and the source of ocean island basalts. *Journal of Petrology* **37**, 45–71.

Usui, T., Nakamura, E. & Helmstaedt, H. (2006). Petrology and geochemistry of eclogite xenoliths from the Colorado Plateau: implications for the evolution of subducted oceanic crust. *Journal of Petrology* **47**, 929–964.

Wang, B., Xu, J., Zhang, X., Chen, J., Kang, Z. & Dong, Y. (2008). Petrogenesis of Miocene volcanic rocks in the Sailipu area, western Tibetan Plateau: geochemical and Sr–Nd isotopic constraints. *Acta Petrologica Sinica* **24**, 265–278 (in Chinese with English abstract).

Wang, B. D., Chen, J. L., Xu, J. F. & Wang, L. Q. (2014a). Geochemical and Sr–Nd–Pb–Os isotopic compositions of Miocene ultrapotassic rocks in southern Tibet: petrogenesis and implications for the regional tectonic history. *Lithos* **208–209**, 237–250.

Wang, G.-D., Wang, H., Chen, H.-X., Lu, J.-S. & Wu, C.-M. (2014b). Metamorphic evolution and zircon U -Pb geochronology of the Mts. Huashan amphibolites: insights into the Palaeoproterozoic amalgamation of the North China Craton. *Precambrian Research* **245**, 100–114.

Wang, Q., Chung, S. L., Li, X. H., Wyman, D., Li, Z. X., Sun, W. D., Qiu, H. N., Liu, Y. S. & Zhu, Y. T. (2012). Crustal melting and flow beneath northern Tibet: evidence from Mid-Miocene to Quaternary strongly peraluminous rhyolites in the southern Kunlun range. *Journal of Petrology* **53**, 2523–2566.

Wang, Z. & Gaetani, G. A. (2008). Partitioning of Ni between olivine and siliceous eclogite partial melt: experimental constraints on the mantle source of Hawaiian basalts. *Contributions to Mineralogy and Petrology* **156**, 661–678.

Wen, D., Chung, S., Song, B., Iizuka, Y., Yang, H., Ji, J., Liu, D. & Gallet, S. (2008). Late Cretaceous Gangdese intrusions of adakitic geochemical characteristics, SE Tibet: petrogenesis and tectonic implications. *Lithos* **105**, 1–11.

Williams, H., Turner, S., Kelley, S. & Harris, N. (2001). Age and composition of dikes in southern Tibet: new constraints on the timing of east–west extension and its relationship to post-collisional volcanism. *Geology* **29**, 339–342.

Williams, H. M., Turner, S. P., Pearce, J. A., Kelley, S. P. & Harris, N. B. W. (2004). Nature of the source regions for post-collisional, potassic magmatism in southern and northern Tibet from geochemical variations and inverse trace element modelling. *Journal of Petrology* **45**, 555–607.

Wilson, B. M. (1989). *Igneous Petrogenesis: a Global Tectonic Approach*. Unwin Hyman, 466 pp.

Wittlinger, G., Farra, V., Hetényi, G., Vergne, J. & Nábělek, J. (2009). Seismic velocities in southern Tibet lower crust: a receiver function approach for eclogite detection. *Geophysical Journal International* **177**, 1037–1049.

Woodhead, J., Hergt, J., Davidson, J. & Eggins, S. (2001). Hafnium isotope evidence for 'conservative' element mobility during subduction zone processes. *Earth and Planetary Science Letters* **192**, 331–346.

Woolley, A. R., Bergman, S. C., Edgar, A. D., Le Bas, M. J., Mitchell, R. H., Rock, N. M. S. & Scott Smith, B. H. (1996). Classification of lamprophyres, lamproites, kimberlites, and kalsilitic, melilitic, and leucitic rocks. *Canadian Mineralogist* **34**, 175–186.

Workman, R. K. & Hart, S. R. (2005). Major and trace element composition of the depleted MORB mantle (DMM). *Earth and Planetary Science Letters* **231**, 53–72.

Worthington, J. R., Hacker, B. R. & Zandt, G. (2013). Distinguishing eclogite from peridotite: EBSD-based calculations of seismic velocities. *Geophysical Journal International* **193**, 489–505.

Xie, G., Zou, A., Yuan, J., Li, X., Liao, S., Tang, F., Huang, C., Chen, Z. & Xu, Z. (2004). New results and major progress in regional geological survey of the Boindoi District and Comai sheets. *Geological Bulletin of China* **23**, 498–505 (in Chinese with English abstract).

Yang, Z., Hou, Z., White, N. C., Chang, Z., Li, Z. & Song, Y. (2009). Geology of the post-collisional porphyry copper–molybdenum deposit at Qulong, Tibet. *Ore Geology Reviews* **36**, 133–159.

Yin, A., Harrison, T. M., Ryerson, F., Chen, W. C., Kidd, W. & Copeland, P. (1994). Tertiary structural evolution of the Gangdese thrust system, southeastern Tibet. *Journal of Geophysical Research* **99**, 18175–18201.

Yu, L., Zhao, W., Chen, J., Guo, Q. & Wang, B. (2012). Mineralogical characteristics of the sodium- and potassic-rich alkaline volcanic rocks at Tangra Yumco, SE Tibet: implications for petrogenesis. *Geotectonica et Metallogenia* **36**, 274–283.

Zhang, L. Y., Ducea, M. N., Ding, L., Pullen, A., Kapp, P. & Hoffman, D. (2014a). Southern Tibetan Oligocene–Miocene adakites: a record of Indian slab tearing. *Lithos* **210–211**, 209–223.

Zhang, S. Q. (1996). Mesozoic and Cenozoic volcanism in central Gangdese: implications for lithospheric evolution of the Tibetan Plateau. PhD thesis, China University of Geosciences, Beijing (in Chinese with English abstract).

Zhang, Z. J., Wang, Y. H., Houseman, G. A., Xu, T., Wu, Z. B., Yuan, X. H., Chen, Y., Tian, X. B., Bai, Z. M. & Teng, J. W. (2014b). The Moho beneath western Tibet: shear zones and eclogitization in the lower crust. *Earth and Planetary Science Letters* **408**, 370–377.

Zhao, J. M., Yuan, X. H., Liu, H. B., Kumar, P., Pei, S. P., Kind, R., Zhang, Z. J., Teng, J. W., Ding, L., Gao, X. & Wang, W. (2010). The boundary between the Indian and Asian tectonic plates below Tibet. *Proceedings of the National Academy of Sciences of the USA* **107**, 11229–11233.

Zhao, W., Kumar, P., Mechie, J., Kind, R., Meissner, R., Wu, Z., Shi, D., Su, H., Xue, G. & Karplus, M. (2011). Tibetan plate overriding the Asian plate in central and northern Tibet. *Nature Geoscience* **4**, 870–873.

Zhao, Z., Mo, X., Nomade, S., Renne, P., Zhou, S., Dong, G., Wang, L., Zhu, D. & Liao, Z. (2006). Post-collisional ultrapotassic rocks in Lhasa block, Tibetan Plateau: Spatial and temporal distribution and its implications. *Acta Petrologica Sinica* **22**, 787–794 (in Chinese with English abstract).

Zhao, Z., Mo, X., Dilek, Y., Niu, Y., DePaolo, D. J., Robinson, P., Zhu, D., Sun, C., Dong, G. & Zhou, S. (2009a). Geochemical and Sr–Nd–Pb–O isotopic compositions of the post-collisional ultrapotassic magmatism in SW Tibet: petrogenesis and implications for India intra-continental subduction beneath southern Tibet. *Lithos* **113**, 190–212.

Zhao, Z., Mo, X., Zhu, D., Niu, Y., Dong, G., Zhou, S., Liao, Z. & DePaolo, D. J. (2009b). Petrogenesis and implications of the volcanic rocks in Zabuye salt lake area, western Lhasa terrane, Tibet, China. *Geological Bulletin of China* **28**, 1730–1740 (in Chinese with English abstract).

Zheng, Y. G., Hou, Z. Q., Li, Q. Y., Sun, Q. Z., Liang, W., Fu, Q., Li, W. & Huang, K. X. (2012). Origin of late Oligocene adakitic intrusives in the southeastern Lhasa terrane: evidence from *in situ* zircon U–Pb dating, Hf–O isotopes and whole-rock geochemistry. *Lithos* **148**, 296–311.

Zhou, H. & Murphy, M. A. (2005). Tomographic evidence for wholesale underthrusting of India beneath the entire Tibetan plateau. *Journal of Asian Earth Sciences* **25**, 445–457.

Zhou, S., Mo, X., Dong, G., Zhao, Z., Qiu, R., Guo, T. & Wang, L. (2004). $^{40}$Ar–$^{39}$Ar geochronology of Cenozoic Linzizong volcanic rocks from Linzhou Basin, Tibet, China, and their geological implications. *Chinese Science Bulletin* **49**, 1970–1979.

Zhou, S., Mo, X., Zhao, Z., Qiu, R., Niu, Y., Guo, T. & Zhang, S. (2010). $^{40}$Ar/$^{39}$Ar geochronology of post-collisional volcanism in the middle Gangdese belt, southern Tibet. *Journal of Asian Earth Sciences* **37**, 246–258.

Zhu, B., Kidd, W. S., Rowley, D. B., Currie, B. S. & Shafique, N. (2005). Age of initiation of the India–Asia collision in the east–central Himalaya. *Journal of Geology* **113**, 265–285.